Laser irradiation effect on $MoTe_2$ and its transistor application

August 2024

XIE TIANSHUN

Graduate School of Science and Engineering

CHIBA UNIVERSITY

（千葉大学審査学位論文）

Laser irradiation effect on $MoTe_2$ and its transistor application

August 2024

XIE TIANSHUN

Graduate School of Science and Engineering

CHIBA UNIVERSITY

Abstract

With the development of integrated circuits, the improvement in chip performance has benefited from the scaling of metal-oxide-semiconductor field-effect transistors (MOSFETs) based on silicon. However, as scaling progresses, the short-channel effects become more pronounced, and the evolution of Si-MOSFETs has reached physical limits. Therefore, new structure transistors and new channel materials are considered in the roadmap for the future development of integrated circuits. Since the successful exfoliation of graphene, various two-dimensional (2D) materials have been extensively researched. Among them, transition metal dichalcogenide (TMDC) semiconductor materials exhibit a strong tolerance to the short-channel effect and high carrier mobility even at the atomic level thickness. This makes them the best candidates for channel materials in future integrated circuits. However, the application of TMDC semiconductor materials faces various challenges, such as poor metal-semiconductor contact properties and lack of doping methods.

2H-$MoTe_2$, a member of the TMDC semiconductor material family, has a relatively smaller band gap of 0.9 eV in multilayer and 1.1eV in monolayer compared with other TMDC materials. It can be readily doped to exhibit either n-type or p-type transfer characteristics; Hence, it demonstrates outstanding potential for utilization in complementary MOSFET (CMOS). Previous studies have reported that laser irradiation in the atmosphere can transform 2H-$MoTe_2$ into a semi-metallic 1T' phase, and this 1T' phase exhibits Ohmic contact characteristics with its 2H phase. This improved the contact properties of $MoTe_2$-FET. However, a study also indicates that the product of laser irradiation in the atmosphere is not 1T'-MoTe2 but rather a mixture of thermally decomposed Te atomic layers and Mo oxide.

Therefore, based on previous research, this study first verified that the product formed by appropriately high-intensity laser irradiation on 2H-$MoTe_2$ crystal in the atmosphere is a mixture of MoO_2 and Te. Next, different from laser irradiation in the atmosphere, it was found that $MoTe_2$ crystal transform from the 2H semiconductor phase to another metallic phase of 1T, which is different from the 1T' phase, under

appropriately high-intensity laser irradiation in a vacuum. By employing this technique, a 1T/2H/1T polymorphic homojunction has been achieved. Then, the contact properties of 1T-contacted 2H-$MoTe_2$-FET were investigated by fabricating metal electrodes on the 1T surface.

For the vicinity of the directly irradiated area, this study confirmed that laser irradiation in vacuum and the atmosphere, respectively, induces heavy n-type doping and heavy p-type doping effects. Therefore, after heavy doping via laser irradiation in the contact area of $MoTe_2$-FET during the fabrication process, relatively low Schottky barrier height and contact resistance were obtained. Additionally, since the contact doping method can also control the polarity of $MoTe_2$-FET, this study realized the operation of $MoTe_2$ CMOS inverter with a high gain.

Unlike conventional MOSFETs, tunneling field effect transistors (TFETs) utilizing the band-to-band tunneling (BTBT) phenomenon in semiconductors are not limited by the thermal electron emission limit of 60 mV/dec for the subthreshold swing (*SS*) value at room temperature. Thus, TFETs have significant potential in low-power device applications. While the low on-state current currently constrains the applicability of 3D-TFETs, it is anticipated that this issue will be resolved with 2D materials, thanks to their excellent electrostatic, small tunnel distance, and pristine surface characteristics. 2D-TFET fabrication requires heavily doped semiconductor materials as sources; thus, this study used laser-induced doping to achieve the operation of both n-TFET and p-TFET on a single $MoTe_2$ crystal. Finally, n-TFET and p-TFET are fabricated on the same substrate and combined into an inverter. It successfully achieves signal inversion, representing the first demonstration of a 2D-CTFET inverter in the world.

Table of contents

1. Introduction 1

1.1. MOSFET technology 1

1.1.1. MOSFET structure 1

1.1.2. CMOS inverter 3

1.1.3. Short-channel effect 4

1.1.4. Transistors' future 5

1.2. TFET technology 7

1.2.1. TFET structure 7

1.2.2. Performance factors 10

1.2.3. TFET development 12

1.3. 2D-materials 14

1.3.1. Graphene 14

1.3.2. Hexagonal boron nitride 16

1.3.3. Transition metal dichalcogenides 17

1.4. 2D-FET 18

1.5. Fermi level pinning effect 21

1.6. 2D-TFET 23

1.7. Recent studies on $MoTe_2$ 26

1.7.1. Polycrystalline characteristic 26

1.7.2. $MoTe_2$-FET and TFET 28

1.7.3. Laser irradiation for $MoTe_2$ 31

Reference 32

2. Experimental method 36

2.1. Exfoliation process 36

2.1.1. Exfoliation of graphene and *h*-BN 37

2.1.2. Exfoliation of TMDCs 39

2.2. Substrate cleaning 40

2.3. Lithography 41

2.3.1. UV lithography 41

2.3.2. Electron beam lithography 42

2.4. Metal deposition and lift-off 42

2.5. Dry transfer 43

2.6. Laser irradiation 48

2.7. Raman spectroscopy 49

2.8. Electric measurement 51

2.8.1. Current-Voltage (I-V) characteristics 51

2.8.2. Inverter measurement 52

Reference 53

3. Laser irradiation effect on $MoTe_2$ 54

3.1. Laser-induced phase transition 55
3.1.1. Effect on atmosphere condition 55
3.1.2. Effect on vacuum condition for 2H-$MoTe_2$ 57
3.1.3. Effect on vacuum condition for 1T'-$MoTe_2$ 62
3.1.4. Temperature change in phase transition 64
3.1.5. Mechanism of phase transition 66
3.2. Laser-induced doping 68
3.2.1. Heavy n-doping effect 69
3.2.2. Heavy p-doping effect 73
3.3. Conclusion 76
Reference 77

4. Contact engineering on $MoTe_2$-FET via laser irradiation 78

4.1. Polymorphic contact 78
4.1.1. Laser-induced 1T-phase contact 79
4.1.2. 1T'-phase top contact 84
4.2. Contact doping 90
4.3. CMOS inverter fabrication 96
4.4. Conclusion 106
Reference 107

5. $MoTe_2$-TFET fabrication via laser-induced doping 108

5.1. Out-of-plane $MoTe_2$/MoS_2 n-TFET 109
5.2. In-plane $MoTe_2$ n-TFET 118
5.3. Drain-doped in-plane $MoTe_2$ n-TFET 122
5.4. In-plane $MoTe_2$ p-TFET 131
5.5. CTFET inverter realization 140
5.6. Conclusion 145
Reference 146

6. Conclusion and outlook 147

6.1. Conclusion 147
6.2. Outlook 149

Acknowledgments 150

Publications and conferences 152

1. Introduction

1.1. MOSFET technology

1.1.1. MOSFET structure

Metal-oxide-semiconductor field-effect transistor (MOSFET) technology is a fundamental building block of modern electronic products, widely used in various applications such as digital and analog circuits, power electronics, and radio-frequency systems. MOSFETs have become key components in integrated circuits (ICs) and electronic devices due to their high efficiency, low power consumption, and scalability [1~3]. MOSFETs are composed of a semiconductor substrate (often silicon) on which three terminals are built: the source, the drain, and the gate. The gate is separated from the semiconductor by a thin insulating layer, usually silicon dioxide (SiO_2) or some high-k materials such as hafnium dioxide (HfO_2). This gate oxide layer is crucial as it allows for the control of current flow between the source and drain. MOSFET operation relies on the manipulation of an electric field within the semiconductor substrate. When a voltage is applied to the gate terminal, an electric field is established across the gate oxide layer, which in turn modulates the conductivity of the semiconductor beneath it. This modulation creates a channel between the source and drain, allowing current to flow when a sufficient voltage is applied. MOSFETs can be categorized based on the majority carrier type. N-channel MOSFET (NMOS) uses electrons as majority carriers, while P-channel MOSFET (PMOS) uses holes. **Figure 1.1** shows the structure of the NMOS and PMOS based on silicon.

The scaling of MOSFETs refers to the continuous reduction in the size of transistors, specifically the dimensions of critical components such as gate length, gate oxide thickness, and source-drain spacing [4]. Scaling is a fundamental trend in semiconductor manufacturing driven by the desire to increase transistor density, improve performance, and reduce power consumption. Gordon Moore forecasted the scaling speed in 1965, which is famously referred to as "Moore's Law." The development of MOSFET technology has followed Moore's Law for decades, as shown in **Fig. 1.2**. However, continued scaling faces significant technical and economic

challenges, such as short channel effects as feature sizes approach atomic dimensions and new materials and manufacturing techniques are required to sustain further progress.

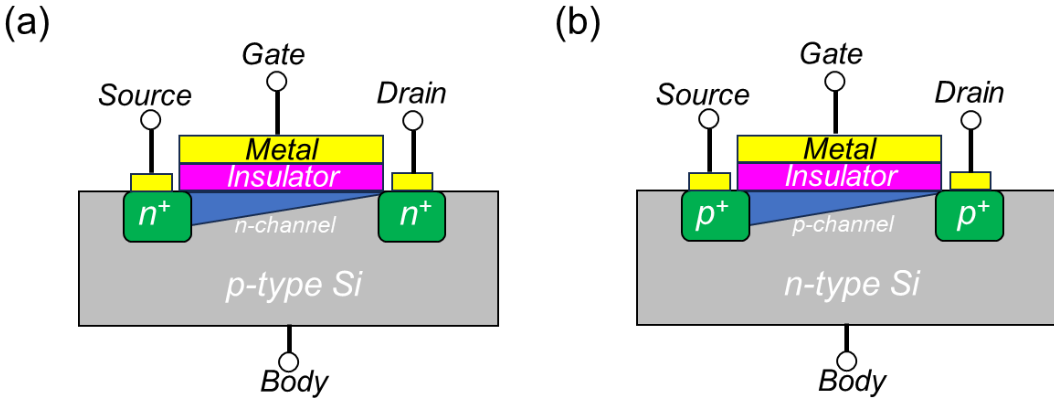

Fig. 1.1 Basic structure of NMOS (a) and PMOS (b).

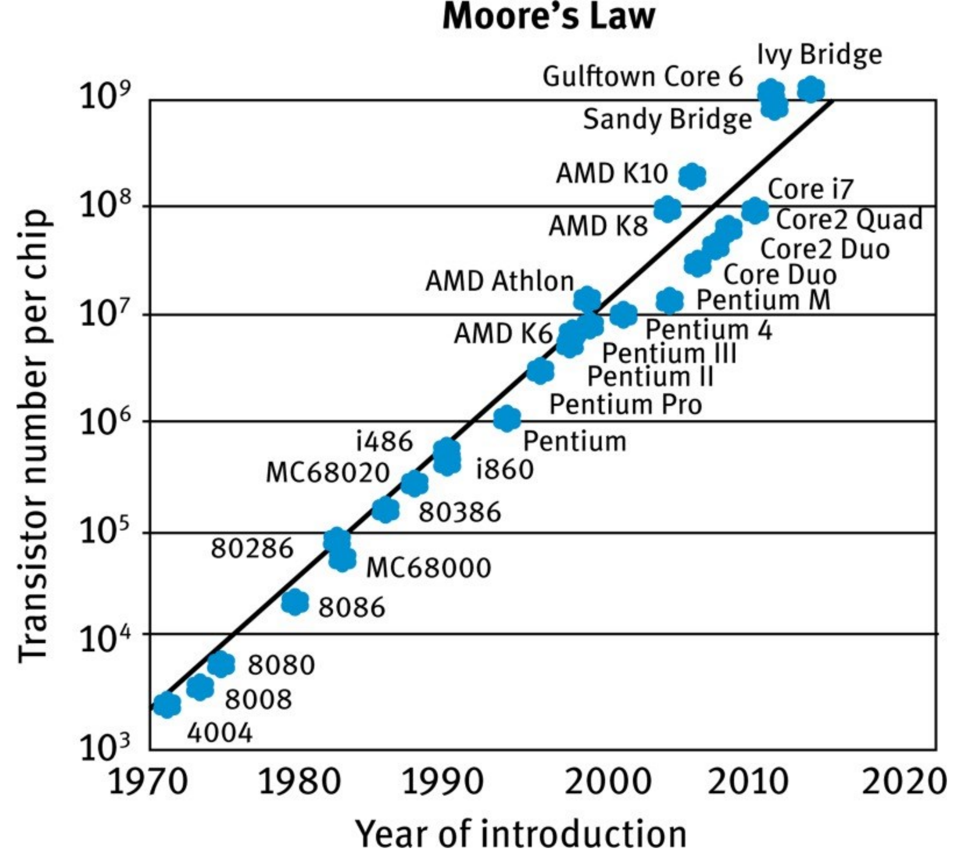

Fig. 1.2 Moore's law of semiconductor development [5].

1.1.2. CMOS inverter

A CMOS inverter is a common digital logic gate circuit used to reverse the logic state of an input signal completely. It consists of an NMOS and a PMOS connected in series. In a CMOS inverter, the source terminals of the PMOS and NMOS transistors are respectively connected to the power supply and ground, while their drain terminals are connected to the output terminal, as shown in **Fig 1.3**. When the input signal is at a high logic level, the NMOS transistor conducts, resulting in a low output level. Conversely, when the input signal is at a low logic level, the PMOS transistor conducts, leading to a high output level. CMOS inverters have advantages such as low power consumption, low-voltage operation, strong resistance to breakdown, and good high-temperature stability, making them suitable for various digital circuits [6].

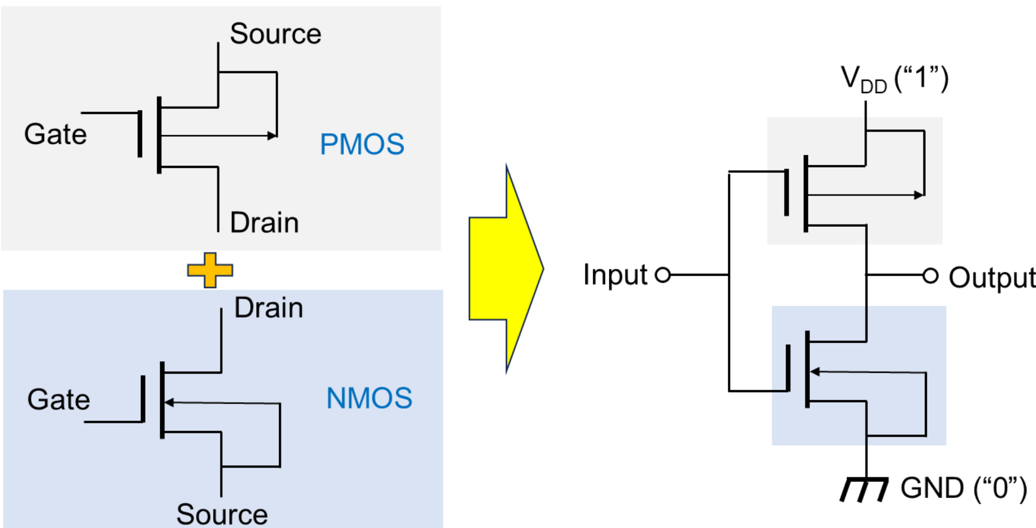

Fig. 1. 3 Diagram of basic structure in CMOS inverter.

1.1.3. Short-channel effect

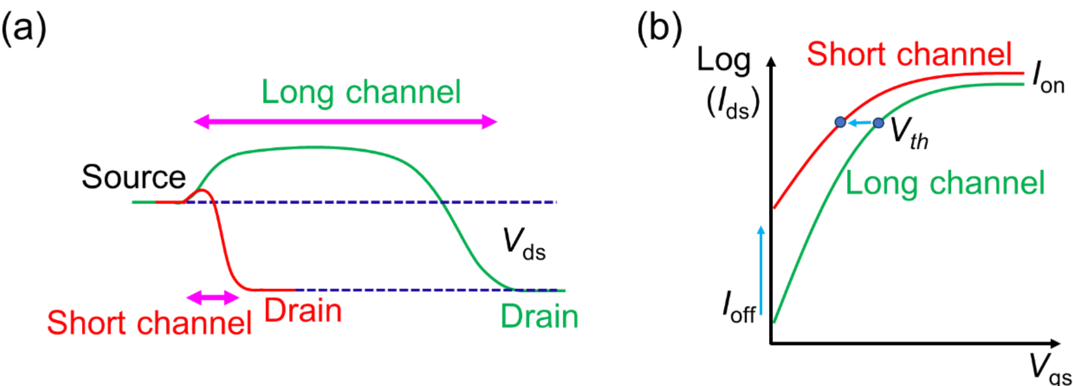

Fig. 1.4 Energy band diagram (a) and transfer characteristics (b) of long and short channel MOSFETs.

The improvement in chip performance is attributed to the continuous scaling of the transistor, which involves a reduction in channel length. However, when the channel length is reduced to a certain extent, transistors experience a series of performance degradation issues collectively referred to as the short-channel effect, as shown in **Fig. 1.4**. Here are some key aspects of the short-channel effect [7,8]:

1. Increased Leakage Current: The reduced channel length weakens the gate's control over the channel, increasing leakage current. This reduces the transistor's switching efficiency and leads to higher power consumption.
2. Degradation of Subthreshold Slope: As the channel length shortens, the subthreshold slope of the transistor may increase. The subthreshold slope refers to the relationship between channel current (I_{ds}) and gate-to-source voltage (V_{gs}). In short-channel transistors, the subthreshold slope degrades due to increased leakage currents, resulting in poorer control over the transistor's switching behavior and reduced energy efficiency.
3. Drain-induced barrier lowering (DIBL): In short-channel transistors, the DIBL phenomenon becomes more significant. This occurs when a high voltage between the source and drain terminals prevents the gate voltage from completely closing the channel, resulting in additional leakage current.
4. Threshold voltage variation: Short-channel effects can lead to variations in the

threshold voltage (V_{th}) across different regions of the transistor, complicating the design and manufacturing process and reducing the device's reliability.

Overall, managing short-channel effects is essential for maintaining the performance and reliability of MOSFETs as semiconductor technology continues to advance towards smaller feature sizes and higher integration densities.

1.1.4. Transistors' future

The scalability of FETs can be quantified by a feature length called the natural length λ, given by the first-order approximation equation as [9,10]:

$$\lambda = \sqrt{\alpha t_{ox} t_{ch} \frac{\varepsilon_{ch}}{\varepsilon_{ox}}} \tag{1.1}$$

Where $\varepsilon_{ox/ch}$ and $t_{ox/ch}$ are the relative permittivity and thickness of the gate dielectric/channel, respectively. α is a geometric factor that reflects the gate topology and decreases with an increase in the number of gates in FETs. To ensure good electrostatic of the channel, it is necessary for the channel length (L_{ch}) to be greater than 3~5 times the feature length (λ). According to the equation, the improvement in scalability can be approached from three directions. Firstly, by reducing "α," which implies increasing the number of gates for individual transistors. For example, the FinFET structure commonly used in advanced chip manufacturing is effectively a triple-gate structure. This configuration significantly enhances the gate's electrostatic control over the channel, thus effectively mitigating the short-channel effect while scaling down transistor sizes. The second is to reduce the ratio of $\frac{t_{ox}}{\varepsilon_{ox}}$, which involves utilizing a gate oxide with a higher dielectric constant, such as hafnium dioxide lanthanum oxide, or reducing its thickness. The third approach involves reducing the thickness and dielectric constant of the channel material. In the most advanced FinFET processes, the channel thickness is around 4 nm. However, further reduction in channel thickness would significantly reduce the mobility of silicon. Fortunately, atomic-scale materials such as single-wall carbon nanotubes (SWNTs) [11] and emerging 2D layered semiconductors, particularly transition metal dichalcogenides (TMDCs) [12], hold promise as potential replacements for silicon in the next generation of channel materials.

Figure 1.5 shows the roadmap of semiconductor development in the future made by Tokyo Electron Ltd.

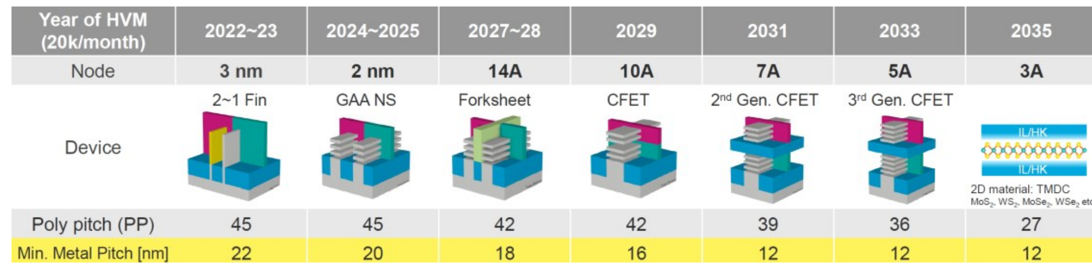

Year of HVM (20k/month)	2022~23	2024~2025	2027~28	2029	2031	2033	2035
Node	3 nm	2 nm	14A	10A	7A	5A	3A
Device	2~1 Fin	GAA NS	Forksheet	CFET	2nd Gen. CFET	3rd Gen. CFET	IL/HK, IL/HK, 2D material: TMDC MoS_2, WS_2, $MoSe_2$, WSe_2 etc.
Poly pitch (PP)	45	45	42	42	39	36	27
Min. Metal Pitch [nm]	22	20	18	16	12	12	12

Fig. 1.5 Roadmap of semiconductor development [13].

1.2. TFET technology

1.2.1. TFET structure

The use of CMOS technology based on Si has greatly enhanced the switching speed, device operation, and cost-effectiveness of microprocessors. However, FET-based nanoelectronics circuits do not exhibit high energy efficiency, with power consumption mainly stemming from two aspects: higher supply voltage and significant leakage current in the off-state [14~17]. In recent years, the rapid development of AI·IoT has led to increasing demand for low-power devices. Consequently, various research efforts have been dedicated to improving device designs and introducing unique materials as substitutes for Si to produce transistors with fast switching. The primary goal is to design devices that operate at lower supply voltages (< 0.5 V) by achieving a subthreshold swing (SS) of < 60 mV/decade at room temperature, which represents the ultimate limit of conventional MOSFETs due to the Boltzmann distribution of charge carriers. Among these efforts, a new class of FETs, which is called tunnel field-effect transistors (TFETs), has emerged. TFETs utilize the mechanism of band-to-band tunneling (BTBT) based on quantum mechanics to transport charge carriers rather than conventional thermal injection. TFETs fabricated with thin semiconductor films or nanowires can achieve a 100-fold reduction in power compared to MOSFETs [18]. Therefore, the combination of TFETs and CMOS technology can improve the integrated circuits of low-power devices. The structure of TFET is very similar to that of MOSFET, with the only difference being the opposite doping polarity at the source and drain in TFET. This creates a p/i/n diode within the semiconductor with an MOS structure, as shown in **Fig 1.6 (a)**. Under reverse bias, the tunneling current flowing through the device is controlled by the gate voltage.

Figure 1.6 (b) shows the different conduction mechanisms of MOSFET and TFET from the perspective of the energy band structure. In MOSFET (n-channel), when no gate voltage is applied, the high Barrier at the source-channel interface prevents the injection of carriers from the source into the channel; thus, no current can flow, and this state is called the off-state. When a positive gate voltage is applied, the barrier height

decreases, allowing carriers to inject into the channel and forming a stable current. This state is called the on-state. In TFET (n-channel), under reverse bias, a staggered gap referred to as type II of energy band forms at the interface between the source and the channel. In this case, the conduction band in the channel is positioned above the valence band of the source, and electrons in the source's valence band cannot tunnel through the wide Barrier into the conduction band of the channel; thus, no current can flow, and this state is called the off-state. When a gate voltage is applied, the Fermi level in the channel approaches the conduction band, gradually lowering it below the valence band of the source, forming a broken gap referred to as type III. The width of the tunneling Barrier significantly decreases, allowing carriers to tunnel from the valence band of the source into the conduction band of the channel, resulting in current flow, and this state is called the on-state.

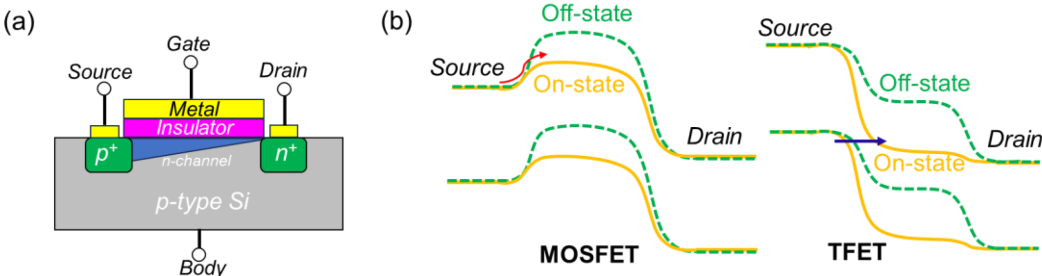

Fig. 1.6 (a) Structure of TFET. (b) Energy band diagram of on-state and off-state in MOSFET and TFET.

In traditional MOSFETs, the current switching process is primarily affected by the transmission of thermal carriers crossing the energy barrier, which limits the steepness of the current. The expression used to represent transistor operation speed in the sub-threshold region is *SS* and is formulated as [19,20]

$$SS = \ln(10)\frac{kT}{q}\left(1+\frac{C_s}{C_{ox}}\right) \tag{1.2}$$

Where C_s is the capacitance of the semiconducting channel, C_{ox} represents gate oxide capacitance and $\frac{kT}{q}$ is the thermal voltage (k: Boltzmann constant, T: temperature, q: electrical charge). The minimum *SS* for a conventional MOSFET at room temperature

($T = 300$ K) can be found by $\frac{C_s}{C_{ox}} \to 0$, which implies that

$$SS_{min} = \ln(10)\frac{kT}{q} \cong 60\, {mV}/{decade} \quad (1.3)$$

where a decade corresponds to a 10-fold increase in the drain current against an applied gate voltage of 60 mV, and it illustrates the ideal thermionic limit for a conventional MOSFET. In TFET, electrons tunnel through the barrier, and the tunneling rate corresponds to the subthreshold slope. Therefore, TFET exhibits a faster and more sensitive response in the subthreshold region than MOSFET. In theory, there is no limit to the *SS* value in TFET. **Figure 1.7** shows the transfer characteristics (I_{ds}-V_{gs}) of MOSFET and TFET. Benefiting from its steep *SS*, TFETs can be turned on at lower voltages compared to MOSFETs, and the static off-state current (I_{off}) is orders of magnitude lower because of the tunneling mechanism of current conduction. These three advantages make TFETs the prime candidate for the application of low-power devices. However, as **Fig. 1.7** shows, due to limitations in tunneling probability, the on-state current in TFET is always lower than MOSFET. Thus, enhancing the on-state current in TFETs has become a primary objective in numerous research.

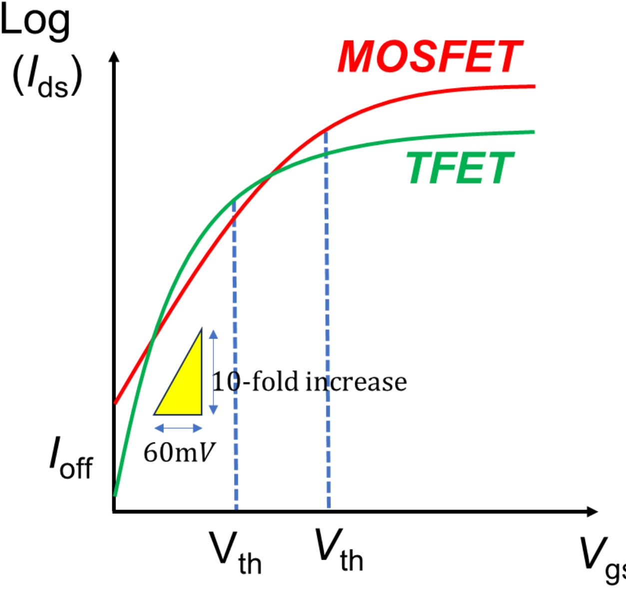

Fig. 1.7 Transfer characteristics (I_{ds}-V_{gs}) of MOSFET and TFET.

1.2.2. Performance factors

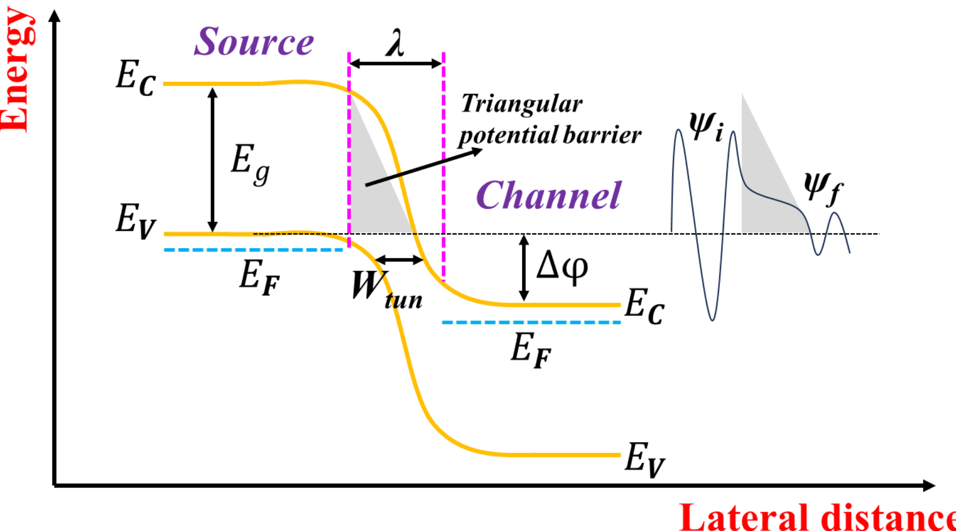

Fig. 1.8 Schematic representation of BTBT in the tunneling junction of TFET.

In TFET, the potential Barrier in the tunneling junction can be approximated as a triangular potential barrier. Several theoretical frameworks have been developed to estimate the tunneling probability through such triangular barriers. The Wentzel–Kramer–Brillouin (WKB) approach has been widely considered the most appropriate for calculating BTBT current in TFET. The tunneling probability (T_{WKB}) can be calculated using the WKB approximation as follows [21,22]:

$$T_{WKB} = \exp\left[-\frac{4\lambda\sqrt{2m^* E_g^3}}{3q\hbar\left(E_g+\Delta\varphi\right)}\right] \tag{1.4}$$

Where m^* is carrier effective mass, E_g is the energy bandgap of the material, ħ is the reduced plank constant, q is the electronic charge, Δφ is the energy window for BTBT that represents the energy difference between the source valance band maxima (VBM) and channel conduction band minima (CBM), and λ in this formula is the screening tunneling length that represents the spatial extent of the energy band bending at the tunneling junction. It should be noted that the minimum tunneling distance (W_{tun}) from the source to the channel is less than λ and strongly depends on λ. The control of tunneling probability (T_{WKB}) by the gate is actually achieved by reducing λ and simultaneously increasing Δφ through an increase in gate bias. The reason for the small

on-state current (I_{on}) in TFETs is primarily due to the limitation of tunneling probability. Therefore, the effective approach to increasing the I_{on} is to enhance the tunneling probability. According to the WKB approximation formula, selecting materials with small bandgap and electron effective mass is expected to achieve higher tunneling probability, such as strained Si [23,24] and some III-V semiconductors (InAs, InGaAs) [25]. Secondly, the tunneling window varies with the strength of the gate field; increasing the unit gate electric field strength can enlarge the tunneling window, which can be achieved by reducing the equivalent oxide thickness (EOT) of the MOS structure. The EOT is defined as $t_{ox}\frac{\varepsilon_{SiO2}}{\varepsilon_{ox}}$. Additionally, the tunneling window is also determined by the doping concentration of the source region; sufficient and appropriate doping concentration can increase the tunneling window, thereby increasing the current. Thirdly, reducing the tunneling length can greatly increase the tunneling probability. The tunneling length is affected by the following formula [26]:

$$\lambda \cong \sqrt{\frac{\varepsilon_s t_s t_{ox}}{4\varepsilon_{ox}}} \tag{1.5}$$

where ε_s and t_s are the relative permittivity and thickness of the semiconductor material. From this formula, it can be inferred that reducing the EOT can decrease the tunneling length, thereby increasing the tunneling probability. Currently, an effective method to reduce the EOT is to use a thinner high-*k* dielectric layer, such as HfO_2. In addition, the thickness of semiconductor materials also has a significant impact on the tunneling length. Reducing the thickness of the semiconductor can decrease the tunneling length and increase the tunneling probability [27]. Currently, two-dimensional semiconductor materials with atomic layer thickness, such as TMDCs, have a clear advantage in this regard. Furthermore, a sharp doping profile between the source and channel is extremely important for reducing tunneling length [28].

1.2.3. TFET development

The contact area between the source and channel also affects the overall current in the TFET [29]. In the basic structure depicted in **Fig 1.9 (a)**, where the p-n junction plane intersects perpendicularly with the MOS interface, tunneling occurs laterally along the MOS interface, resulting in a narrow tunnel region. Thus, as illustrated in **Fig 1.9 (b)**, a portion of the p-n junction surface is aligned as parallel to the MOS interface as possible. The tunneling area is expanded by tunneling vertically. In the third structure, as shown in **Fig 1.9 (c)**, tunneling occurs across the entire area of the channel perpendicular to the MOS structure, maximizing the tunneling region. Transitioning from the structure in **Fig 1.9 (a)** to **(b)** and **(c)**, the increase in tunneling area leads to an improvement in on-state current. However, the structure becomes more complex, thereby increasing device manufacturing difficulty.

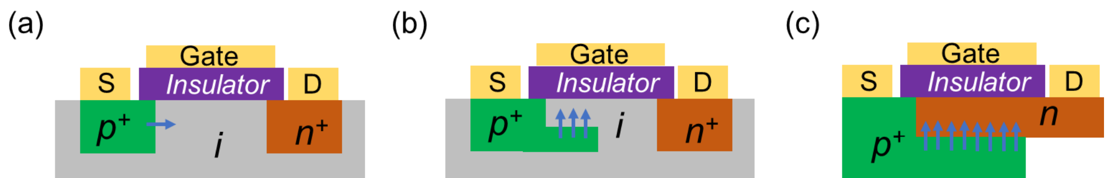

Fig. 1.9 (a) P-n junction lateral TFET. (b) P-n junction vertical TFET. (3) Bi-layer TEFT.

One major advantage of Si-TFETs is not only being able to utilize the CMOS process technology directly but also implementing nearly identical structures for both n- and p-channel TFETs using the same materials. This has been experimentally proven, especially in nanowire structures, demonstrating relatively excellent performance [30]. However, I_{on} remains relatively low, and steep *SS* has not been achieved over a wide range. Ge-TFETs possess the same advantages as Si. Although n- and p-channel Ge-TFETs with a high I_{on} have been demonstrated, I_{off} is too high and small *SS* values have not yet been reported [31]. III-V group semiconductors, such as InGaAs-TFETs with excellent MOS interface characteristics, have been extensively researched [32]. A significant challenge in III-V semiconductor TFETs is achieving satisfactory p-channel TFETs, primarily due to the high density of interface states near the valence band and

the difficulty in forming highly n-doped source regions [33]. TFETs based on oxide semiconductors such as ZnO have also been reported in recent years [34]. The tunneling distance is determined by the thickness of the oxide semiconductor, and the gate voltage can effectively control the tunneling current. Additionally, a sufficiently low I_{off} value can be achieved due to the large E_g of oxide semiconductors. However, improvements are still needed in the uniformity of oxide semiconductor film thickness and MOS interface characteristics. In recent years, owing to the excellent electrical properties of two-dimensional semiconductor materials, they have become the prime candidates for next-generation channel materials, and research on 2D-TFETs has been extensively reported, which will be discussed in detail in the next section.

1.3. 2D-materials

Two-dimensional (2D) materials are characterized by their single or few-layer atomic thicknesses. The isolation of graphene by Andre Geim and Konstantin Novoselov in 2004 opened the door to research on 2D materials [35]. Subsequently, various other types of 2D materials have been extensively studied. 2D materials encompass a wide range of physical properties, including superconductors, conductors, semiconductors, and insulators. Their diverse physical properties make them promising candidates for applications in electronics [36], optoelectronics [37], valleytronics [38], photovoltaics [39], etc. Additionally, 2D materials can be used to fabricate flexible and tunable sensors [40] and some other medical diagnostic devices [41] in the biomedical field. Multilayer 2D materials are comprised of layers held together by van der Waals forces, and the majority can be isolated into single layers through mechanical exfoliation. Here, several typical two-dimensional materials, including graphene, h-BN, and TMDCs will be introduced.

1.3.1. Graphene

Monolayer graphene is a 2D crystal structure composed of carbon atoms with a single-atom thickness (~ 0.3 nm). Its structure consists of formed carbon atoms hybridized in sp^2 orbitals, resembling a honeycomb pattern, as shown in **Fig 1.10 (a).** In the graphene lattice, each carbon atom shares three σ bonds with its adjacent three carbon atoms, forming a flat hexagonal structure, while π bonds are distributed above and below the carbon atom layer, contributing to conductivity and other properties of graphene, as shown in **Fig 1.10 (b)**. The presence of π bonds in its structure allows carriers to move freely on the plane. Thus, carriers in graphene can move at high speeds on its surface, exhibiting high electron mobility. The electron mobility in graphene obtained in experiments can reach millions [42]. The energy band of monolayer graphene is linear, and the center is called the "Dirac point" which represents the minimum carrier density. Unfortunately, lacking bandgap limits its application in logic electronic devices. However, with the types and densities of carriers being controllable,

numerous quantum phenomena and applications in other fields based on monolayer graphene have been extensively reported [43]. Bilayer graphene is composed of two stacked layers of monolayer graphene. In its initial state, similar to monolayer graphene, bilayer graphene also lacks a band gap, but a certain degree of bandgap can be opened by applying a perpendicular electric field. As the energy band of bilayer graphene can be introduced under external conditions, research on electronic devices based on bilayer graphene, including logic devices and quantum devices, has been extensively studied [44,45]. The energy band structure of monolayer, bilayer and vertical electric field applied bilayer graphene. When the number of layers exceeds three, the properties of graphene almost have no change. Multilayer graphene is commonly referred to as graphite.

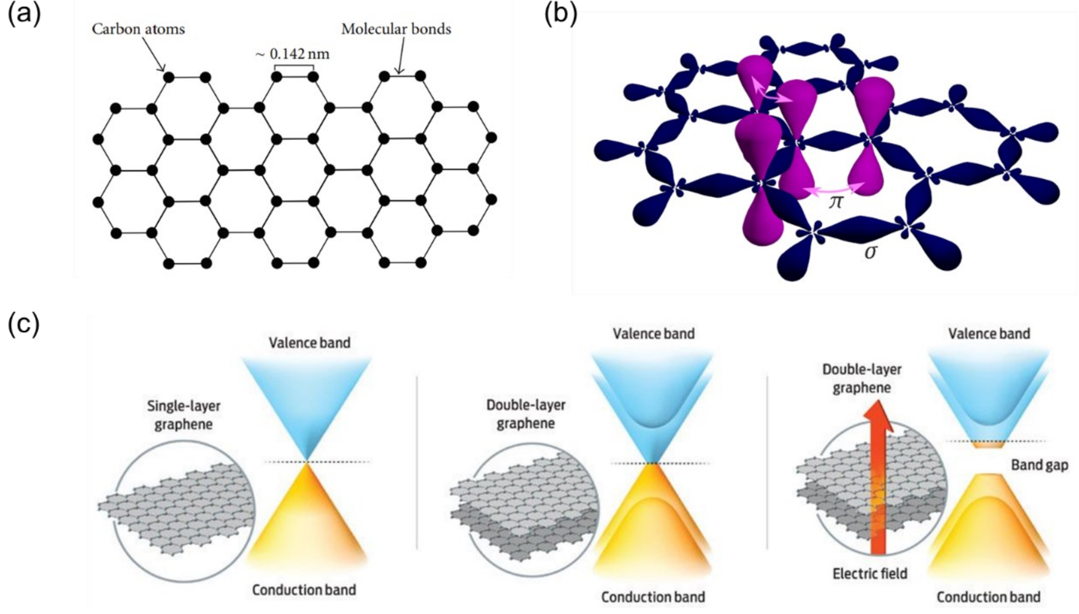

Fig. 1.10 (a) Schematic of the structure of a graphene sheet [46]. (b) σ bonds and π bonds in graphene. (c) The energy band structure of monolayer, bilayer graphene and vertical electric field applied bilayer graphene. *(Picture adapted from https://spectrum.ieee.org/graphene-makes-transistors-tunable)*

1.3.2. Hexagonal boron nitride

Hexagonal boron nitride (h-BN) is a 2D material with a hexagonal lattice structure similar to graphene, composed of alternating nitrogen and boron atoms. In the hexagonal lattice, each boron atom is surrounded by three nitrogen atoms, and conversely, each nitrogen atom is surrounded by three boron atoms, thereby establishing a stable crystal structure. The alternating arrangement of nitrogen and boron atoms in h-BN confers different chemical and physical properties compared to graphene. h-BN has a bandgap of ~6 eV and an equivalent dielectric constant to SiO_2 ($\varepsilon = 3.9$), exhibiting excellent electrical insulation and voltage tolerance. This makes it highly promising for applications in 2D electronic devices as an insulating layer or substrate [47]. In addition, h-BN exhibits excellent thermal and chemical stability and dangling bonds-free in the out-of-plane direction, minimizing band hybridization and the introduction of interface trap when combined with other 2D materials. Hence, h-BN is highly suitable for integration with other 2D materials to fabricate diverse heterostructure devices [48]. **Figure 1.10** shows the crystal and band structure of h-BN.

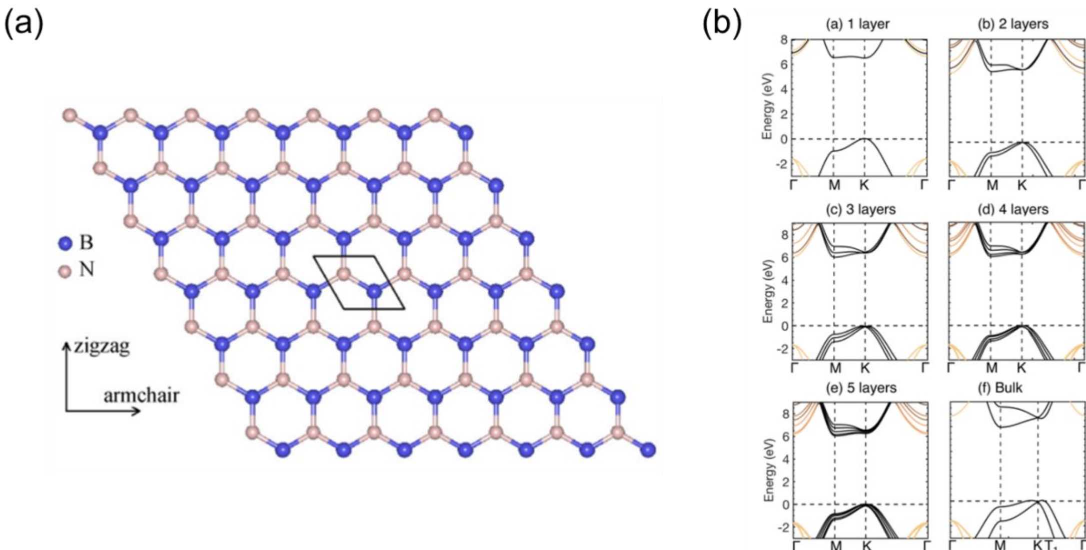

Fig. 1.10 (a) Schematic of the structure of a h-BN sheet [49]. (b) Energy band structure of h-BN with different layers [50].

1.3.3. Transition metal dichalcogenides

The general formula of transition metal dichalcogenides (TMDCs) is MX_2, where M represents a transition metal element and X represents a chalcogen element. The transition metal element can be selected from Group IV (Ti, Zr, etc.), Group V (V, Nb, etc.), or Group VI (Mo, W, etc.), sandwiched between the two planes of chalcogen anions, as shown in **Fig. 1.11 (a)**. Ionic-covalent bonds ensure the in-plane stability of the MX_2 layer, while van der Waals interactions bind the layers together, forming bulk MX_2 crystals [51]. TMDCs possess various crystal structures, such as 2H, 1T, 1T', etc. [52]. The 2H phase is a common stable structure, also known as a hexagonal lattice structure. In this structure, transition metal and chalcogen atoms form hexagonal lattice arrangements with weak interactions between layers. The 2H structure typically exhibits semiconducting properties. The 1T phase, also known as a triangular structure, exhibits highly symmetrical triangular lattice arrangements of transition metal and chalcogen atoms, generally demonstrating semimetal properties. The 1T' structure is a variant of the triangular lattice structure, also known as a distorted triangular lattice structure. In this structure, transition metal and chalcogen atoms still form triangular lattice arrangements, but there is a certain degree of distortion or deviation. This distortion may be caused by interlayer stress or external environmental factors. The distortion of the 1T' structure may lead to some physical properties different from those of the standard 1T structure. These three common crystal structures in TMDCs are shown in **Fig. 1.11 (b)**.

Unlike graphene, semiconductor TMDCs exhibit excellent semiconducting properties, with bandgaps ranging from 0 to over 2 eV. Moreover, the bandgap of semiconductor TMDCs can be tuned by changing the number of layers and can transition from direct (monolayer) to indirect (multilayer) bandgap, as shown in **Fig. 1.12**. The bandgap can also be engineered by applying an external electric field perpendicular to the TMDC layers or through strain engineering [53,54]. Some TMDCs also exhibit remarkable properties such as superconductivity and charge density waves [55,56]. In monolayer MoS_2 or other TMDCs, the lack of inversion symmetry and strong spin-orbit coupling lead to strong spin-orbit band splitting and spin-valley

locking effects [57,58]. All these characteristics make TMDCs highly promising for various applications such as transistors, optoelectronic, and valleytronic devices.

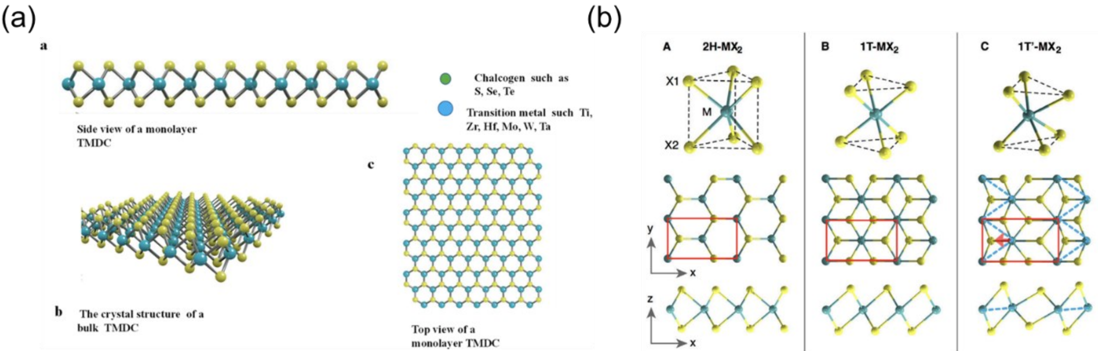

Fig. 1.11 (a) Crystal structure of TMDCs [59]. (b) Three phase structure of TMDCs [52].

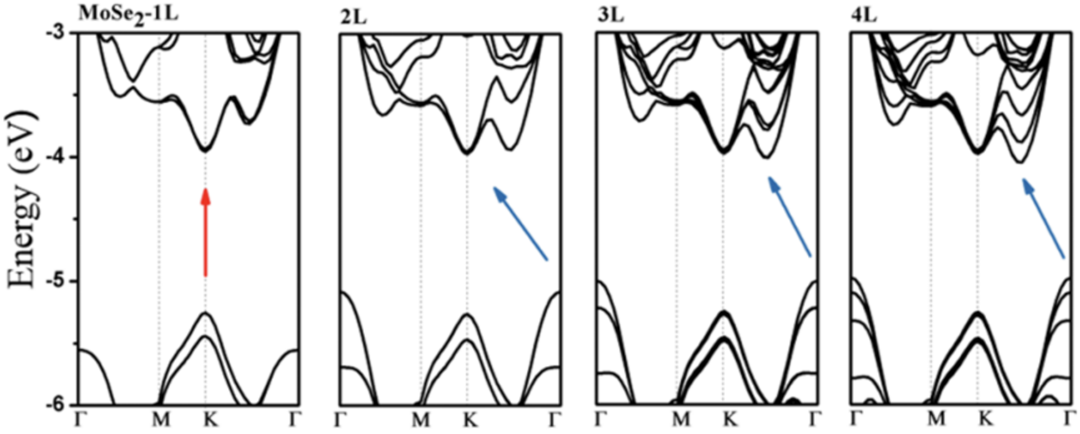

Fig. 1.12 Band gap evolution of $MoSe_2$ as a function of layer numbers [60].

1.4. 2D-FET

The scalability of transistors is correlated with the thickness of the channel material; The thinner channel material allows for higher scalability, as mentioned before. The thickness of traditional Si-based channels has already been reduced to 4 nm; further thinning would result in a significant decrease in mobility. 2D-FETs are a type of transistor structure based on 2D materials. The basic principle of 2D-FET is similar to that of traditional transistors, where the core function is to regulate the flow of current between the source and drain by controlling the gate electric field. In 2D-FETs, 2D

materials such as graphene, black phosphorus, and TMDCs are commonly used as semiconductor channels. When a voltage is applied to the gate electrode, it generates an electric field on the surface of the 2D material, thereby adjusting the carrier concentration in the channel and consequently controlling the current between the source and drain. **Figure 1.13** shows the typical structures of the bake-gated and top-gated 2D-FET. Unlike Si-MOSFETs, which operate in the inversion state, 2D-FETs operate in the accumulation state [61]. Due to their atomic-level thickness and excellent electrostatic properties, 2D-FETs can significantly suppress short-channel effects compared to Si-MOSFETs. Additionally, 2D materials have several advantages [62]: 1) High mobility enables high-speed carrier transport, thus improving device performance; 2) Tunable bandgap can meet various device requirements; 3) High on-off ratio and low leakage current meet low-power requirements. 4) Due to the flexibility of 2D materials, they are suitable for the application of flexible electronic devices such as wearable devices and flexible displays. Among 2D materials, graphene-FET generally exhibits a low on-off ratio due to its lack of bandgap or insufficient bandgap induced by external conditions, making it unsuitable for transistor applications. Black phosphorus, as an outstanding 2D material, has been extensively researched for transistor applications [63], but its instability in the ambient limits its application. TMDC materials, due to their excellent electric properties and stability, have emerged as the prime candidates for next-generation channel materials.

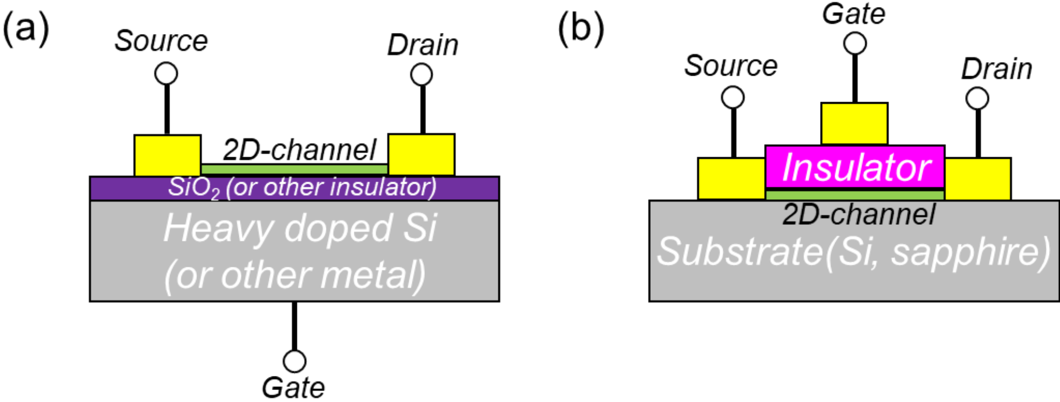

Fig. 1.13 (a) Back-gated 2D-FET. (b) Top-gated 2D-FET.

MoS_2 is the most typical TMDC material with a bandgap of 1.8 eV in monolayer and 1.2 eV in multilayer, and it is commonly used as an n-channel material for FET application, as shown in **Fig. 1.14 (a)**. MoS_2-FET exhibits high on-state current and low off-state current characteristics, with an on/off ratio exceeding 10^{10}; MoS_2 has a high electron mobility. A previous study has reported that mobility in MoS_2-FET reached 150 cm^2/Vs [64]. Compared to other TMDC materials, MoS_2 shows relatively greater ease in forming Ohmic contacts with metals and exhibits lower contact resistance. The lowest contact resistance achieved for MoS_2-FET in experiments is 42 ohms by using Sb semimetal contact [65]. However, since logic devices require complementary p-channel transistors and MoS_2 itself is difficult to form a p-channel due to the Fermi level pinning effects [66], WSe_2 has emerged as a p-channel material, as shown in **Fig. 1.14 (b)**. WSe_2 has a bandgap of 1.6 eV in monolayer and 1.2 eV in multilayer. Due to its small electron affinity (~ 3.6 eV), WSe_2 is easier to form a p-channel. However, to match the performance of MoS_2-FET, the formation of Ohmic contacts and low contact resistance for WSe_2-FET are urgently needed [67].

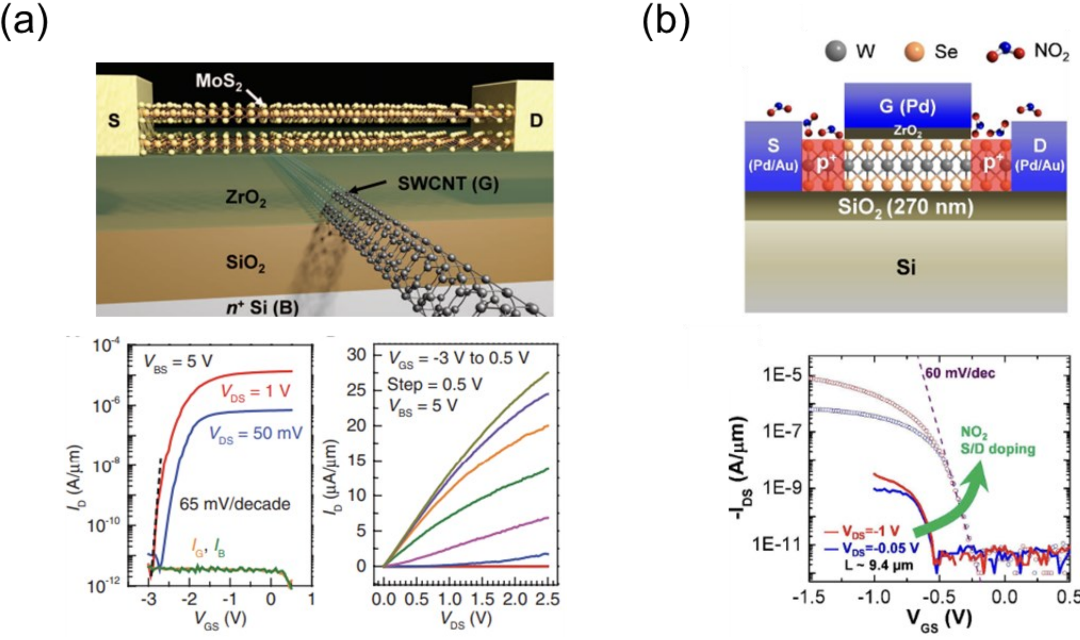

Fig. 1.14 (a) MoS_2-FET with a SWCNT gate [68]. (b)WSe_2-FET with chemically doped contacts [69].

1.5. Fermi level pinning effect

The properties of metal-semiconductor contact play a critical role in the performance of FETs. It can be classified into two types: Ohmic and Schottky contacts. In ideal conditions, the type of contact is determined by the difference in energy between the metal's work function (Φ_m) and the electron affinity (χ_s) or valence band energy of the semiconductor. For an n-type semiconductor, if the metal's work function is lower than the semiconductor's electron affinity, electrons will flow from the metal's Fermi level into the semiconductor's surface after contact. This results in a bending of the energy band at the semiconductor surface, forming an n-type degenerate region. Under applied voltage, electrons can flow freely without encountering a barrier, leading to low contact resistance, which is referred to as an Ohmic contact, as shown in **Fig. 1.15 (a)**. Conversely, when the metal's work function exceeds the semiconductor's electron affinity, the Fermi levels of both align upon contact, creating a barrier at the contact surface known as the Schottky barrier, which can be extracted from the difference between the metal's work function and semiconductor's electron affinity ($\Phi_{BN} = \Phi_m - \chi_s$). Under applied voltage, electrons must overcome this barrier to flow, resulting in significantly high contact resistance. This situation is termed a Schottky contact. In the case of p-type semiconductors, the Ohmic contact will be formed when it contacts a metal with a larger work function than its valence band. Otherwise, a Schottky barrier will form at the interface, as shown in **Fig. 1.15 (b)**. The Schottky barrier is given by $\Phi_{BP} = \chi_s + E_g - \Phi_m$. The method of extracting the Schottky barrier in this way is called the Schottky−Mott rule [66].

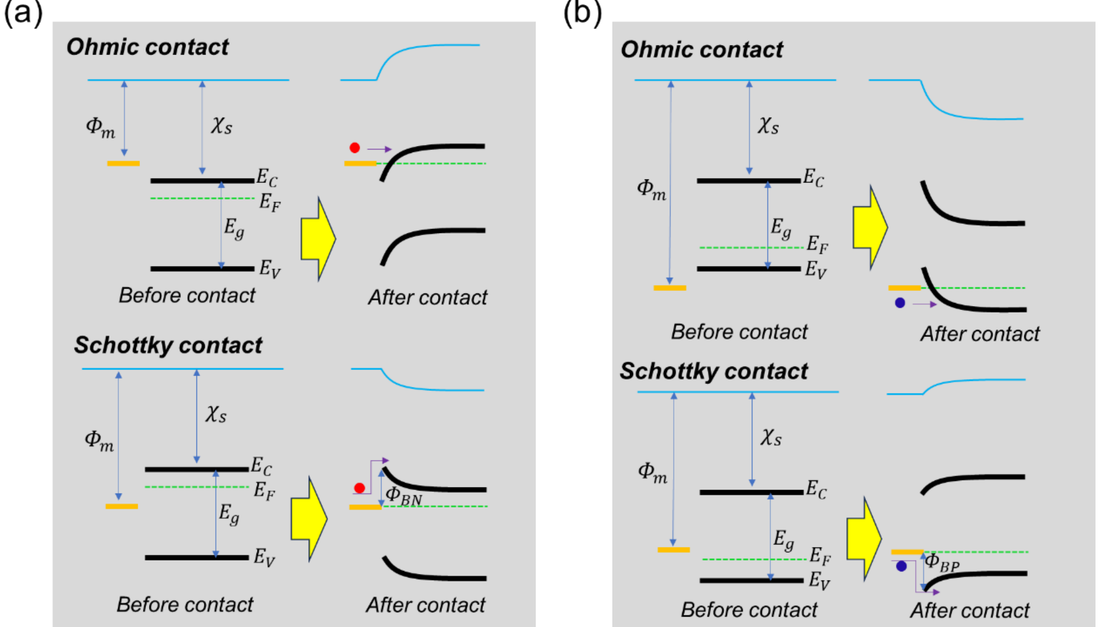

Fig. 1.15 (a) Band evolution of Ohmic and Schottky contact between the n-type (a) and p-type (b) semiconductor.

However, in practical situations, achieving Ohmic contacts, especially for 2D semiconductor materials, cannot be realized simply by selecting metals. Traditional metal contacts introduce numerous interface states on the semiconductor surface, leading the Fermi level of the metal to consistently align with a fixed position within the semiconductor bandgap after contact, as shown in **Fig. 1.16**. This phenomenon, known as the Fermi level pinning (FPL) effect, renders the contact properties independent of the metal's work function. There are three main reasons for the formation of interface states. Firstly, the wave functions of electrons near the metal's Fermi level can penetrate into the semiconductor, causing a rehybridization of the semiconductor's original wave functions and thus forming some new states within the bandgap, known as metal induced gap states (MIGS) [70]. Secondly, during the metal deposition process, the high energy can induce defects on the semiconductor surface, and the inherent defects in the semiconductor itself can introduce defect energy levels within the bandgap. This phenomenon is referred to as the unified defect model (UDM) [71]. Thirdly, impurity levels with a continuous distribution at the semiconductor interface can also contribute to the FLP effect, termed the Disorder Induced Gap State

(DIGS) [72]. In reality, the factors contributing to the formation of interface states are complex, and further research is needed to understand the underlying principles. The FLP effect deviates from the Schottky barrier extraction from the Schottky−Mott rule. In that case, the Schottky barrier is characterized quantitatively by introducing a pinning factor (*S*) and charge neutrality level (CNL, Φ_{CNL}) [66].

$$\Phi_{BN} = S(\Phi_m - \Phi_{CNL}) + (\Phi_{CNL} - \chi_s) \tag{1.6}$$

$$\Phi_{BP} = S(\Phi_m - \Phi_{CNL}) + \left(E_g - \Phi_{CNL} + \chi_s\right) \tag{1.7}$$

$$S = \frac{d\Phi_B}{d\Phi_m} \tag{1.8}$$

S varied from 1 or -1 for an unpinned interface to 0 for a strongly pinned interface. CNL is defined as the energy above which the states of a neutral surface are empty. In other words, the CNL is the energy at which the Fermi level of a metal is pinned. When $0 < |S| < 1$, the Schottky barrier can only be extracted through the thermionic emission equation, which will be explained later.

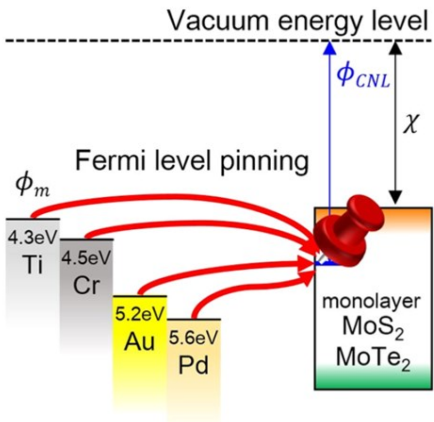

Fig. 1.16 Schematic diagram of Fermi level pinning [66].

1.6. 2D-TFET

As discussed before, the BTBT-dominated carrier transport in TFET leads to an I_{on}, usually a few orders of magnitude smaller than the conventional MOSFETs. It should be noted that both *SS* and I_{on} of TFET are determined by the probability of BTBT, which is strongly dependent on the device's electrostatics and semiconductor material

properties. Thus, the device design and materials for TFET are paramount to practically achieving extremely small *SS* and acceptable I_{on}. The 2D crystalline semiconductors are being actively studied as a channel material for the FETs because of their excellent electric properties, as stated before. According to the WKB approximation, thinner channel materials can increase the tunneling probability in TFETs, thereby enhancing device current; thus, 2D materials with atomic thickness promise to increase device current in TFETs. Additionally, the absence of dangling bonds on the surface provides a high-quality interface when in contact with other 2D materials such as 2D-insulator. These unique attributes present an opportunity to introduce 2D materials for TFET design that can simultaneously incorporate the advantages of superior electrostatic integrity and tunneling barrier engineering. Hence, the field of 2D-TFET design has substantially grown in recent years. Specifically, the 2D-TFETs are being considered the promising candidate for the nanoscale device dimensions where the channel lengths are typically ≤ 40 nm, leading to ballistic/quasi-ballistic carrier transport in the channel. Specifically, 2D-TFETs are considered promising candidates for nanoscale device sizes, where the channel length is typically ≤40 nm, resulting in ballistic/quasi-ballistic carrier transport in the channel [73].

Currently, there are two types of TFET structures based on 2D materials. One is the lateral structure (homojunction) shown in **Fig. 1.9 (a)**, and the other is the bilayer vertical structure (heterojunction) shown in **Fig. 1.9 (c)**. Each structure has advantages and disadvantages. The lateral structure allows a single material to realize both n and p-channel TFETs, simplifying the integration process. However, the tunneling area is limited, and achieving a sharp doping profile in the source-channel region is challenging. The vertical structure typically consists of heterojunctions formed by two different materials. This structure offers a larger tunneling area and fewer tunneling interface states, enabling higher BTBT current. However, the complexity of the structure significantly increases the integration difficulty. Additionally, achieving both n- and p-channel TFETs simultaneously requires multiple materials, leading to extremely challenging fabrication processes. Liu W. group has demonstrated a TFET based on 2D/3D vertical heterostructure including a TMDC material (MoS_2) as the

channel and heavily p-doped Ge as the source [74]. This TFET showed a small *SS* over four decades of drain current, as shown in **Fig. 1.15 (a)**. A major feature of this work is establishing a connection between 2D and 3D materials. Since 2D materials must be mounted on a substrate to be fabricated into devices, this work cleverly incorporates the substrate directly as part of the device. One advantage of this approach is the potential for large-scale integration, as 2D materials can be directly grown on 3D semiconductor wafers like Si or Ge. Meanwhile, TFETs based on 2D/2D heterostructures have also been extensively fabricated. A typical example involves utilizing p-doped WSe_2 by ozone-treating as the source and pristine MoS_2 as the channel to achieve TFET operation [75], as shown in **Fig. 1.15 (b)**. However, steep *SS* over a wide range of currents has not yet been realized. Compared to the vertical heterostructure, the fabrication of TFETs based on lateral homogeneous structures is relatively less due to limitations in doping techniques for 2D materials. However, Shin, W. group successfully fabricated n- and p-channel TFETs by using the feature of black phosphorus, where the bandgap and electrical properties changed with the thickness [76]. They achieved record-low average *SS* over 4~5 decades of current and record-high I_{60} (the current value at SS = 60 mV/dec), as shown in **Fig. 1.15 (c)**.

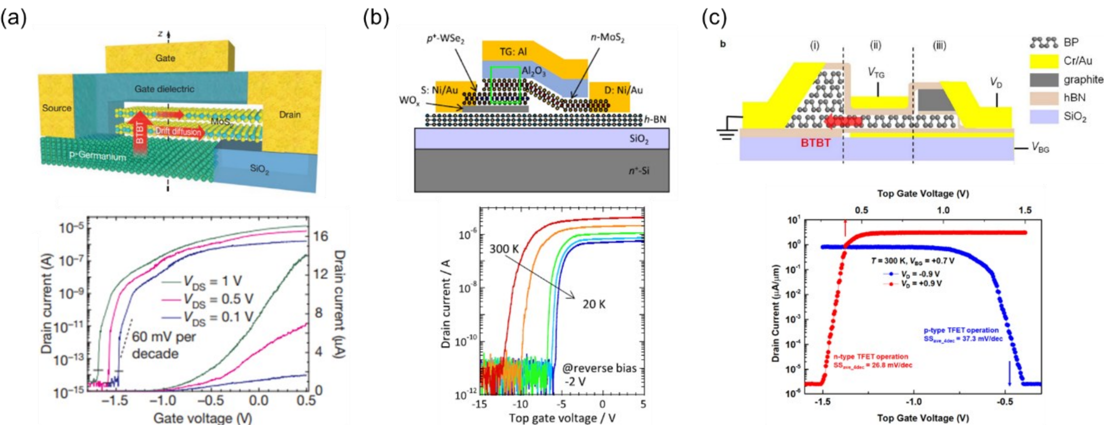

Fig. 1.15 (a) Ge/MoS_2 -TFET [74]. (b)WSe_2/ MoS_2-TFET [75]. (c) Homojunction BP-TFET [76].

1.7. Recent studies on $MoTe_2$

1.7.1. Polycrystalline characteristic

$MoTe_2$ is a layered TMDC material composed of the transition metal element Mo and the chalcogen element Te. It is arranged in a triangular prism shape and exhibits a stable structure in the 2H phase. Mo and Te atoms are linked by covalent bonds, while the layers are held together by weak van der Waals forces. $MoTe_2$ has a polymorphism feature that has a 2H structure of a semiconducting phase and a 1T' (1T) structure of a semi-metallic one. 1T'-$MoTe_2$ transforms into the T_d phase around 250 K and exhibits superconducting characteristics under extremely low-temperature conditions, which has caused extensive research [77,78]. A theoretical study suggests that the stability of $MoTe_2$ in the 1T' structure is superior to that in the 1T structure; hence the semi-metallic phase of $MoTe_2$ generally exists in the 1T' structure [79]. However, Bartels, L. group successfully employed CVD methods to grow three different phase structures of $MoTe_2$ by varying the cool-down temperatures and measuring the Raman spectra of each phase [80], as shown in **Figs. 1.16 (a) and (b)**. **Figure 1.17** shows the band structure calculations of three $MoTe_2$ phases in a monolayer. Regardless of whether 1T' or 1T phase, the maximum valence band is higher than the minimum conduction band, resulting in an electron structure with band overlap, thus exhibiting the characteristics of a semimetal.

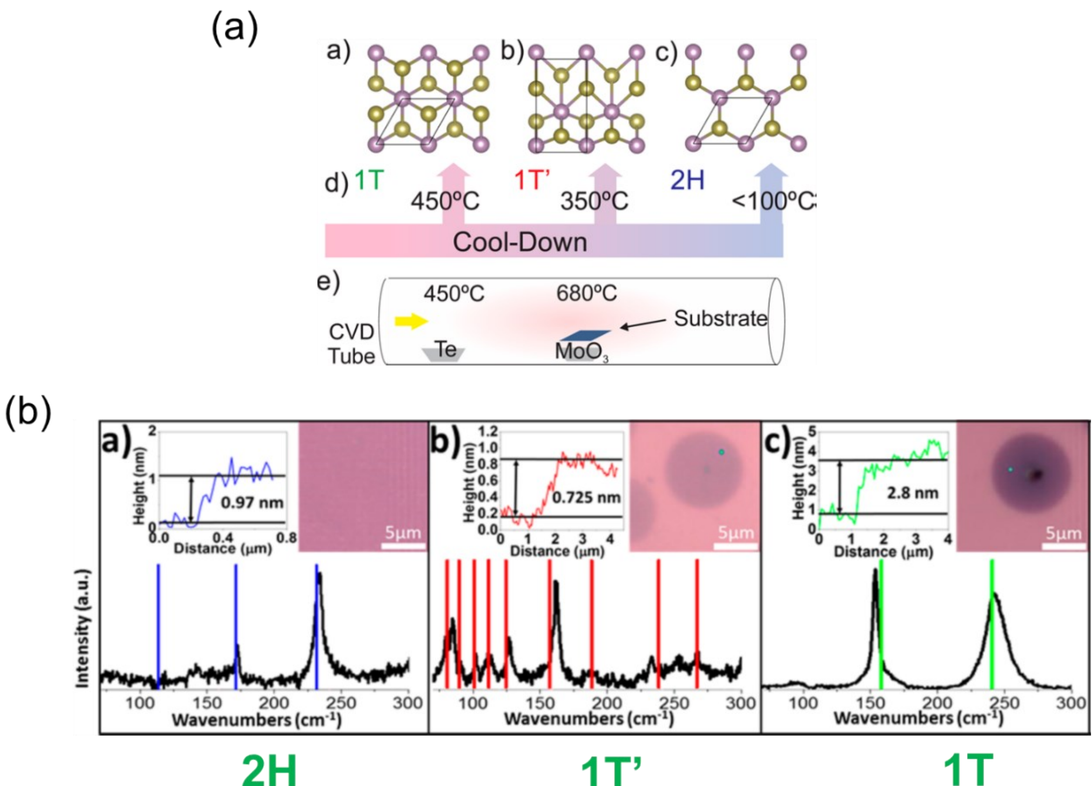

Fig. 1.16 (a) $MoTe_2$ phases and overview of CVD preparative technique [80]. (b) Comparison of the experimental (black) Raman spectra for each phase of $MoTe_2$ with computational predictions (colored lines) [80].

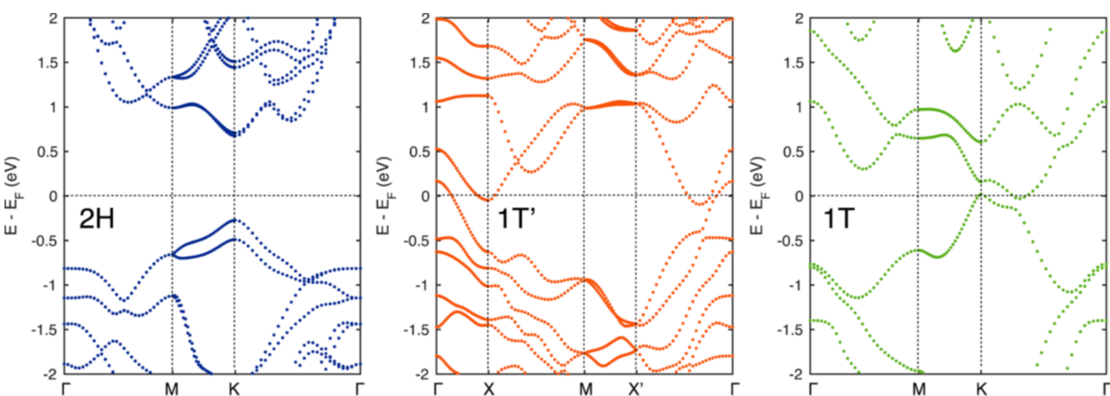

Fig. 1.17 band structures calculations of three $MoTe_2$ phases in monolayer [80].

1.7.2. $MoTe_2$-FET and TFET

2H-$MoTe_2$ has a direct bandgap of 1.1 eV in monolayer and an indirect bandgap of 0.88 eV in multilayer or bulk. Due to the small bandgap, original 2H-$MoTe_2$ FETs typically exhibit ambipolar behavior that can turn both the n- and p-FET operation on by applying positive and negative gate voltage [81]. However, 2H-$MoTe_2$ can be easily doped, enabling the formation of transistors dominated by either n- or p-channels [822]. **Figure 1.18** shows the three types of transfer characteristics of 2H-$MoTe_2$ FETs. Its advantage lies in the ability to achieve transistors of opposite polarity on the same material, similar to Si, while its disadvantages include poor stability of monolayer and relatively high ambipolar current at room temperature. The performance of 2H-$MoTe_2$ FETs is also limited by poor contact properties caused by serious FLP effect. Many previous studies have been conducted to improve contact properties. For example, de-pinning interfaces are fabricated by inserting an insulating layer such as monolayer *h*-BN or Al_2O_3 between metal and 2H-$MoTe_2$ [83,84]. Moreover, 1T'-$MoTe_2$ was used as an electrode instead of a metal contact with 2H-$MoTe_2$ via a 1T'/2H/1T' homojunction, and it shows a low contact resistance and ohmic carrier injunction [85~87]. Additionally, the phase transition in $MoTe_2$ is easily realized under external conditions, transitioning from a semiconducting phase to a semimetal phase. This feature may be utilized to optimize processes in integrated circuits [88].

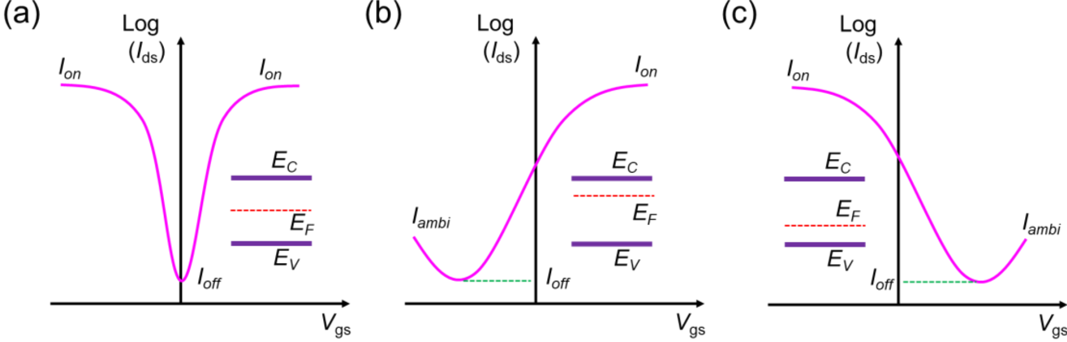

Fig. 1.18 Three types of transfer characteristics of 2H-$MoTe_2$ FETs: (a) ambipolar FET. (b) n-type dominated FET. (c) p-type dominated FET.

According to the WKB approximation, a smaller bandgap can result in a larger tunneling current. The few-layer or multilayer $MoTe_2$ has a bandgap of only 0.88 eV,

which is smaller than that of most TMDC semiconductor materials. Moreover, its ambipolar characteristics enable the simultaneous preparation of n- and p-channel TFETs, which shows itself to be a much more suitable candidate for TFET applications. In addition, compared to other TMDC materials, $MoTe_2$ can be easily doped through some methods, allowing it to be used not only to fabricate TFETs with the homojunction structure shown in **Fig. 1.9 (a)** but also as the source material in TFETs with the heterojunction structure shown in **Fig. 1.9 (c)**, providing carriers for the device. A dual-gated $MoTe_2$-TFET with a homojunction was reported in 2021 [89]. In this structure, the $MoTe_2$ was divided into two parts of n- and p-type by applying opposite voltages in the globe back gate and top gate; thus, a tunneling window can be formed, and an average *SS* of 46 mV/dec over four decades drain current was obtained at 300 K, as shown in **Fig. 1.19 (a)**. In addition, a heterostructure of $MoTe_2/MoS_2$ has successfully realized the TFET operation with $MoTe_2$ as source and MoS_2 as channel, which was reported by Choi S. Y. group [90], as shown in **Fig. 1.19 (b)**. For vertical heterostructure-based 2D-TFETs, band alignment is crucial. Typically, to achieve a high on/off ratio in TFETs, the initial band alignment of the two materials is required to be of type 2. By applying drain and gate biases, the band alignment evolves into type 3, allowing the device to turn on. **Fig. 1.20** illustrates several typical TMDC materials' band alignments in monolayer. Due to $MoTe_2$ having a shallow valence band, it is suitable as the heavy p-doped source material w for n-channel TFETs.

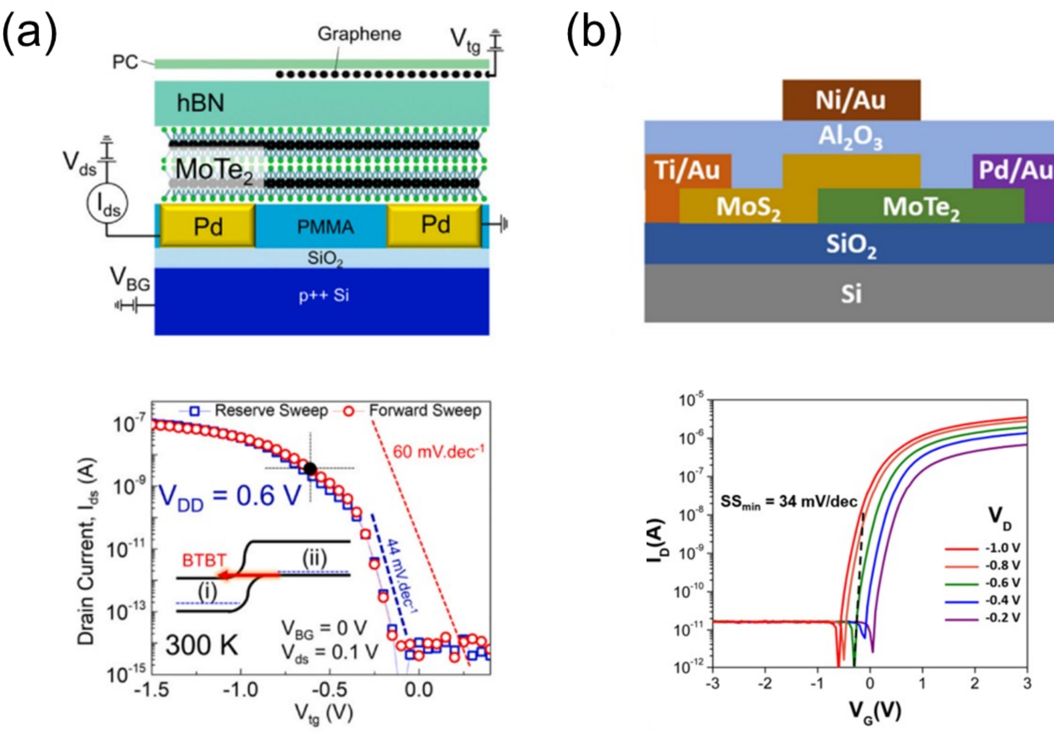

Fig. 1.19 (a) $MoTe_2$-TFET with a homojunction structure [89]. (b) 2D-TFET with a $MoTe_2$/MoS_2 vertical heterojunction [90].

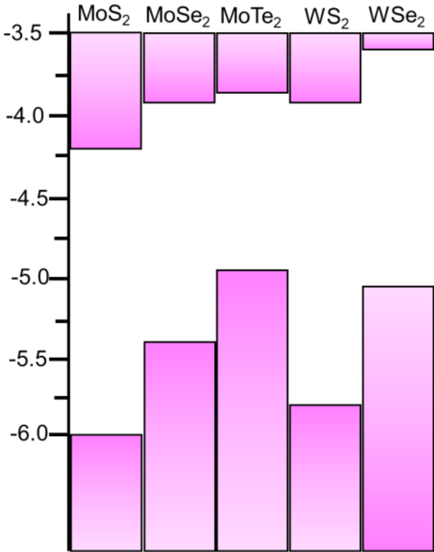

Fig. 1.20 Calculated band alignment for TMDC monolayers (made by referring [91]).

1.7.3. Laser irradiation for $MoTe_2$

Since the report by the S. Cho group in 2015 on the transformation of the semiconductor phase (2H) of $MoTe_2$ to a semimetal phase (1T') through laser irradiation in the atmosphere [92], numerous researchers have turned their attention to the effects of laser irradiation on 2D crystals, particularly $MoTe_2$. Due to the instability of Te atoms in $MoTe_2$, laser irradiation can induce local heating and thermal conduction, leading to lattice deformation and the formation of defects, thereby altering the electrical properties of $MoTe_2$. The electrical conductivity, carrier concentration, and electronic structure of $MoTe_2$ can be controlled through laser-induced local oxidation or strain. This modulation of electrical properties contributes to the adjustment and optimization of device performance. Currently, laser irradiation is utilized to modulate the electrical properties of $MoTe_2$, mainly in two aspects. Firstly, low-intensity laser irradiation on $MoTe_2$ in the atmosphere can induce p-doping effects by forming a MoO_x layer with a high work function on the surface through charge transfer mechanisms, which was reported by R. Liu group [93]. Secondly, several studies of phase transition control by laser irradiation for $MoTe_2$ have been reported. Laser irradiation with appropriate intensity on $MoTe_2$ in the atmosphere leads to phase transition from the 2H semiconductor phase to the 1T' metallic phase accompanied by the layer-thinning phenomenon, and the laser-induced 1T' phase shows a good contact property with the original 2H phase [92], as shown in **Fig. 1.21 (a)**. However, it has also been reported that the product of this transition may be a thermally decomposed Te layer because the Raman spectrum of the laser-irradiated region is similar to Te, as shown in **Fig. 1.21 (b)** [94]. In summary, laser-induced modulation of the electrical properties of 2D materials is a rapid and effective method. The application of laser technology in the field of 2D materials is of paramount significance.

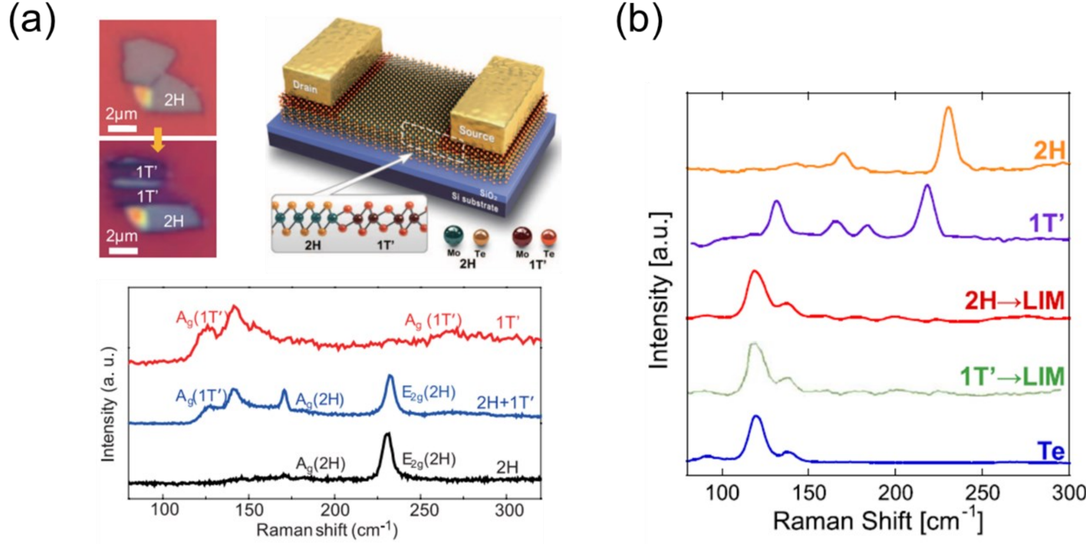

Fig. 1.21 (a) Phase transition of $MoTe_2$ by laser irradiation [92]. (b) Raman spectra. From top to bottom: 2H-$MoTe_2$, thermally grown 1T′-$MoTe_2$, laser-induced-metal (LIM) phase from 2H, LIM phase from 1T′, and Te crystal [94].

Reference

[1] F. Schwierz and J. J. Liou, 2020 IEEE Latin America Electron Devices Conference (LAEDC). IEEE 1 (2020).
[2] A. Samal, S. L. Tripathi and S. K. Mohapatra, IEEE Trans Electron Devices **21**, 443 (2020).
[3] R. K. Ratnesh, A. Goel, G. Kaushik, et al. Mater Sci Semicond Process **134**, 106002 (2021).
[4] D. L. Critchlow. Proceedings of the IEEE **87**, 659 (1999).
[5] https://www.ncbi.nlm.nih.gov/books/NBK321721/figure/oin_tutorial.F3/
[6] W. Bae. Journal of Low Power Electronics and Applications **9,** 26 (2019).
[7] Khanna, Vinod Kumar, and Vinod Kumar Khanna. Integrated Nanoelectronics: Nanoscale CMOS, Post-CMOS and Allied Nanotechnologies, 73-93 (2016).
[8] Q. Xie, J, Xu, Y. Taur, IEEE transactions on electron devices **59**, 1569 (2012).
[9] R. H. Yan, A. Ourmazd and K. F. Lee, IEEE transactions on electron devices **39**, 1704 (1992).
[10] W. Cao, H. Bu, M. Vinet, et al. Nature **620**, 501(2023).
[11] S. Iijima, T. Ichihashi, Nature **363,** 603 (1993).
[12] S. B. Desai, S. R. Madhvapathy, A. B. Sachid, et al. Science **354**, 99 (2016).
[13] Seiji Nagahara / Tokyo Electron Ltd. / Sep. 5, 2023/ SSDM 2023 Short Course A
[14] S. W. Sun and P. G. Y. Tsui. IEEE Journal of solid-state circuits **30**, 947(1995).

[15] D. A. Antoniadis and A. Khakifirooz, 2008 IEEE International Electron Devices Meeting. IEEE, pp. 1-4 (2008).
[16] A. Rjoub, M. Mistarihi and N. Al Taradeh, International Journal of Electrical and Computer Engineering **10**, 2313 (2020).
[17] V. K. Sharma, Australian journal of electrical and electronics Engineering **18**, 217 (2021).
[18] K. Tomioka, H. Gamo, J. Motohisa, et al. 2020 IEEE International Electron Devices Meeting, pp. 21-1 (2020).
[19] G. Nazir, A. Rehman and S. J. Park, ACS applied materials & interfaces **12**, 47127 (2020).
[20] N, Mendiratta and S. L. Tripathi, Journal of Semiconductors **41**, 061401 (2020).
[21] S. Kanungo, G, Ahmad, P. Sahatiya, et al. npj 2D Materials and Applications **6**, 83 (2022).
[22] S. Kim, G. Myeong, J. Park, et al. Nano Letters **20**, 3963 (2020).
[23] G. V. Luong, S. Strangio, A. T. Tiedemann, et al. IEEE journal of the Electron Devices Society **6**, 1033 (2018).
[24] Q. T. Zhao, S. Richter, C. Schulte-Braucks, et al. IEEE Journal of the Electron Devices Society **3**, 103 (2015).
[25] M. Hemmat, M. Kamal, A. Afzali-Kusha, et al. Solid-State Electronics **124**, 46 (2016).
[26] Qing-Tai Zhao / PGI 9, Forschungszentrum Jülich, / Sep. 5, 2023/ SSDM 2023 Short Course A
[27] C. Y. Chen, T. A. Ameen, H. Ilatikhameneh, et al. IEEE Transactions on Electron Devices **65**, 4614 (2018).
[28] C. Y. Chen, H. Y. Tseng, H. Ilatikhameneh, et al. IEEE Transactions on Electron Devices **68**, 3104 (2021).
[29] 高木信一**.** ”トンネル FET への期待と将来展望**.**” 応用物理 **88**, 382 (2019).
[30] G. V. Luong, K. Narimani, A. T. Tiedemann, et al. IEEE electron device letters **37**, 950 (2016).
[31] R. Takaguchi, R. Matsumura, T. Katoh, et al. Japanese Journal of Applied Physics **57**, 04FD10, (2018).
[32] A. Alian, J. Franco, A. Vandooren, et al. 2015 IEEE International Electron Devices Meeting **31**, pp. 31-7 (2015).
[33] S. M. T. Azam, A. S. M. Bakibillah, M. T. Hasan, et al. Nanomaterials **11**, 3166 (2021).
[34] K. Kato, H. Matsui, H. Tabata, et al. IEEE Journal of the Electron Devices Society **7**, 1201 (2019).
[35] D. R. Cooper, B. D'Anjou, N. Ghattamaneni, et al. International Scholarly Research Notices, (2012).
[36] N. Briggs, S. Subramanian, Z. Lin, et al. 2D Materials **6**, 022001 (2019).
[37] T. Tan, X. Jiang, C. Wang, et al. Advanced Science **7**, 2000058 (2020).
[38] J. R. Schaibley, H. Yu, G. Clark, et al. Nature Reviews Materials **1**, 1 (2016).
[39] S. Das, D. Pandey, J. Thomas, et al. Advanced Materials **31**, 1802722 (2019).
[40] H. R. Ansari, A. Mirzaei, H. Shokrollahi, et al. Journal of Materials Chemistry C

(2019).
[41] S. Li, L. Ma, M. Zhou, et al. Current Opinion in Biomedical Engineering **13**, 32 (2020).
[42] W. Wang, N. Clark, M. Hamer, et al. Nature Electronics **6**, 981 (2023).
[43] S. D. Sarma, S. Adam, E. H. Hwang, et al. Reviews of modern physics **83**, 407 (2011).
[44] S. Pathania, P. Gupta, R. Kumar, et al. 2021 IEEE Bombay Section Signature Conference (IBSSC). pp. 1-6 (2021).
[45] P. Tiwari, S. K. Srivastav, A. Bid, Physical Review Letters **126**, 096801 (2021).
[46] M. W. Roberts, C. B. Clemons, J. P. Wilber, et al. Journal of nanotechnology (2010).
[47] F. Hui, C. Pan, Y. Shi, et al. Microelectronic Engineering **163**, 119 (2016).
[48] J. Meng, D. Wang, L. Cheng, et al. Nanotechnology **30**, 074003 (2018).
[49] M. Salavati, A. Mojahedin, A. H. N. Shirazi, Frontiers of Structural and Civil Engineering **14**, 623 (2020).
[50] D. Wickramaratne, L. Weston and C. G. Van de Walle, The Journal of Physical Chemistry C **122**, 25524 (2018).
[51] M. Houssa, A. Dimoulas, and A. Molle, eds. 2D materials for nanoelectronics **17**, CRC Press (2016).
[52] X. Qian, J. Liu, L. Fu, et al. Science **346**, 1344 (2014).
[53] J. Qi, X. Li, X. Qian, et al. Applied Physics Letters **102,** 173112 (2013).
[54] D. Lloyd, X. Liu, J. W. Christopher, et al. Nano letters **16**, 5836 (2016).
[55] E. Navarro-Moratalla, J. O. Island, S. Manas-Valero, et al. Nature communications **7**, 11043 (2016).
[56] S. Krishnamurthi and G. Brocks. Physical Review B **102**, 161106 (2020).
[57] A. Kormányos, V. Zólyomi, N. D. Drummond, et al. Physical Review X **4**, 011034 (2014).
[58] C. J. Ciccarino, T. Christensen, R. Sundararaman, et al. Nano letters **18**, 5709 (2018).
[59] P. O. Fadojutimi, S. S. Gqoba, Z. N. Tetana, et al. Catalysts **12**, 468 (2022).
[60] Y. Sun, D. Wang and Z. Shuai, The Journal of Physical Chemistry C **120**, 21866 (2016).
[61] N. Fang and K. Nagashio. ACS applied materials & interfaces **10**, 32355 (2018).
[62] X. Cai, Y. Luo, B. Liu, et al. Chemical Society Reviews **47**, 6224 (2018).
[63] W. C. Tan, L. Wang, X. Feng, et al. Advanced Electronic Materials **5**, 1800666 (2019).
[64] Z. Yu, Z. Y. Ong, Y. Pan, et al. arXiv preprint arXiv **1510**, 00830 (2015).
[65] W. Li, X. Gong, Z. Yu, et al. Nature **613**, 274 (2023).
[66] C. Kim, I. Moon, D. Lee, et al. ACS nano **11**, 1588 (2017).
[67] H. J. Chuang. Two-dimensional low-resistance contacts for high performance WSe_2 and MoS_2 transistors. Wayne State University (2016).
[68] S. B. Desai, S. R. Madhvapathy, A. B. Sachid, et al. Science **354**, 99 (2016).
[69] H. Fang, S. Chuang, T. C. Chang, et al. Nano letters **12**, 3788 (2012).
[70] K. Sotthewes, R. Van Bremen, E. Dollekamp, et al. The Journal of Physical Chemistry C **123**, 5411 (2019).

[71] Y. Ishikawa, N. Tsurumi, T. Fukui, et al. Journal of Vacuum Science & Technology B: Microelectronics and Nanometer Structures Processing, Measurement, and Phenomena, **16**, 2387 (1998).
[72] H. Hasegawa and H. Ohno. Journal of Vacuum Science & Technology B: Microelectronics Processing and Phenomena **4**, 1130 (1986).
[73] S. Kanungo, G. Ahmad, P. Sahatiya, et al. npj 2D Materials and Applications **6**, 83 (2022).
[74] D. Sarkar, X. Xie, W. Liu, et al. Nature **526**, 91 (2015).
[75] K. Nakamura, N. Nagamura, K. Ueno, et al. ACS Applied Materials & Interfaces **12**, 51598 (2020).
[76] S. Kim, G. Myeong, W. Shin, et al. Nature nanotechnology **15**, 203 (2020).
[77] Y. Cheon, S. Y. Lim, K. Kim, et al. ACS nano **15**, 2962 (2021).
[78] R. Beams, L. G. Cançado, S. Krylyuk, et al. ACS nano **10**, 9626 (2016).
[79] M. Kan, H. G. Nam, Y. H. Lee, et al. Physical Chemistry Chemical Physics **17**, 14866 (2015).
[80] T. A. Empante, Y. Zhou, V. Klee, et al. ACS nano **11**, 900 (2017).
[81] Y. F. Lin, Y. Xu, S. T. Wang, et al. Advanced Materials **26**, 3263 (2014).
[82] Y. M. Chang, S. H. Yang, C. Y. Lin, et al. Advanced Materials **30**, 1706995 (2018).
[83] M. J. Mleczko, A. C. Yu, C. M. Smyth, et al. Nano letters **19**, 6352 (2019).
[84] Y. J. Park, A. K. Katiyar, A. T. Hoang, et al. Small **15**, 1901772 (2019).
[85] S. Yang, X. Xu, W. Xu, et al. ACS Applied Nano Materials **3**, 10411 (2020).
[86] X. Zhang, Z. Jin, L. Wang, et al. ACS applied materials & interfaces **11**, 12777 (2019).
[87] R. Ma, H. Zhang, Y. Yoo, et al. ACS nano **13**, 8035 (2019).
[88] X. Yin, C. S. Tang, Y. Zheng, et al. Chemical Society Reviews **50**, 10087 (2021).
[89] N. T. Duong, C. Park, D. H. Nguyen, et al. Nano Today **40**, 101263 (2021).
[90] B. Koo, G. H. Shin, H. Park, et al. Journal of Physics D: Applied Physics **51**, 475101(2018).
[91] S. Lee, Z. Zhong. Nanoscale **6**, 13283 (2014).
[92] S. Cho, S. Kim, J. H. Kim, et al. Science **349**, 625 (2015).
[93] J. Chen, J. Zhu, Q. Wang, et al. Small **16**, 2001428 (2020).
[94] K. Sakanashi, H. Ouchi, K. Kamiya, et al. Nanotechnology **31**, 205205 (2020).

2. Experimental method

2.1. Exfoliation process

Currently, growth techniques such as chemical vapor deposition (CVD) and molecular beam epitaxy (MBE) have made significant progress in the production of 2D material flakes, allowing for wafer-scale growth of monolayer 2D material, which accelerates the application of 2D semiconductor materials in integrated circuits [1~3]. However, high growth temperatures resulting in high defect densities caused the quality of 2D crystals grown by these methods to be lower than those obtained by mechanical exfoliation. Additionally, the quality of 2D crystals is highly dependent on the substrate, limiting the choice of substrates in practical device fabrication. Although large-scale transfer can be achieved through wet transfer techniques, this inevitably introduces impurities, leading to a decrease in quality. Some heterostructure devices based on 2D materials require the transfer of a single crystal and the positioning adjustment of each crystal, rendering large-scale wet transfer impractical. Dry transfer techniques capable of transferring single crystals are difficult to employ due to the strong interaction between the grown crystal and the substrate, making it challenging to pick up the 2D crystal from the substrate. Although mechanical exfoliation is time-consuming and labor-intensive, the quality of the exfoliated crystals is very high, and crystals of different thicknesses can be chosen for device fabrication. Furthermore, due to the weak interaction between the exfoliated crystals and the substrate, various single nano-electronic devices can be easily fabricated using dry transfer techniques. Therefore, this study adopted the mechanical exfoliation method to obtain all the 2D materials used in device fabrication.

2.1.1. Exfoliation of graphene and *h*-BN

The bulk crystal of graphite was purchased from [HQ$^+$ Graphene] company, while the bulk crystal of *h*-BN was acquired from Professors K. Watanabe and T. Taniguchi, who are working at the National Institute for Materials Science (NIMS) in Japan. The exfoliation method of graphene and *h*-BN is as follows:

1. Place the cleaned and oxygen plasma-treated SiO_2/Si substrate on a hot plate and bake at 110 °C for 1 minute to remove residual water on the substrate surface, as shown in **Fig. 2.1 (a)**. Details about substrate cleaning and plasma treatment will be provided later.
2. Unfold a piece of Scotch tape and place a relatively large, flat bulk graphite on the tape. The bulk material of *h*-BN is in powder form, typically consisting of three to five powder crystals picked up with tweezers and placed concentratedly on the tape, as shown in **Fig. 2.1 (b)**.
3. Fold the tape with the graphite (*h*-BN) attached to one end, sticking the adhesive side of the tape together. Repeat the peeling process 10 to 15 times to transform the bulk into a thin crystal, as shown in **Fig. 2.1 (c)**. Be careful not to overlap the crystals during peeling.
4. Place the SiO_2 side of the baked substrate on the area of tape where the crystal is adhered, and gently wipe the surface with a cotton swab or tweezers to make the tape fully contact with the substrate. Wait for the substrate to return to room temperature, as shown in **Fig. 2.1 (d) and (e)**.
5. Once the substrate has returned to room temperature, slowly peel it off the tape, and a large number of crystals will adhere to the substrate, as shown in **Fig. 2.1(f)**.
6. Look for crystals of appropriate thickness under an optical microscope.
7. After exfoliation, organic residues of the tape may adhere to the surface of the substrate and crystals. Therefore, for graphene and *h*-BN crystals, the substrate is annealed in an Ar/H_2 mixed gas environment at 500 ºC for one hour to remove the organic residues after finding the target crystals. The gas flow rate is set to 1 L/min. **Figure 2.2** shows the surface difference between unannealed and annealed samples.

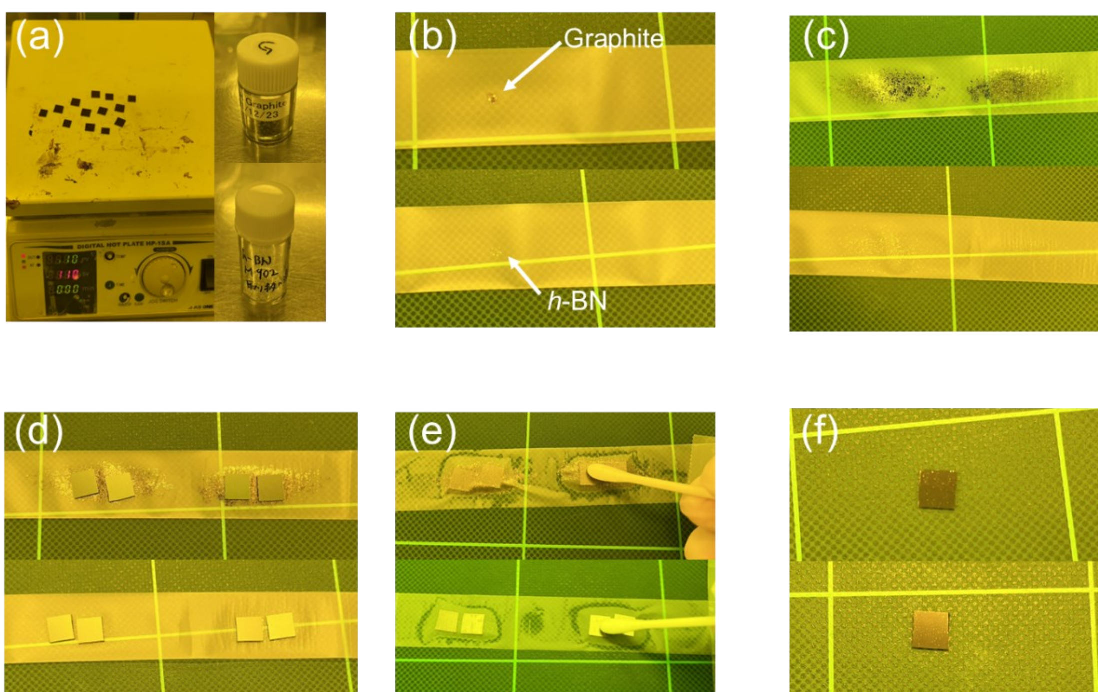

Fig. 2.1 Graphene/*h*-BN exfoliation process

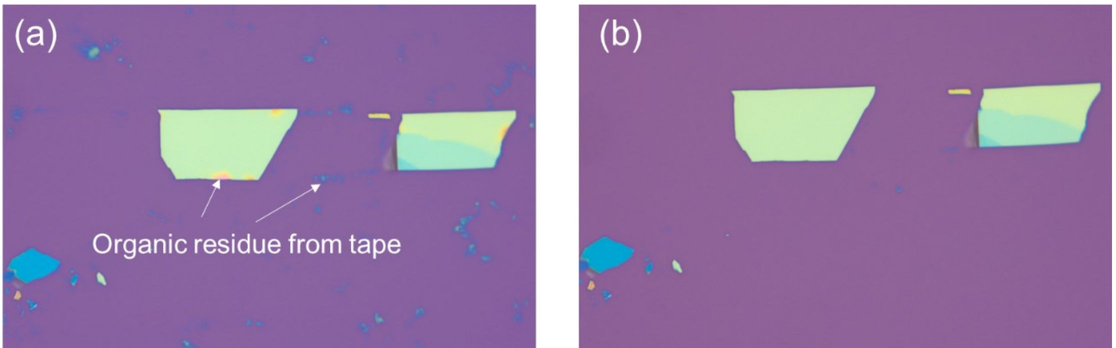

Fig. 2.2 *h*-BN crystal before (a) and after (b) Ar/H_2 annealing.

Exfoliation yields crystals of various thicknesses ranging from micrometers to hundreds of micrometers. The specific number of layers can be determined by the color contrast observed on the SiO_2/Si substrate. Conventionally, single-layer and two-layer crystals of graphite are referred to as monolayer and bilayer graphene, respectively, while crystals with three layers or more exhibit properties similar to bulk crystals and are referred to as graphite. In addition to color contrast, monolayer and bilayer graphene can also be accurately determined through Raman spectroscopy measurements. Raman

spectroscopy was performed using a JASCO RMP-510 spectrometer with an electron-cooled CCD camera, an Olympus BX-51 metallurgical microscope, and a DPSS green laser. The laser power was attenuated to approximately 0.65 mW to minimize damage to the crystals. Graphene typically exhibits G and 2D peaks near 1500 cm^{-1} and 2700 cm^{-1}, respectively. Monolayer and bilayer can be determined by observing the intensity ratio of these two peaks and the FWHM (Full Width Half Maximum) of the 2D peak. Since some devices in this study utilize multilayer graphite as a back gate, it is unnecessary to determine the exact thickness. Unlike graphene, due to its wide bandgap, *h*-BN can transmit through most visible light, making it difficult to determine the number of layers from single-layer to few-layer crystals based on color contrast under an optical microscope. Since *h*-BN with a thickness of less than 5 nm is easily broken down by an electric field, the thickness of the *h*-BN used in this study is approximately 10 ~ 60 nm, determined by color contrast.

2.1.2. Exfoliation of TMDCs

The exfoliation method for TMDC materials is generally similar to the above procedure but has three main differences. Firstly, blue tape was used for TMDC materials instead of Scotch tape. Blue tape is preferred because it leaves fewer organic residues on the substrate after exfoliation than Scotch tape. Due to the poor thermal stability of TMDC materials, they cannot undergo high-temperature annealing to remove organic residues left by Scotch tape; hence, blue tape with fewer residues is preferred. Secondly, the number of peeling times should be limited to prevent the exfoliated crystals from becoming too small, which would be detrimental to device fabrication. Typically, TMDC materials are peeled off 5 to 8 times in the exfoliation process. Third, due to the relatively low stickiness of the blue tape, after adhering the substrate to the tape, it needs to be placed on a hot plate at 70 ºC for one minute to ensure tight adhesion between the tape and the substrate surface. Then, after the substrate cooling to room temperature, slowly peel off the substrate from the tape. **Figure 2.3 (a~f)** shows the image of the TMDC exfoliation process. There are several methods to determine the number of layers in TMDC materials, such as color contrast

in optical microscopy, Raman spectroscopy, Photoluminescence, and AFM thickness measurement. However, since the TMDC materials used in this study, such as $MoTe_2$, were multi-layered with thicknesses ranging from 10 to 20 nm, it is not necessary to determine their exact number of layers. Therefore, the details for layer determination are not discussed further here.

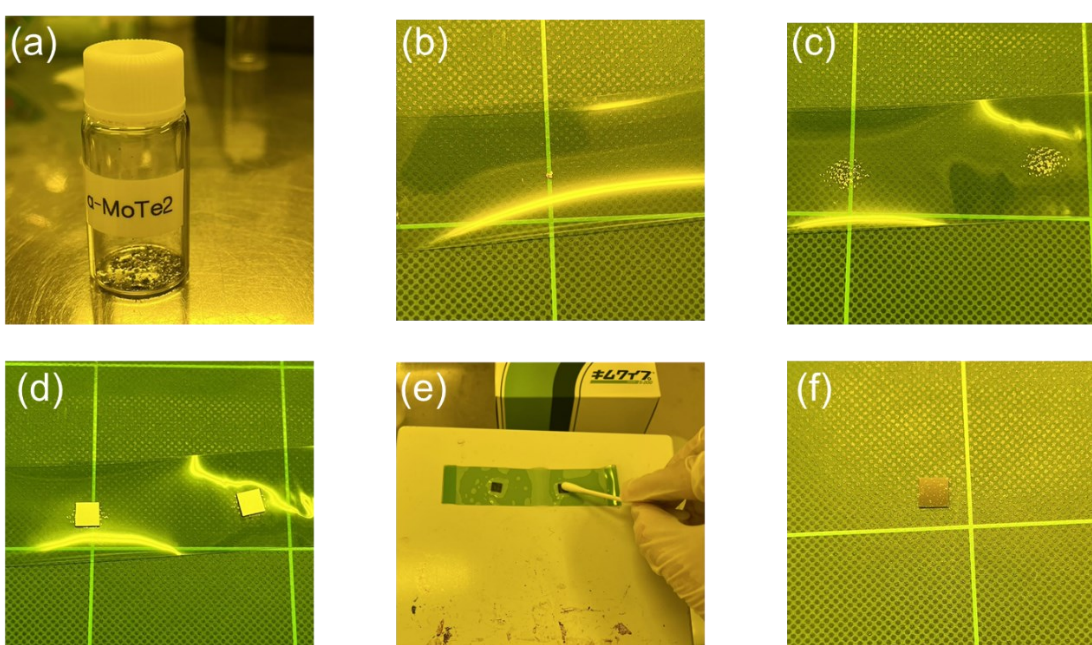

Fig. 2.3 Exfoliation process of TMDC materials.

2.2. Substrate cleaning

The substrates used in this study were Si substrates with 300 nm of thermally grown SiO_2. Depending on the device structure, two types of Si substrates were employed: heavily doped Si and undoped Si. The heavily doped Si was not only used as a substrate but also can directly serve as part of the device, functioning as the back gate, while the undoped Si just served as the substrate of the device. Substrate cleaning is crucial for device fabrication, as residual impurities can impact the properties of 2D materials. The cleaning process in this study is outlined below:

1. Cut a SiO_2 / Si wafer into a square of about 5 mm using a diamond cutter to obtain a substrate.
2. After roughly blowing off the dust on the prepared substrate with an air gun, soak

it in acetone and perform ultrasonic cleaning for 10 minutes.

3. Remove the substrate from the acetone solution, spray with isopropyl alcohol and bake on a hot plate at 90 °C for 1 minute.
4. Sock substrate in isopropyl alcohol and perform ultrasonic cleaning for 10 minutes.
5. If the cleaned substrate is intended for the exfoliation of 2D materials, it needs to undergo hydrophilic treatment. This treatment can be achieved through wet processes using Semicoclean solution (Soak the substrate in the Semicoclean solution and perform ultrasonic cleaning for 10 minutes) and dry processes using oxygen plasma etching (O_2: 40 sccm, vacuum degree: 3 Pa, Power: 20 W, frequency: 13.56 MHz, time: 30 sec). However, if the substrate is directly used for electrode deposition in device fabrication, this step is unnecessary.

2.3. Lithography

2.3.1. UV lithography

In this study, the electrode patterns were prepared by using UV lithography and electron beam lithography. Here is the UV lithography procedure:

The chemicals used were HMDS, LOR, and AZ5214E. The HMDS solution changes the substrate to hydrophobic and can make the photoresist uniformly. AZ5214E is used as the photoresist. The LOR functions as a sacrificial layer, and the development pattern can be reversed by using the LOR. The coating conditions for the photoresist and the process are shown below.

1. Fix the substrate in the center of the spin coater and drop the HMDS. Then, spin coat at 4000 rpm for 10 s.
2. Bake the substrate on a hot plate at 90 °C for 1 minute.
3. Fix the substrate in the center of the spin coater and drop the LOR. Then, the spin coat is continuously at 500 rpm for 3 s, 4500 rpm for 60 seconds, and 6000 rpm for 2 s.
4. Bake the substrate on a hot plate at 160 °C for 5 minutes.
5. Fix the substrate in the center of the spin coater and drop AZ5214E. Then, spin coat

at 5000 rpm for 25 s.

6. Bake the substrate on a hot plate at 90 °C for 1 minute.

Then, the sample is exposed to UV light using an exposure apparatus, transferring the pattern from the mask onto the substrate. The exposure time is 4.1 s. An AZ300MIF solution is used as the developer. After exposure, soak the substrate in AZ300MIF solution for 90 s, then rinse with ultrapure water for 1 minute, and bake on a hot plate at 90 °C for 1 minute.

2.3.2. Electron beam lithography

Electron beam lithography is one of the methods used to produce electrode patterns. It is performed using a scanning electron microscope (SEM) with a pattern generator. Compared with photolithography, a much finer pattern can be produced. The pattern can be created using computer-aided design (CAD) software, allowing for the creation of arbitrary patterns without requiring a photomask. Polymethylmethacrylate (PMMA) is used as the resistor. The coating conditions in electron beam lithography are shown below.

1. Fix the substrate in the center of the spin coater and drop the PMMA. Then, spin coat at 5000 rpm for 30 s.
2. Bake the substrate on a hot plate at 160 °C for 2 minutes.
3. Transfer the designed pattern onto the substrate using the SEM system.

The development conditions are as follows.

1. Soak the substrate in a solution of ultrapure water (30%) and IPA (70%) for 1 minute.
2. Rinse the substrate with ultrapure water for 1 minute.
3. Bake the substrate on a hot plate at 110 °C for 1 minute.

2.4. Metal deposition and lift-off

Since high temperatures in thermal evaporation can damage the 2D crystals, this study employs electron beam evaporation. This evaporation method utilizes accelerated electrons to bombard the metal target material, causing metal atoms to evaporate onto

the sample. It is characterized by low energy and stable deposition rate. After finishing the metal deposition, the lift-off process is required under the following conditions.

Use LOR and AZ5214E (for UV lithography):

Soke the sample in N-methyl-2-pyrrolidone solution at room temperature for over 1 hour. Then, spray with acetone and isopropyl alcohol and dry with a compressed air gun.

Use PMMA (for electron beam lithography):

Soak the sample in acetone solution at 60 °C for 30 minutes. Then, spray it with acetone and isopropyl alcohol and dry it with a compressed air gun.

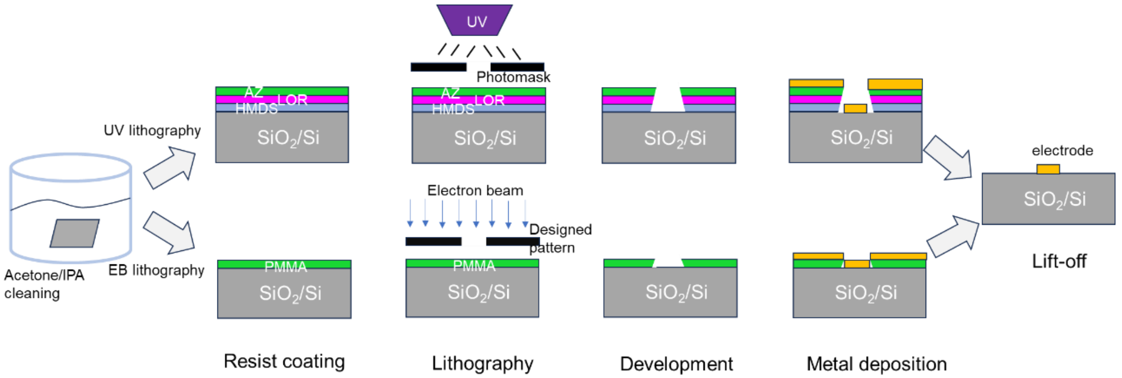

Fig. 2.4 Basic process of electric device fabrication.

2.5. Dry transfer

The transfer of 2D materials refers to the technique of relocating 2D materials from one substrate to a target substrate or other material by using some external methods. This process is a crucial step in the fabrication of 2D electronic devices, especially heterojunction devices. Currently, there are two main types of transfer methods: wet transfer and dry transfer. Wet transfer is typically suitable for large-area transfer where crystal positioning adjustment is not necessary, with PMMA commonly used as an auxiliary film for transfer [4]. Dry transfer, on the other hand, is suitable for transferring specific individual or multiple crystals while allowing for precise positioning adjustments, enabling the fabrication of heterojunctions. Thus, the transfer technique employed in this study is dry transfer. The auxiliary material for dry transfer is a

polycarbonate film with strong adhesion. The fabrication method of the polycarbonate film is shown in **Fig. 2.5 (a)~(c)**.

1. Dissolve Poly Bisphenol A Carbonat beads (Sigma-Aldrich) in chloroform solution at a 6-8% concentration.
2. Dripping an appropriate amount of polycarbonate solution onto a cleaned slide glass.
3. Use another clean glass substrate to press down the dropped polycarbonate solution, spreading it out and making it thin. The two glasses will plate together with the polycarbonate solution. Then, quickly separate the upper glass plate by pulling it away.
4. The uniformly spread polycarbonate solution left on the slide glass substrate will form a solid polycarbonate film after being allowed to stand at room temperature for 5 minutes to evaporate the solvent.

Since the polycarbonate film needs to be in full contact with the 2D crystal during the transfer process, it must be mounted on a transparent and soft stamp. PDMS gel park with a 1mm × 1mm size is commonly used as a stamp for the PC film. After preparing the polycarbonate film, slowly pick it up from the slide glass using tweezers and place it flat on the PDMS stamp. Then, heat it at 180 °C to ensure that the film adheres slightly to the surface of the PDMS stamp, as shown in **Fig. 2.5 (d)~(f)**. However, in this transfer method, the polycarbonate film attached to the PDMS surface tends to adhere extensively to the substrate, picking up unwanted crystals simultaneously, which significantly affects subsequent device fabrication processes and may cause the polycarbonate film to peel off from the PDMS stamp. Additionally, this method is prone to introducing bubbles at the interface of van der Waals heterostructures of 2D materials. These bubbles, containing organic substances, atmospheric moisture, and oxygen, negatively impact device characteristics. Moreover, due to the height of these bubbles ranging from a few nanometers to tens of nanometers, they cause uneven electric field application in the gate structure.

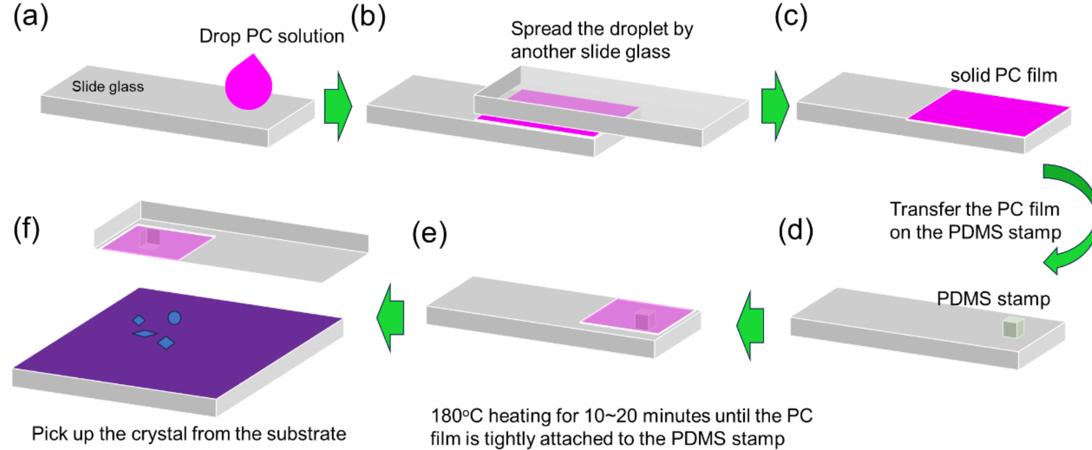

Fig. 2.5 Polycarbonate film-covered PDMS stamp Fabrication.

To avoid these issues, a PDMS stamp with a certain curvature, referred to as a PDMS lens as shown in **Fig. 2.6**, was used instead of a flat stamp. Employing a PDMS lens allows partial contact between the polycarbonate film and the substrate and facilitates the slow expulsion of air during the bonding of 2D materials, achieving a free-bubble heterojunction interface. The method for fabricating the PDMS lens is as follows:

1. Mix the base material (Sylgard 184) of the PDMS lens and curing agent in a plastic petri dish at a ratio of 10:1 and stir evenly.
2. Place the PDMS solution in a vacuum chamber and vacuum for 20 minutes to remove air bubbles.
3. Use a spatula needle to drop the PDMS solution onto a clean glass slide and bake on a hot plate at 130 °C for 5 minutes.
4. Use a tungsten probe with a tip diameter of only 1 μm to pick up a small amount of PDMS solution and drop it on top of the previously formed PDMS lens to create a second small PDMS lens. This process increases the curvature of the lens.
5. Bake at 130 °C for 5 minutes.

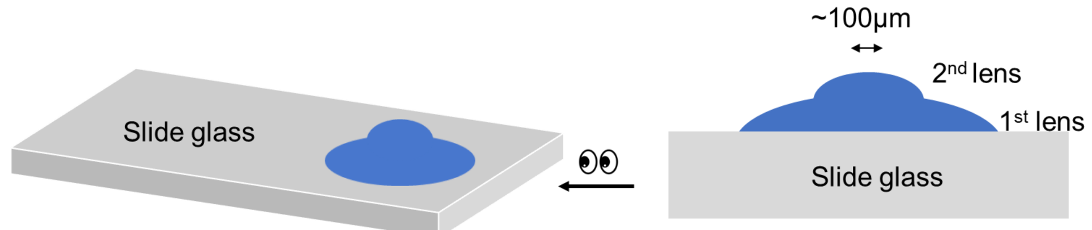

Fig. 2.6 Diagram of PDMS lens.

The transfer apparatus utilized in this study comprises a robotic arm offering xyz three degrees of freedom and a microscope system equipped with a stage with heating and rotation functions. The transfer procedure employing the PDMS lens of a 2D heterojunction is outlined as follows:

1. Fix the slide glass with the polycarbonate film/PDMS lens on the robotic arm, set the SiO_2/Si substrate with the target crystal "1" on the stage, and vacuum-adhere it for fixation. At this moment, set the stage temperature to 60 °C.
2. Under the microscope, align the center of the PDMS lens with target crystal "1" and gradually bring them closer using the control software of the robotic arm. Before contact, slightly offset target crystal "1" away from the center of the PDMS lens to prevent bubble entrapment during subsequent layer stacking.
3. Increase the stage temperature to 100 ~120 °C, allowing the PDMS lens to expand until the polycarbonate film fully adheres to target crystal "1".
4. Lower the stage temperature back to 60 °C, causing the PDMS lens to gradually contract. As the polycarbonate film is lifted, paste target crystal "1" until it completely detaches from the substrate.
5. Replace the substrate with target crystal "2" and align crystal "1" on the polycarbonate film with target crystal "2" on the substrate under the microscope. The alignment position depends on the specific structure of heterojunction.
6. Slowly bring the PDMS lens closer to the substrate. As crystal "1" approaches crystal "2", raise the stage temperature to 100 ~120 °C, utilizing the heating expansion of the PDMS lens to make them contact and adhere fully. Due to the curvature of the lens, compression occurs during contact, expelling air from the

contact interface.

7. Lowering the temperature to 60 °C causes PDMS to contract and pick up crystal "2" due to van der Waals forces with crystal "1".
8. Repeat steps 5-7 until the desired heterostructure is achieved.
9. Replace the substrate, which is either cleaned or pre-patterned with electrodes, on the stage. Slowly lower the completed heterostructure on the polycarbonate film to a specific position on the substrate, heat the stage to 180 °C, and wait for 2 minutes until the polycarbonate film adheres tightly to the substrate. Then, lift the PDMS lens via the robotic arm. At this point, the polycarbonate polymer will melt, and the heterostructure transfer from the PDMS lens to the substrate side.
10. Soak the substrate containing heterostructures in chloroform solution overnight to remove the polycarbonate polymer. Then soak it in IPA for several hours, followed by soaking it in fresh chloroform solution again for several hours, and rinse the substrate with IPA to reduce residual polycarbonate polymer.

Since polycarbonate polymer residuals can affect the properties of TMDC materials, *h*-BN is usually first picked up by polycarbonate film, and then TMDC materials are picked up by *h*-BN using van der Waals forces between *h*-BN and TMDC materials. **Figure 2.7** shows the 2D-heterojunction transfer process using the PDMS lens.

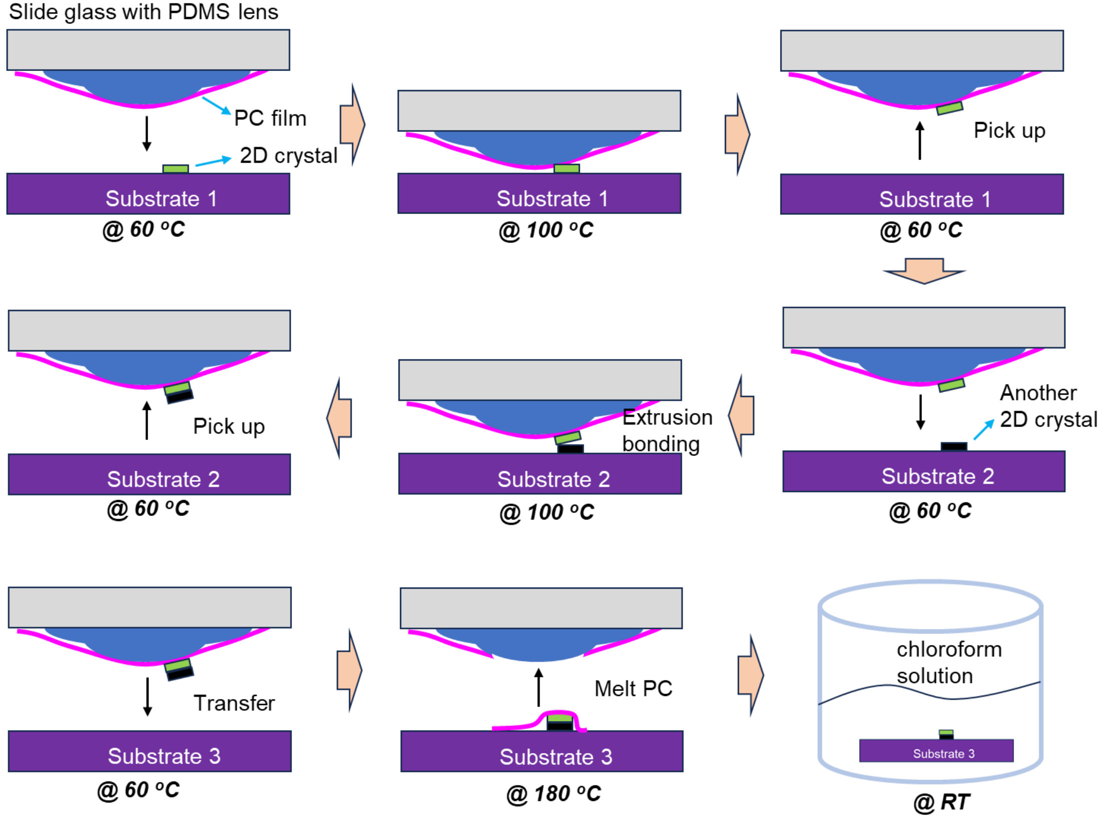

Fig. 2.7 Dry transfer process using PDMS lens with covered polycarbonate film.

2.6. Laser irradiation

Laser irradiation in this study was performed using a continuous wave laser with a wavelength of 532 nm and an output power of 1 W. The laser is guided into a chamber through an optical microscope, where samples can be placed, as shown in **Fig. 2.8**. The chamber is mounted on a stage that can move in the x and y directions and is connected to a vacuum pump, which can provide a high-vacuum environment (~10^{-4} Pa). Since the center of the laser spot remains fixed during each laser irradiation, the position displayed on the computer screen via the optical microscope is also fixed. The center of the laser spot is pre-marked on the computer screen; thus, when irradiating the crystal, it is only necessary to align the desired region on the crystal with the marked position through microscope observation. Linear scanning can be achieved by quickly moving the stage during irradiation. The laser irradiation time is determined by an automatically controlled shutter. Once the exposure time is set, the shutter opens automatically,

allowing the laser to be guided into the chamber for irradiation. After the set time elapses, the shutter automatically closes, blocking the laser from entering the optical microscope. The time for laser irradiation in this study was 1 or 2 seconds. Since a 20× objective lens was used to focus the laser, the laser spot was 4 μm in diameter on a sample surface. The power of the laser used to irradiate the 2H-$MoTe_2$ crystal in the chamber was in a range of 50~ 400 mW, which is controlled by a laser power variable attenuator.

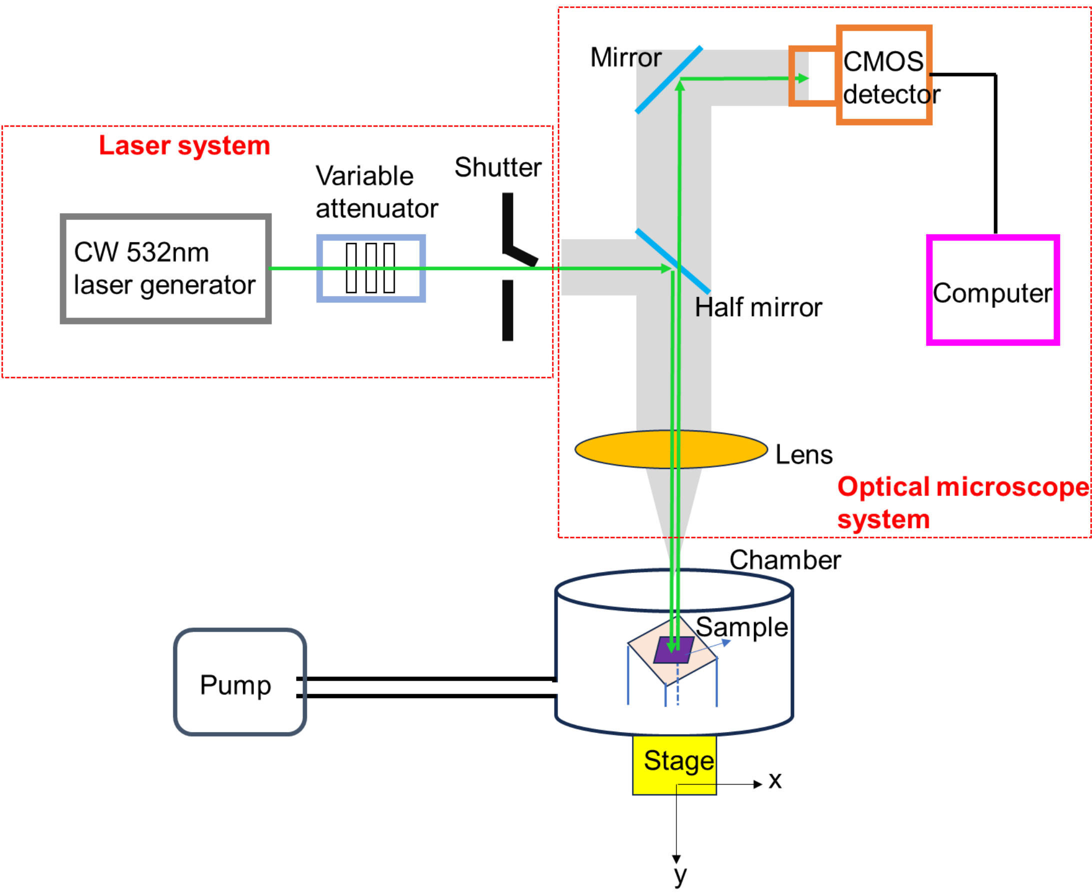

Fig. 2.8 Diagram of laser irradiation system.

2.7. Raman spectroscopy

Raman spectroscopy is an analytical technique that involves irradiating a sample with laser or other monochromatic light sources and then measuring the spectrum of the scattered light from the sample. It is based on the Raman scattering effect, where the vibration and rotation of excited molecules or crystal structures cause small changes in

the energy of photons, resulting in scattered light with frequencies different from the incident light. Raman spectroscopy is divided into two types: Stokes Raman scattering and anti-Stokes Raman scattering. Stokes Raman scattering occurs when the sample absorbs photon energy and emits it as lower-energy photons, whereas anti-Stokes Raman scattering emits higher-energy photons, as shown in **Fig. 2.9**. The frequencies of the scattered light in Raman spectra are typically shifted relative to the incident light. Stokes Raman scattering frequencies are lower than the incident light, whereas anti-Stokes Raman scattering frequencies are higher. This frequency shift is related to the molecular structure and vibrational characteristics of the sample, where different types of chemical bonds and molecular structures lead to specific Raman frequencies and intensities. In summary, Raman spectroscopy provides information about the chemical composition, crystal structure, morphology, and orientation of the sample. By comparing with known standards or databases, the compounds and substances present in the sample can be identified. In this study, Raman spectroscopy was primarily used to identify the crystalline phases of $MoTe_2$.

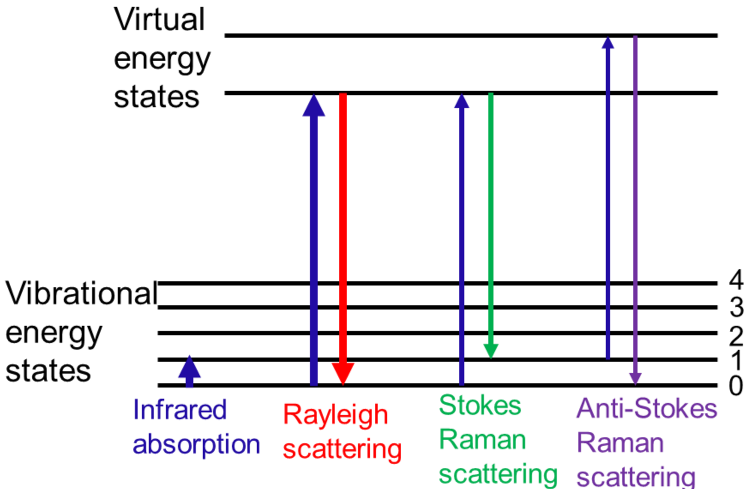

Fig. 2.9 Energy level diagram of Raman spectroscopy.

2.8. Electric measurement

2.8.1. Current-Voltage (*I-V*) characteristics

Current-Voltage (*I-V*) characteristics are important metrics for evaluating FET performance, encompassing I_d-V_g and I_d-V_d characteristics. The I_d-V_g characteristic is typically used to illustrate the influence of gate voltage on semiconductor channel current. From the I_d-V_g curve, the I_{on} and I_{off} values of the FET can be ascertained; thus, the on/off ratio can be obtained. Additionally, information such as the *SS* value and threshold voltage (V_{th}) can be derived from the I_d-V_g curve, reflecting the control ability of the gate over the whole channel. The I_d-V_d characteristic represents the influence of drain voltage on channel current under a certain gate voltage. At low drain voltages, the contact characteristics of FET can be revealed, where the current increases linearly with drain voltage, indicating ohmic contact, while non-linearity suggests Schottky contact. At high drain voltages, the saturation characteristics of FET can be observed, where current depends solely on gate voltage. In this study, all *I-V* characteristic measurements were conducted using a dual-channel Keithley 2613B source meter, providing both drain and gate voltages and measuring channel current and gate leakage current separately, as shown in **Fig. 2.10**. The measurement of *I-V* characteristics in TFET is similar to that of FET, with the only difference being the need to pay attention to the connection of the source and drain, as TFET operates on a reverse-biased p/n junction or a p/i/n junction.

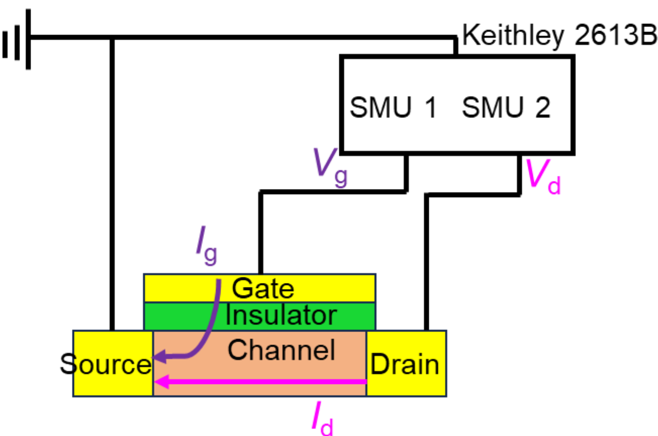

Fig. 2.10 Diagram of *I-V* characteristics measurement.

2.8.2. Inverter measurement

The transfer characteristics measurement of the inverter in this study is illustrated in **Fig. 2.11**. SMU1 of the Keithley 2613B source mater applies a sweeping input voltage to the gate of the inverter, while SMU2 is connected to the source of the p-channel FET and applies a drive voltage. The output voltage is measured in DC voltage mode by a digital multimeter (VOAC7602). For the AC response measurement of the inverter, a pulse voltage generator is connected to the gate of the inverter, applying pulse gate voltage as the input signal while simultaneously displaying the waveform on an oscilloscope. The oscilloscope is also connected to the drain of the inverter to read the output voltage waveform, as shown in **Fig. 2.12**.

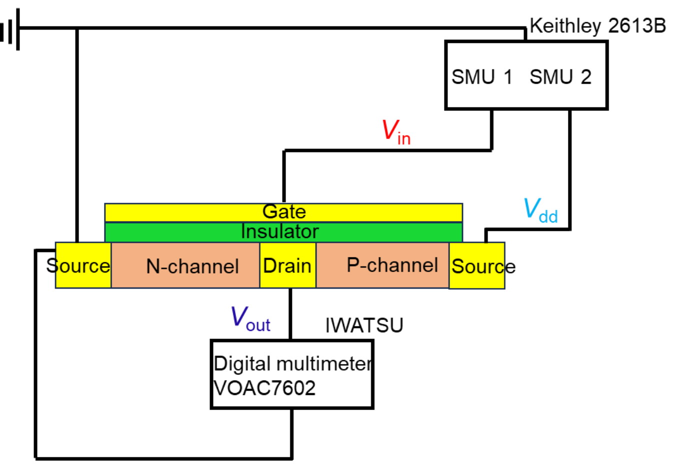

Fig. 2.11 Diagram of transfer characteristics measurement of inverter.

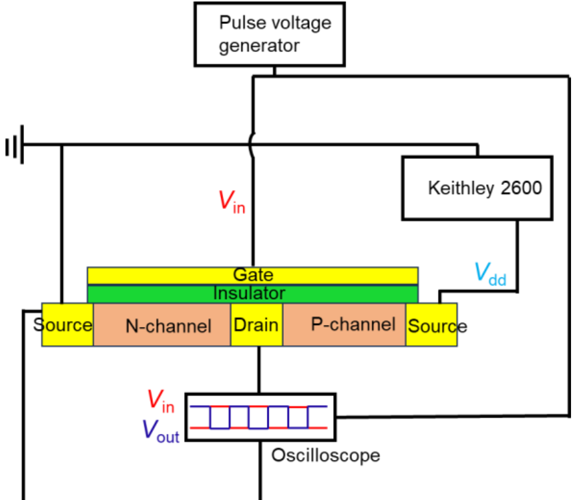

Fig. 2.12 Diagram of AC response measurement of the inverter.

Reference

[1] P. C. Shen, Y. Lin, H. Wang, et al. IEEE Transactions on Electron Devices **65**, 4040 (2018).
[2] X. Xu, T. Guo, H. Kim, et al. Advanced Materials **34**, 2108258 (2022).
[3] S. Vishwanath, A. Sundar, X. Liu, et al. Journal of Crystal Growth **482**, 61 (2018).
[4] S. Kim, S. Shin, T. Kim, et al. Carbon **98**, 352 (2016).

3. Laser irradiation effect on $MoTe_2$

Laser irradiation on 2D crystals constitutes instantaneous thermal annealing followed by rapid cooling, resulting in a sudden increase and decrease in crystal temperature. This chapter presents experimental results and analysis of the effects produced by high-intensity laser irradiation under different conditions on different regions of $MoTe_2$ crystal, including directly irradiated area and its adjacent regions, as shown in **Fig. 3.1**. Furthermore, in conjunction with the discussion of relevant previous studies, the effects of laser irradiation on $MoTe_2$ crystal under different conditions were summarized.

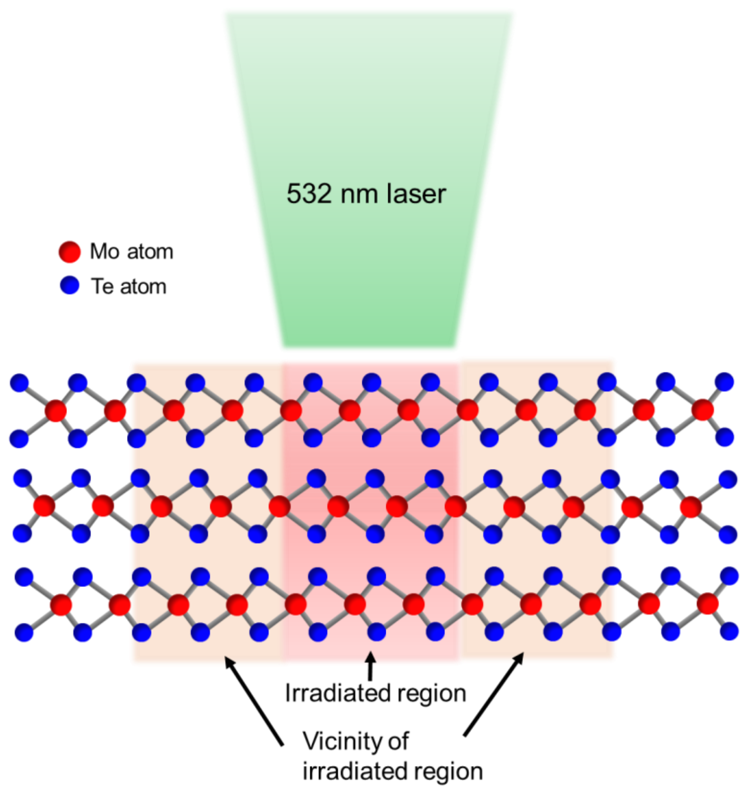

Fig. 3.1 Diagram of laser irradiation for $MoTe_2$.

3.1. Laser-induced phase transition

3.1.1. Effect on atmosphere condition

As stated in the “introduction” part, a study has reported that high-intensity laser irradiation of multilayer 2H-$MoTe_2$ crystal in the atmosphere can lead to phase transition with a layer-thinning phenomenon. After irradiation, the Raman spectrum of the crystal exhibits new peaks that are not characteristic of the 2H phase. Additionally, the irradiated crystals demonstrate high electrical conductivity, indicating a transition to the 1T' phase [1]. However, the other study has proposed that the peaks around 120 and 140 cm^{-1} do not correspond to the 1T' phase. In addition, the Raman spectrum of Te is conducted, revealing a strong resemblance between the irradiated crystal and Te. Consequently, it is suggested that high-intensity laser irradiation in the atmosphere does not induce a phase transition but rather the thermal decomposition of Mo and Te atoms [2]. This study first utilized Raman spectroscopy to elucidate the material formed after the 2H-$MoTe_2$ was subjected to high-density laser irradiation in the atmosphere. The Raman spectra of the exfoliated 2H- and 1T'-$MoTe_2$ were first measured, as shown in **Fig. 3.2 (a)**. The original 2H-$MoTe_2$ exhibits two distinct peaks located at 170 and 230 cm^{-1} of A_{1g} and E_{2g} mode, respectively. The original 1T'-$MoTe_2$ shows four prominent Raman peaks at 73, 110, 125, and 160 cm^{-1}, respectively. After high-intensity laser irradiation of 2H-$MoTe_2$, the Raman peaks belonging to the 2H phase disappeared, and numerous different Raman peaks emerged, as shown in **Fig. 3.2 (b) and (c)**. The upper part of **Fig. 3.2 (b)** is the Raman spectrum of Te powder extracted from the Ref [3]. Upon comparison, it is found that the two peaks observed in the irradiated crystal correspond to the Raman peaks of Te. The overlapping of the two peaks indicates that the irradiated crystal is not pure Te. The lower part of **Fig. 3.2 (c)** shows the Raman spectrum of the irradiated crystal in the wavenumber range of 200 ~ 1000 cm^{-1}, while the upper part shows the Raman spectra of MoO_2 grown on Si substrates at different temperatures extracted from the Ref [4]. Comparison reveals that all Raman peaks belonging to MoO_2 appear in the irradiated $MoTe_2$ crystal, indicating that the irradiated crystal contains MoO_2. Both Te and MoO_2 substances exhibit good electrical

conductivity, explaining the metallic electrical properties of the irradiated crystal. Furthermore, as stated in Ref [2], the ratio of Mo to Te elements was found to be close to 1:1 by EDX elemental analysis. This result confirms that the irradiated crystal is not 1T'-$MoTe_2$ and suggests that some Te atoms sublimate due to the heating. Combining the experimental results of this study, it can be inferred that after high-intensity laser irradiation of 2H-$MoTe_2$ in the atmosphere, the sudden increase in crystal temperature triggers the rupture of chemical bonds between Mo and Te atoms, resulting in the rapid oxidation of Mo atoms and the subsequent formation of MoO_2 and Te atoms. Additionally, some Te atoms sublime due to the high temperature. The overall process can be described by the following reaction equations. The Mo oxide is MoO_2 rather than MoO_3 because even if MoO_3 is produced, it will be reduced to MoO_2 by Mo atoms at high temperatures. **Figure 3.3** shows the Raman spectra of two crystal phases of MoO_3. In the Raman spectrum in this experiment, there were no Raman peaks consistent with MoO_3. Therefore, the Mo oxide after laser irradiation in the atmosphere are only MoO_2.

$$2\mathrm{MoTe_2} + 3\mathrm{O_2} \xrightarrow{\text{High T}} 2\mathrm{MoO_3} + 2\mathrm{Te} + 2\mathrm{Te}\ (\text{ sublimated}) \tag{3.1}$$

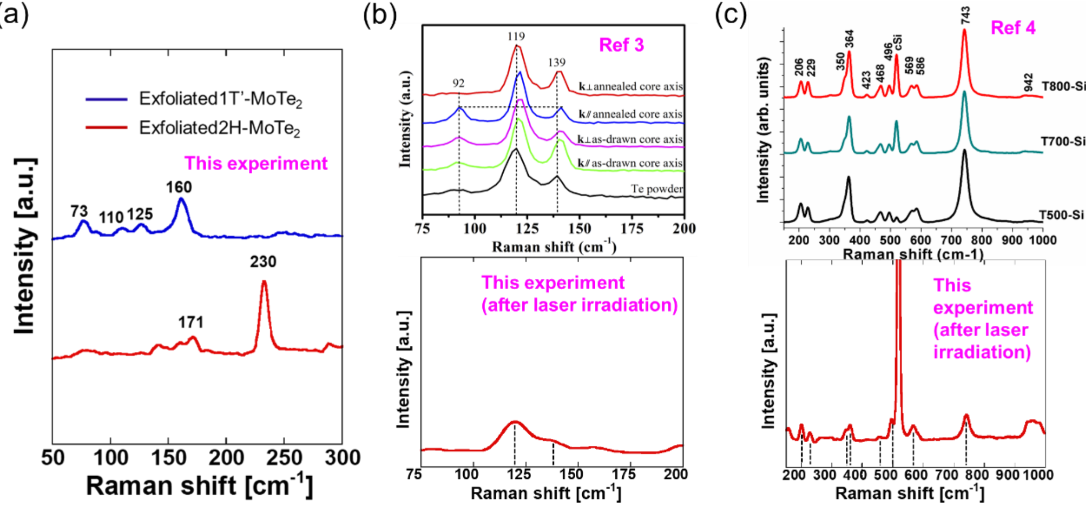

Fig. 3.2 (a) Raman spectra of exfoliated 2H-$MoTe_2$ and 1T'-$MoTe_2$. (b) Raman spectra in a wavenumber range of 75~200 cm^{-1} of Te powder [3] and laser-irradiated 2H-$MoTe_2$. (c) Raman spectra in a 200 ~ 1000 cm^{-1} range of MoO_2 [4] and laser-irradiated 2H-$MoTe_2$.

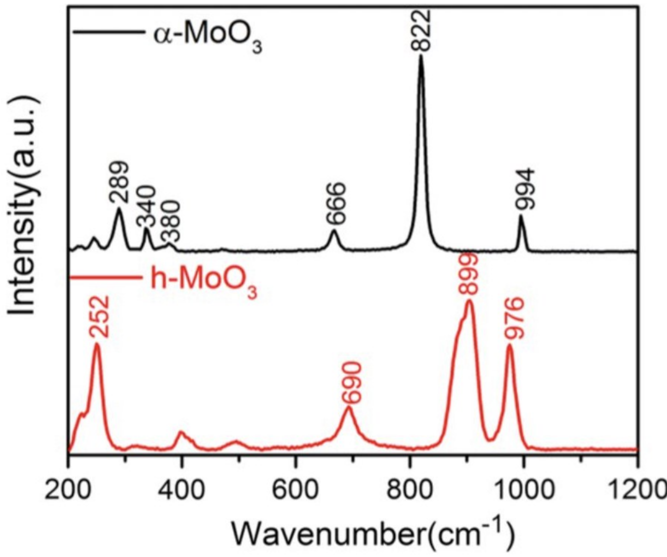

Fig. 3.3 Raman spectra of two crystal phases of MoO_3.

3.1.2. Effect on vacuum condition for 2H-$MoTe_2$

The presence of oxygen molecules significantly impacts the crystalline changes after laser irradiation, as their chemical reaction with Mo atoms hinders the occurrence of phase transitions. Therefore, in this study, high-intensity laser irradiation was performed on 2H-$MoTe_2$ crystals in a vacuum condition. In order to simultaneously investigate the effect of laser irradiation on their electrical properties, a 2H-$MoTe_2$ FET was fabricated, as shown in **Fig. 3.4 (a)**. It was placed in a vacuum chamber at a pressure of 10^{-6} Torr, and the channel region of the FET was irradiated by a focused laser several times with different intensities. Before the laser irradiation, the $MoTe_2$-FET showed ambipolar transfer characteristics, in which the p-branch is slightly stronger than the n-branch. After the irradiation with a power density of 0.25 MW/cm^2, the I_{on} of both the n-branch and p-branch reduced by about a half while the I_{off} increased, resulting in a degraded on/off ratio and the charge neutral point (CNP) shifted to a more positive value meanwhile. As is well-known, chalcogen-atom vacancies such as S, Se, and Te in TMDC materials typically act as electron dopants. Due to the relatively poor stability of Te atoms in $MoTe_2$, low-intensity laser irradiation can induce Te vacancies in $MoTe_2$ crystals. These vacancies can form donor levels in the band gap, leading to an n-doping effect of the crystal. However, the vacancies in TMDC materials also result

in a decrease in mobility. The reduction in mobility results in a decrease in current, while the doping effect enhances current; however, the doping concentration at this step is insufficient to compensate for the reduction of current caused by the decreased mobility. Consequently, the I_{on} decreased. The increase in I_{off} and the CNP shift is attributed to the doping effect. After a more powerful laser of 0.5 MW/cm^2 was irradiated to the channel, the I_{on} in both branches was back to the original value; however, the on/off ratio was drastically reduced because of the substantially increased I_{off}. A more powerful laser induces a higher number of Te vacancies, and the doping concentration is increased, thereby compensating for the current loss resulting from reduced mobility. At this moment, the color of the 2H-$MoTe_2$ did not change, indicating that no layer-thinning phenomenon occurred in the irradiated region. When the laser power was increased to 1 MW/cm^2, the color of the irradiated crystal was changed distinctly. The current in the FET at this moment is almost independent of the gate voltage. Due to the spot size of the laser being just half of the channel area, it is not enough to change the whole channel region. After irradiating the other half of the channel with the same power laser, the current level became larger. **Figure 3.4 (b)** shows the final image of the sample. The color of the entire channel was changed, corresponding to a phenomenon of layer-thinning. This laser-irradiated crystal has a higher conductivity and no longer obvious semiconducting properties. **Figure 3.5** shows the change of I_d-V_g curves after each irradiation.

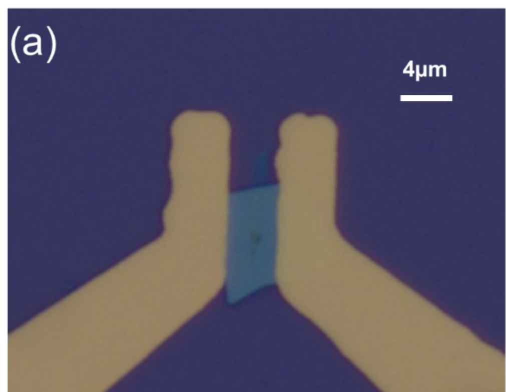

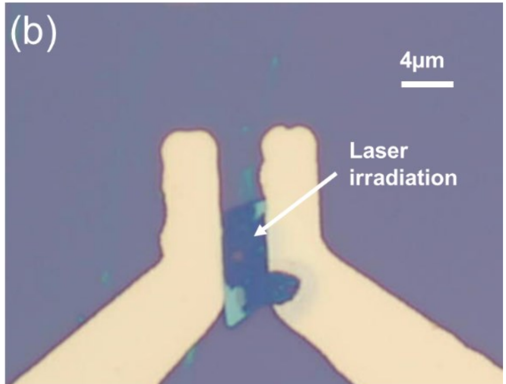

Fig. 3.4 Optical image of the $MoTe_2$-FET before (a) and after (b) laser irradiation in a vacuum environment.

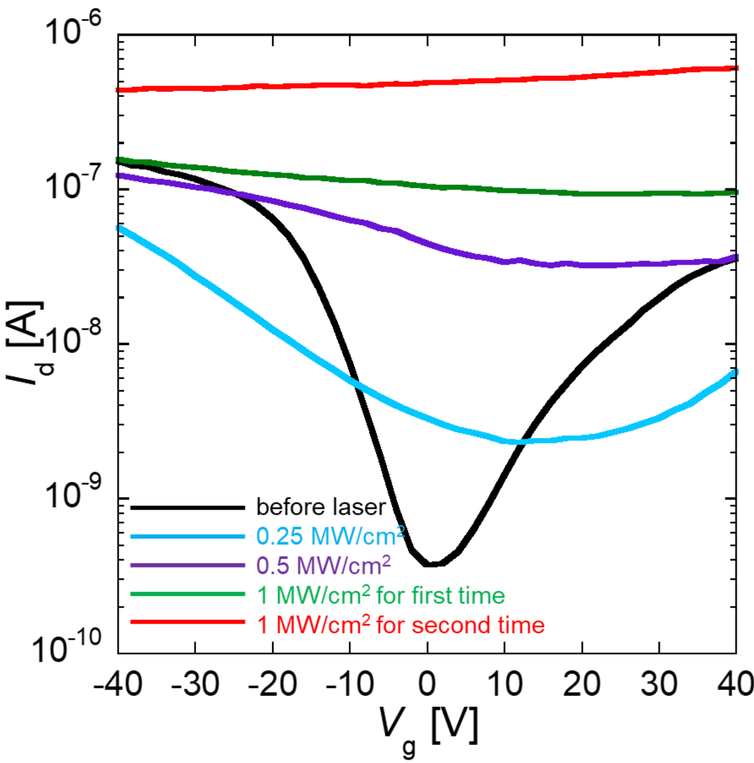

Fig. 3.5 I_d-V_g curves after each laser irradiation with different densities.

To confirm the phase of the channel region after the high-density laser irradiation in a vacuum condition, the crystal of the channel in $MoTe_2$-FET was confirmed by Raman spectroscopy in the atmosphere before and after the laser irradiation. As shown in **Fig. 3.6**, the peaks of the pristine crystal at 171 cm^{-1} and 231 cm^{-1} are assigned as the A_{1g} and the E_{2g} modes, respectively, corresponding to the 2H phase. After the high-density laser irradiation, the Raman spectrum changed and has two new significant peaks located at 152 cm^{-1} and 240 cm^{-1}, slightly broader than the pristine 2H phase peaks. Through comparative analysis via Raman spectra, it is found that these two distinctive peaks do not belong to the 1T' phase nor the Te. However, it is worth noting that $MoTe_2$ exists in three crystalline phases; aside from the 2H and 1T' phases, there is also a semi-metallic phase known as 1T, which was introduced before. These three distinct crystalline phases were successfully grown using the CVD method, followed by characterization using Raman spectroscopy and electrical measurements, which were reported in Ref [5]. By comparing the results with those in Ref [5], it is observed that

the crystalline phase following high-intensity laser irradiation under vacuum conditions corresponds to the 1T phase, as depicted in **Fig. 3.7**. The inset figure shows the Raman spectra of CVD-growth 1T-$MoTe_2$ extracted from the Ref [5]. The green line in the inset figure represents the simulated Raman peak by DFT calculation, which closely matches the experimental measurements.

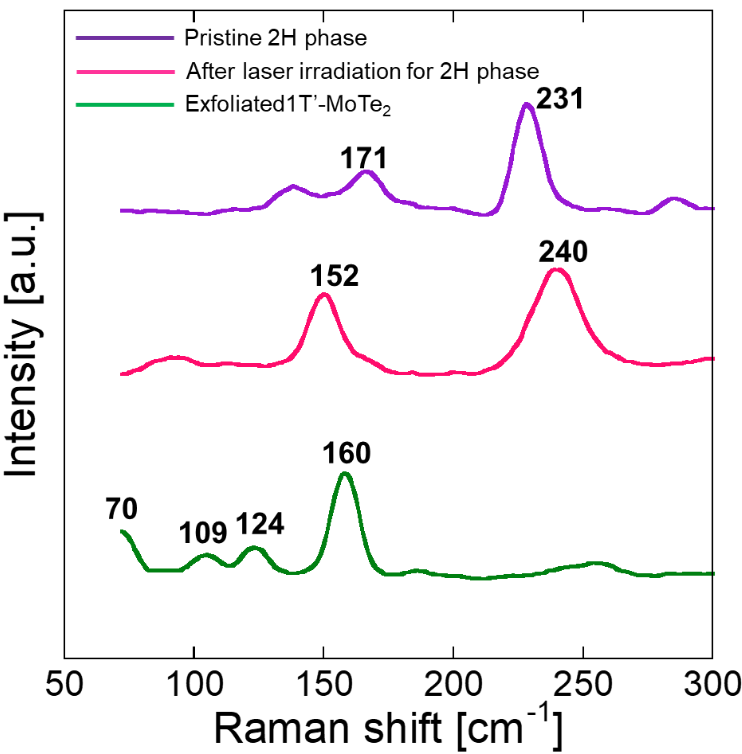

Fig. 3.6 Raman spectra of 2H-$MoTe_2$ before (purple) and after (pink) laser irradiation and exfoliated 1T'-$MoTe_2$ (green).

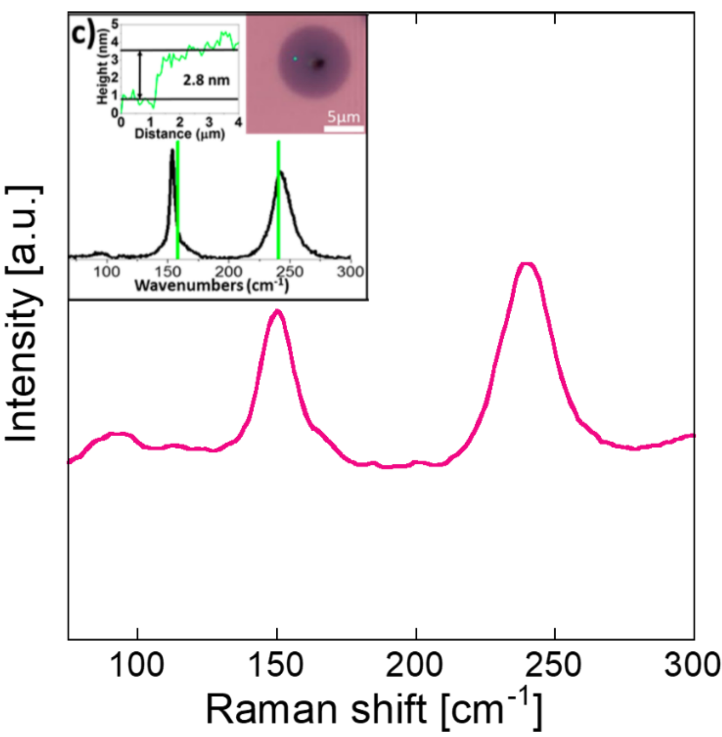

Fig. 3.7 Raman spectrum of the crystal after laser irradiation in a vacuum environment. The inset figure shows the Raman spectrum of CVD-growth 1T-$MoTe_2$, and the green line in the inset figure represents the simulated Raman peak by DFT calculation.

Although the current of the FET sample exhibited nearly gate-independent characteristics after being fully irradiated by a high-density laser for the channel, the crystal underneath the electrodes retained their original 2H structure as they are not directly irradiated by the laser, impacting the electrical properties of the channel. To accurately measure the electrical characteristics of the crystal after laser irradiation in a vacuum condition, two electrodes were fabricated directly on the irradiated crystals, forming an FET with a laser-irradiated crystal as the channel, as shown in **Fig. 3.8 (a)**. **Figure 3.8 (b)** shows the I_d-V_g curve of the FET. At a drain voltage of 0.1 V, the current exceeds 20 microamps, corresponding to a total resistance of 5 kilohms, including both channel and contact resistances. The resistance measured for the 1T phase in Ref [5] is in the range of hundreds of ohms. The relatively large total resistance observed in this experiment is attributed to the high contact resistance at the kilohm level in the two-terminal measurements. Moreover, the current remains constant regardless of gate voltage. Such electrical behavior is consistent with the properties of a 2D semimetal.

Combined with the Raman spectra, it can be inferred that the crystal formed by high-intensity laser irradiation in a vacuum condition is of the 1T phase, indicating a phase transition from 2H to 1T structure. Numerous 2H-$MoTe_2$ crystal samples were measured, and the experimental results for each sample were found to remain highly consistent. Furthermore, this laser-induced 1T phase can stably exist in the atmosphere for a long time.

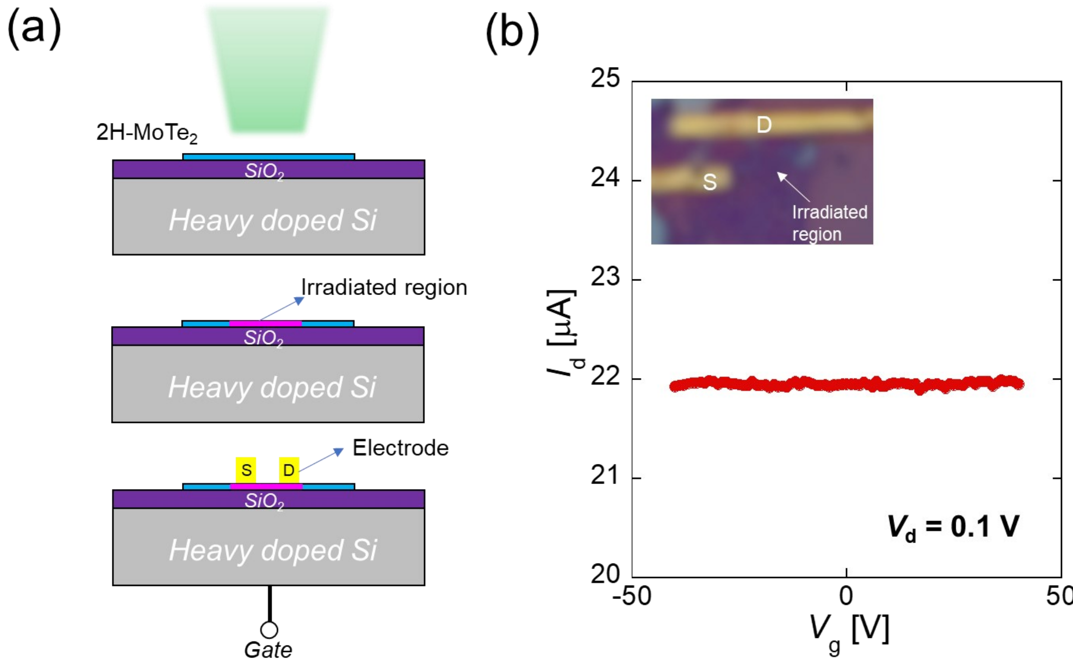

Fig. 3.8 Fabrication process (a) and I_d-V_g curve (b) of p^{++}-Si back-gated FET with the laser-irradiated region as channel.

3.1.3. Effect on vacuum condition for 1T'-$MoTe_2$

A theoretical study suggests that the metastable structures of $MoTe_2$ tend to preferentially select the 1T' phase [6]. However, the results of this experiment demonstrate that laser-induced phase transition tends towards the 1T phase rather than the 1T' phase. Therefore, the exfoliated CVD-growth 1T'-$MoTe_2$ was irradiated by a high-density laser in a vacuum. After irradiating, there was a noticeable change in color in the irradiated area of the crystal, indicating a layer-thinning phenomenon occurred as same as the irradiated 2H-$MoTe_2$, as shown in **Fig. 3.9 (a)**. The Raman spectra were

measured before and after laser irradiation, as shown in **Fig. 3.9 (b)**. Before the laser irradiation, the 1T'-$MoTe_2$ crystal showed four peaks at 75,109,126 and 159 cm^{-1}, respectively, which is almost consistent with our previous results. It should be noted that even with the same sample, Raman measurements conducted a second time may exhibit a little difference from the first measurement, typically with errors of 1~3 cm^{-1} in wavenumber. These errors are generally attributed to the Raman apparatus and can be disregarded. After laser irradiation, the Raman spectrum of the irradiated region showed a strong attenuation of these peaks located at 72,107 and 124 cm^{-1}, and the peak located at 160 cm^{-1} had been a slight shift to 155 cm^{-1}, which close to the characteristic peak of 1T phase. Furthermore, a new peak appeared at 240 cm^{-1}, which is another characteristic peak belonging to the 1T phase. In addition, the widths of these two peaks are also broad, similar to the experimental results of laser irradiation on 2H-$MoTe_2$ stated before. Thus, the 1T phase was also induced by laser irradiation in a vacuum condition for 1T'-$MoTe_2$.

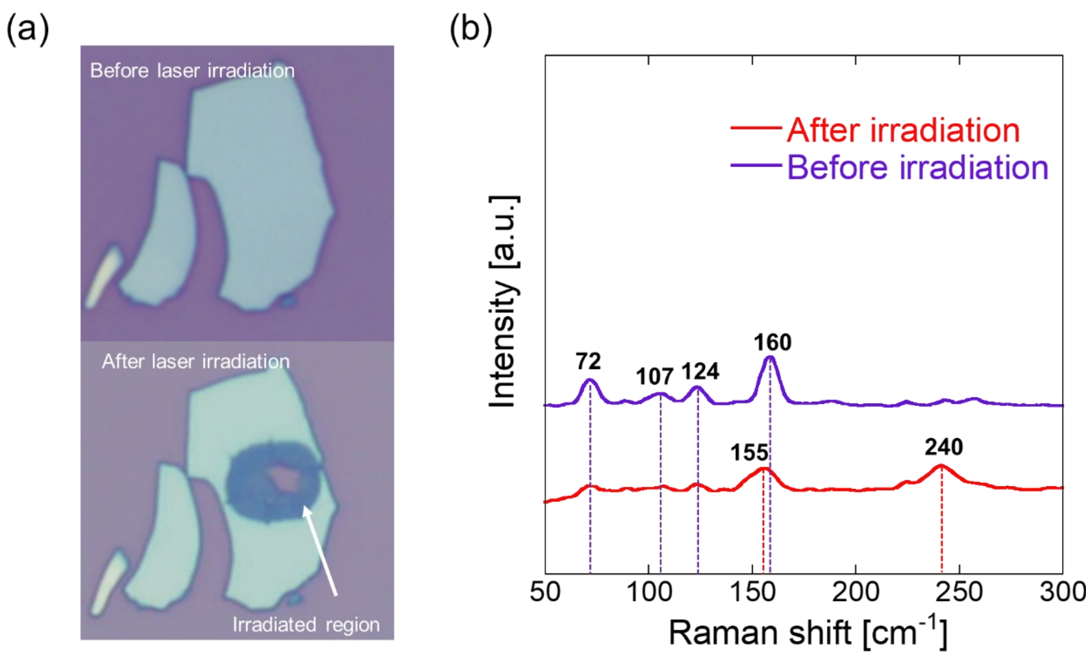

Fig. 3.9 Optical image (a) and Raman spectra (b) of 1T'-$MoTe_2$ before and after laser irradiation.

3.1.4. Temperature change in phase transition

Laser irradiation causes a rapid increase in the temperature of the crystal; however, the temperature change within the crystal is difficult to measure directly. **Figure 3.10 (a)** shows the Raman spectrum of *h*-BN; it has a strong Raman peak of in-plane mode located nearly 1560 cm^{-1} [7]. Since the position of the in-plane mode peak of *h*-BN linearly depends on temperature, as shown in **Fig. 3.10 (b)**, the temperature of $MoTe_2$ crystal stacked under an *h*-BN freak can be determined by measuring the in-plane mode peak shift of *h*-BN when subjecting laser irradiation to the stack. Due to the relatively large bandgap width of *h*-BN, it does not absorb the 532 nm laser. Therefore, the energy of the laser is almost entirely absorbed by the $MoTe_2$ underneath the *h*-BN. Consequently, the temperature increase induced by the laser irradiation will be transferred to the *h*-BN, resulting in a shift of the E_{2g} peak of *h*-BN. Due to the Raman apparatus in this experiment utilizing a laser intensity rated at 65 mW, the laser intensity is adjusted using neutral density filters with different attenuation ratios of 1%, 10%, and 25%, corresponding to intensities of 5.6, 14, and 22.4 mW, respectively. The objective lens used in measuring the Raman spectrum of *h*-BN was 100× to obtain a clear Raman peak under a smaller laser intensity. It should be noted that when we performed the phase transition experiment of $MoTe_2$, the objective lens and the laser intensity were 20× and 120 mW, respectively. In order to achieve the same power density by using an objective lens of 100×, the power should be 30 mW because the laser spot size in 100 ×, was a quarter of 20× lens. Therefore, using "30" as the x value of the extracted relational expression ($y = 1367.5 - 0.41667x$), the wavenumber change amount was 12.5 cm^{-1}, as shown in **Fig. 3.11**. Knowing that the relationship between the wavenumber of the E_{2g} peak of *h*-BN and the temperature dependency is 0.023 $cm^{-1}/ {}^{o}C$, it can be calculated that the temperature change at which the phase transition of $MoTe_2$ occurs is about 540 °C in a vacuum condition. Since heat is transferred from $MoTe_2$ to *h*-BN, energy loss inevitably occurs during this process. Therefore, the actual temperature increase in the phase transition process is larger than the value of 540 °C calculated using this method.

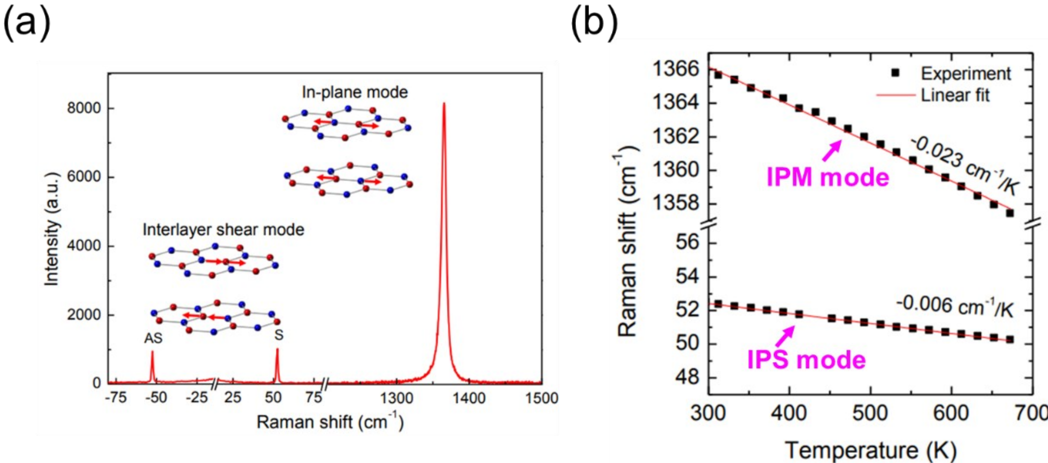

Fig. 3.10 (a) Raman spectrum of bulk *h*-BN. (b) Raman peak position of the ISM and the IPM mode as a function of temperature. [7]

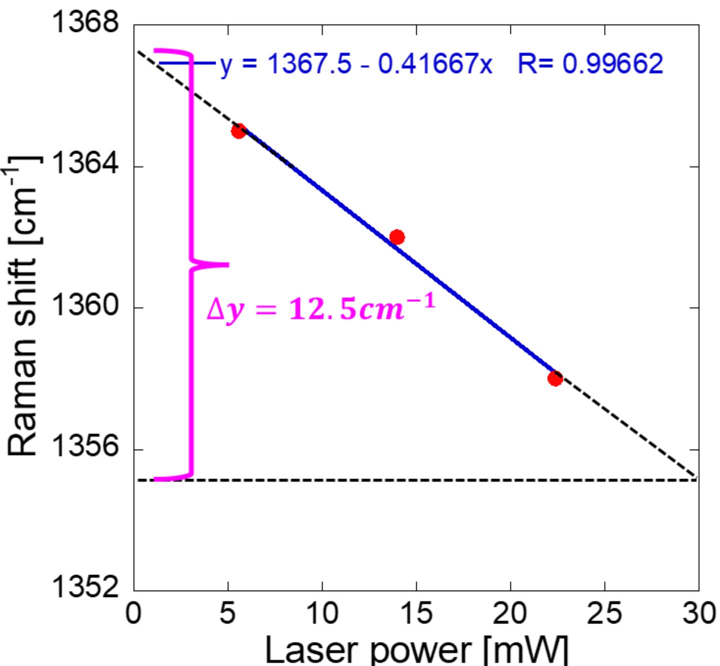

Fig. 3.11 (a) Linear relationship between the Raman shift of the in-plane mode peak of *h*-BN and laser power.

3.1.5. Mechanism of phase transition

In Ref [5], the 1T phase of $MoTe_2$ was obtained by precursor reaction at high temperature followed by quenching at 450 °C, while quenching at 350 °C resulted in the crystallization of the 1T' phase and quenching below 100 °C resulted in the 2H phase. This indicates that the crystal structure of the 1T phase is more stable at high temperatures. **Figure 3.12** shows the free energy of $MoTe_2$ in the 2H, 1T′, and 1T phases based on calculations of the phonon density of states in the three phases. At low temperatures, the energy of the 2H phase is the lowest, making it a stable structure. However, after reaching a temperature of 310 °C, the energy of the 1T' phase becomes the lowest, making the 1T' phase the stable structure. This transition temperature is close to the experimental growth temperature of 350 °C. For the 1T phase, the energy of the structure becomes the lowest after reaching a temperature of 916 °C. However, the growth temperature of the 1T phase is 450 °C. The significant discrepancy between theoretical calculations and experimental results is attributed to some factors influencing phase stability that are not fully considered in the computational model. In reality, the stability of materials is influenced by various factors, such as interactions with gaseous substances and substrates. Therefore, theoretical calculations may overestimate the stability temperature of the 1T phase. However, this indicates that the 1T phase has the minimum free energy at sufficiently high temperatures, replacing the 1T' phase as the stable structure. The stability of the 1T phase of $MoTe_2$ at high temperatures may be related to its structural characteristics and atomic interactions. At high temperatures, thermal vibrations of atoms and molecules increase, leading to temporary bond breakage or structural changes. However, theoretical calculations have shown that, for the 1T phase of $MoTe_2$, although some Mo-Mo bonds may experience temporary breakage at high temperatures up to 500 K, the overall atomic structure remains stable. This suggests that the 1T phase exhibits high thermal stability. Laser irradiation is somewhat analogous to quenching, as it can induce rapid heating and cooling of the material. When a laser is directed onto the material surface, it rapidly absorbs energy, causing a sharp increase in local temperature. Subsequently, when the laser is stopped or removed, the material undergoes rapid cooling. This rapid thermal

change can lead to structural changes in the material, similar to the effects observed during the quenching process. The estimated increase in crystal temperature induced by high-intensity laser irradiation in this experiment exceeds 540 ºC, which is higher than the growth temperature for the 1T phase, indicating that $MoTe_2$ is more stable in the 1T phase structure at this temperature, prompting the phase transition from 2H to 1T. The phenomenon of layer thinning observed after laser irradiation occurs because the energy of the laser is transferred from the crystal's surface to its interior. The high temperature at the surface disrupts the crystal structure, causing atoms to be heated and sublimate, resulting in a reduction in the number of layers. However, when subjected to the same laser intensity in the atmosphere, 2H-$MoTe_2$ undergoes a similar rapid increase in temperature, rendering the 2H phase unstable. However, unlike in a vacuum condition, oxygen molecules will oxidize the Mo atoms at high temperatures, thereby impeding the occurrence of phase transitions. Therefore, the residue formed after high-intensity laser irradiation of 2H-$MoTe_2$ in the atmosphere is a mixed layer of Mo oxide (MoO_2) and Te atoms.

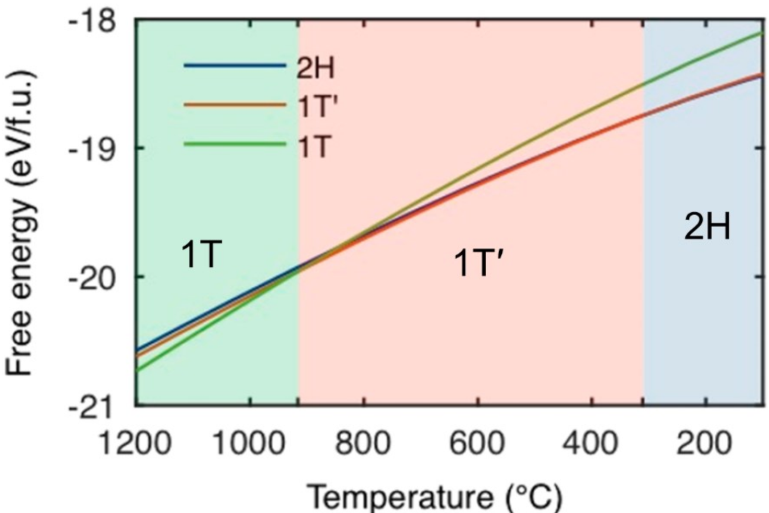

Fig. 3.12 Computed phase stability. Free energy of $MoTe_2$ in the 2H, 1T′, and 1T phases based on calculations of the phonon density of states in the three phases [5].

3.2. Laser-induced doping

High-density laser irradiation sometimes causes the crystal to sublime and disappear, leaving behind a hole in the irradiated area. This situation is prone to occur in a vacuum environment where a vacuum pump continuously pumps out the gas inside the chamber. It is also related to the thickness of the $MoTe_2$ crystal and the type of substrate. Thicker crystals have higher light absorption rates, making them more prone to sublimation. Additionally, when *h*-BN is used as the substrate for $MoTe_2$ instead of SiO_2, a higher laser intensity is required to induce changes in the crystal because the heat caused by the laser is easy to diffuse through *h*-BN. Regarding the irradiation time, since the time precision of the shutter is in seconds, the duration of irradiation in seconds does not significantly affect the irradiation results. In addition to the change in the directly irradiated area, the vicinity of the irradiated area is also affected by laser irradiation, as shown in **Fig. 3.13**. This section will discuss the effect of laser irradiation on this region.

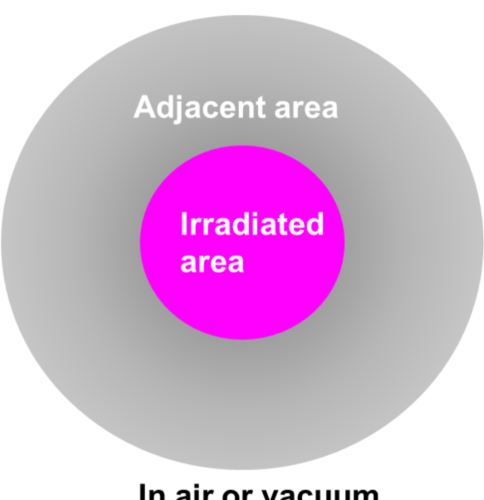

Fig. 3.13 Schematic diagram of crystal situation after laser irradiation.

3.2.1. Heavy n-doping effect

Figure 3.14 (a) shows a top-contacted $MoTe_2$-FET sample after high-density laser irradiation between the electrodes in a vacuum. The laser created a hole in the channel at the irradiated region. The diameter of the hole is almost the same as the size of the laser spot. Raman spectroscopy was used to confirm the crystalline structure inside and near the irradiated area. No signal was observed in the irradiated area within the wavenumber range, indicating no residue remained after the irradiation. Before laser irradiation, the original sample showed two prominent peaks at 170 cm^{-1} and 230 cm^{-1}, which correspond to the A_{1g} mode and E_{2g} mode of 2H-$MoTe_2$, as shown in **Fig. 3.14 (b)**. After laser irradiation, no significant change was observed in the spectrum in the regions indicated by red-dotted rectangles close to the irradiated area. The color of the remaining $MoTe_2$ crystal did not change after the irradiation, as shown in **Fig. 3.14 (a)**, indicating that the adjacent crystal of the irradiated area does not exhibit a layer-thinning phenomenon or phase transition caused by the influence of the laser.

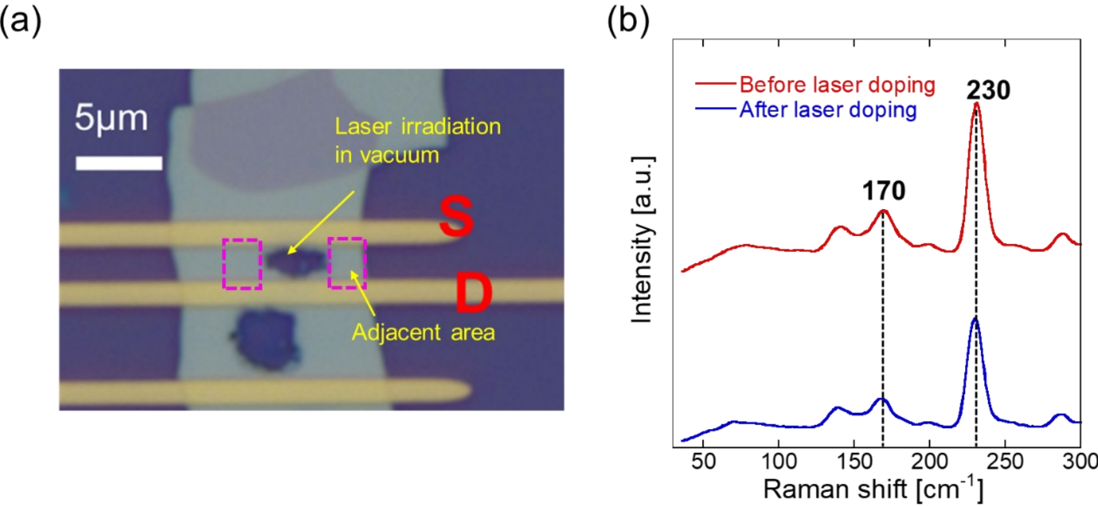

Fig. 3.14 (a) Optical image of the FET sample after high-density laser irradiation for the channel in a vacuum. (b) Raman spectra of the original crystal and the adjacent crystal of irradiated area.

Figure 3.15 (a) shows the I_d-V_g curves of the $MoTe_2$-FET sample before and after the laser irradiation at room temperature. The original sample showed an n-type semiconducting transfer property with an on/off ratio of 10^3 caused by the doping effect of polycarbonate residue during the transfer process. After laser irradiation in the channel, the transfer property changed to n^+-property with a high drain current (I_d), and the threshold voltage shifted to a significantly negative value. The current is almost independent of the gate voltage. **Figure 3.15 (b)** shows the I_d-V_g curves of the n^+-doped $MoTe_2$-FET sample at different temperatures. The current values in each curve decreased slightly with the temperature decrease; however, no significant change was observed in the shape of the curve. This result indicates that the channel region includes a gate-independent degenerately heavily doped region and a gate-dependent lightly doped one in parallel; however, even the heavily doped region has a small potential barrier at the contact region.

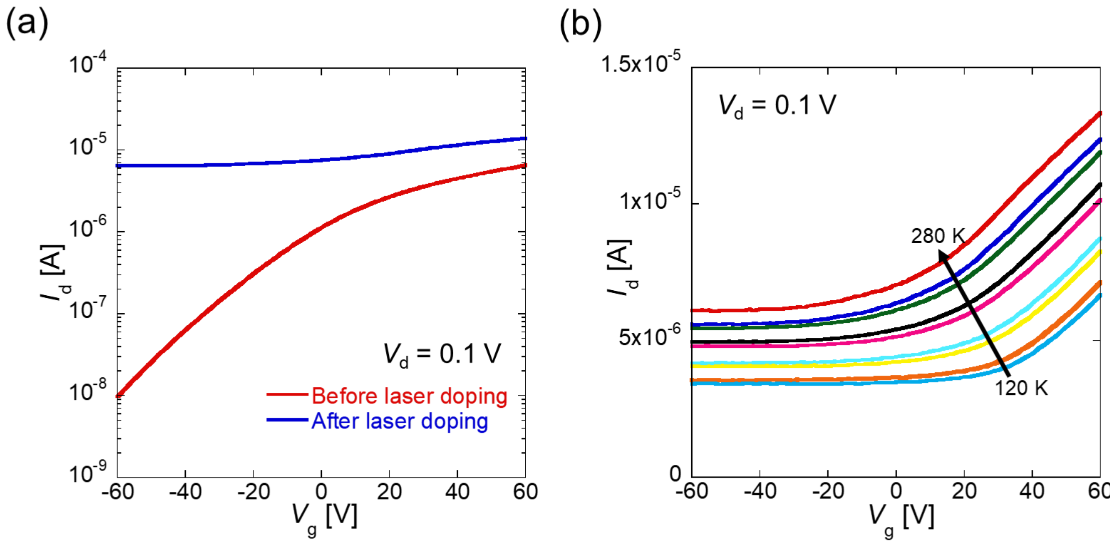

Fig. 3.15 (a) I_d-V_g curves of the $MoTe_2$-FET before and after laser doping at room temperature. (b) I_d-V_g curves of heavily n-doped $MoTe_2$-FET at different temperatures.

Generally, $MoTe_2$ crystals are easily damaged by heat because of the weak stability of Te atoms. Therefore, increasing the temperature above 120 ºC began to produce Te vacancies. Chalcogen-atom vacancies have an effect of n-type doping in TMDC crystals; thus, annealing at a high temperature in an oxygen-free environment for $MoTe_2$ can make the crystal n-doped [8]. In this study, after subjecting the $MoTe_2$ crystal to high-density laser irradiation, it absorbed the energy of the laser, causing a rapid increase in the crystal temperature. The temperature of the $MoTe_2$ crystal during the irradiation can be extremely high so that the crystal was decomposed into Mo and Te atoms and completely sublimated in a vacuum environment as schematically shown in **Fig. 3.16**; therefore, no Raman signal was observed in the irradiated area. However, due to the Gaussian profile of the laser, the temperature of $MoTe_2$ crystal around the irradiated area is also heated up, and then the sublimation of Te atoms creates Te vacancies. This situation is similar to high temperature annealing in a vacuum environment. The rapid thermal annealing induced by laser irradiation creates numerous Te vacancies near the irradiated area, establishing a heavily n-doped region. However, as the distance from the irradiated area increases, the doping level gradually diminishes. This decay occurs because the annealing temperature decreases with distance from the irradiation area. Additionally, even when the n-doped sample was placed in the atmosphere, no change in the doping level was observed, indicating that this laser-induced heavy n-type doping is stable. It should be noted that the temperature rise in the adjacent region caused by laser radiation is insufficient to promote a phase transition. The first-principal density functional theory (DFT) calculation reveals an appearance of donor level in the band gap when considering a Te vacancy in a 3×3 lattice, as shown in **Fig. 3.17,** which aligns with the experimental results.

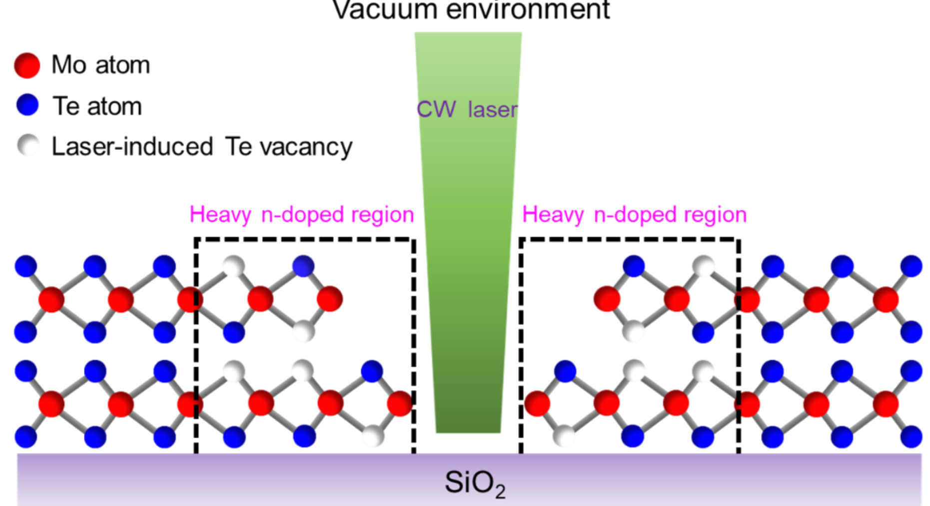

Fig. 3.16 Schematic diagram of heavy n-type doping via laser irradiation in a vacuum condition.

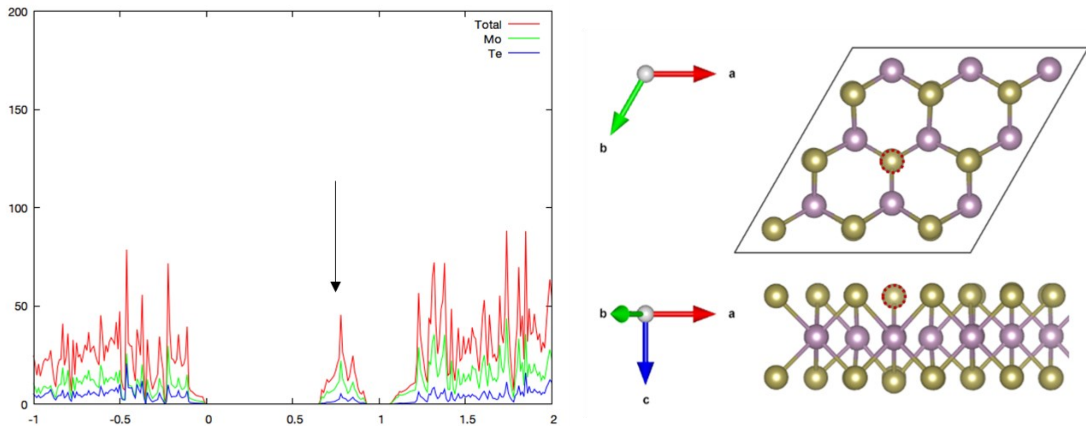

Fig. 3.17 DFT calculation of energy level in the band gap of $MoTe_2$ with Te vacancy in a 3X3 lattice.

3.2.2. Heavy p-doping effect

In order to confirm the effect of laser irradiation in the atmosphere, a bottom-contacted $MoTe_2$-FET sample was fabricated, and it was scanned linearly with a focused high-density laser by moving the sample stage. **Figure 3.18 (a)** shows the optical image of the $MoTe_2$-FET sample after laser irradiation. A groove was always created in the irradiated area in the case of scanning irradiation. The irradiated area showed an evident color change, which resulted in a layer-thinning phenomenon. Compared with the case of laser irradiation in a vacuum condition, there is often a crystal residue in the groove. The residue is a mixed layer of MoO_2 and Te, as stated before. However, the adjacent area we focused on showed no significant change in the Raman spectrum from the original one, corresponding to the 2H-$MoTe_2$, as shown in **Fig. 3.18 (b)**, indicating that no phase transition occurred in the adjacent area. **Figure 3.19 (a)** shows the I_d-V_g curves of the adjacent area before and after the laser irradiation at room temperature using the electrodes shown in **Fig. 3.18 (a)**. It changes from an n-type semiconducting transfer characteristic to a heavily p-doped one. This p^+-region showed good stability, even in a vacuum and low-temperature condition, as shown in **Fig. 3.19 (b)**.

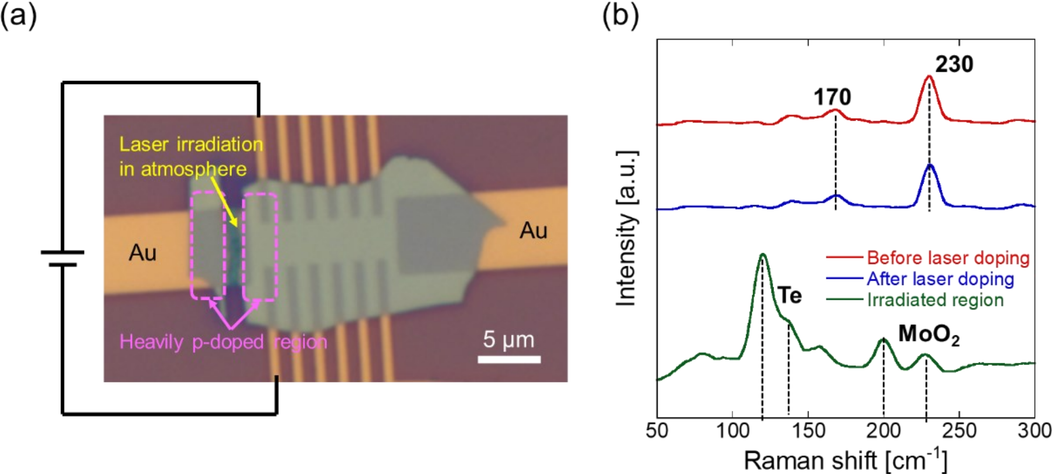

Fig. 3.18 (a) Optical image of the FET sample after scanning irradiation by a high-density laser in the atmosphere. (b) Raman spectra of the original crystal, the irradiated region, and the vicinity of the irradiated area.

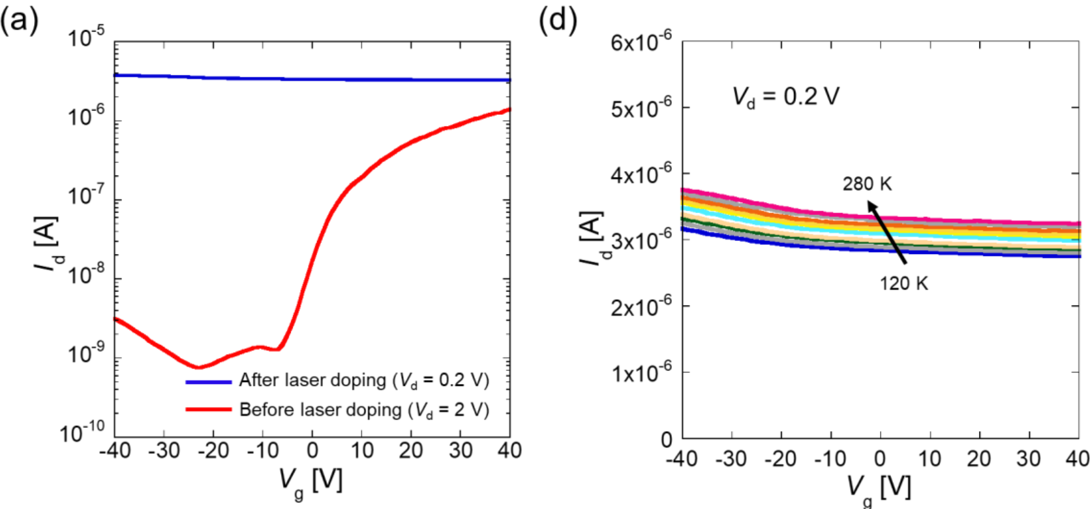

Fig. 3.19 (a) I_d-V_g curves of the $MoTe_2$-FET before and after laser doping at room temperature. (b) I_d-V_g curves of heavily p-doped $MoTe_2$-FET at different temperatures.

Figure 3.20 shows the schematic diagram of the laser-induced p-doping effect. Similar to the case of laser irradiation under vacuum, the crystalline temperature in the vicinity of the irradiated area rises due to the radiation effect of the laser, resulting in a large number of Te vacancies. However, oxygen molecules present in the atmosphere quickly adsorb onto these Te vacancies, acting as p-type dopants. Recently, research on oxygen as a p-type dopant in $MoTe_2$ crystal has also been reported [9]. The absence of any peaks corresponding to Mo oxides in the Raman spectrum indicates that the temperature radiated by the laser to the surroundings is insufficient to oxidize the Mo atoms. **Figure 3.21** shows the DFT calculation of energy level in the band gap of $MoTe_2$ with an oxygen molecule adsorbing onto Te vacancy in a 3×3 lattice. It revealed an appearance of an acceptor level close to the valence band, which is consistent with experimental results. The important experimental fact is that the absorption of oxygen molecules at the Te vacancies for p-type doping needs a heating process; therefore, the n-doped sample prepared by laser irradiation in a vacuum condition does not change the polarity and the carrier density, even when the sample is exposed to oxygen at room temperature. In addition, it is known that Mo oxide acts as a suitable acceptor for

TMDC crystals due to a charge transfer process. The MoO_2 included in the residue inside or around the irradiated region may play the role of an electron acceptor for the 2H-$MoTe_2$ in the vicinity of the irradiated region.

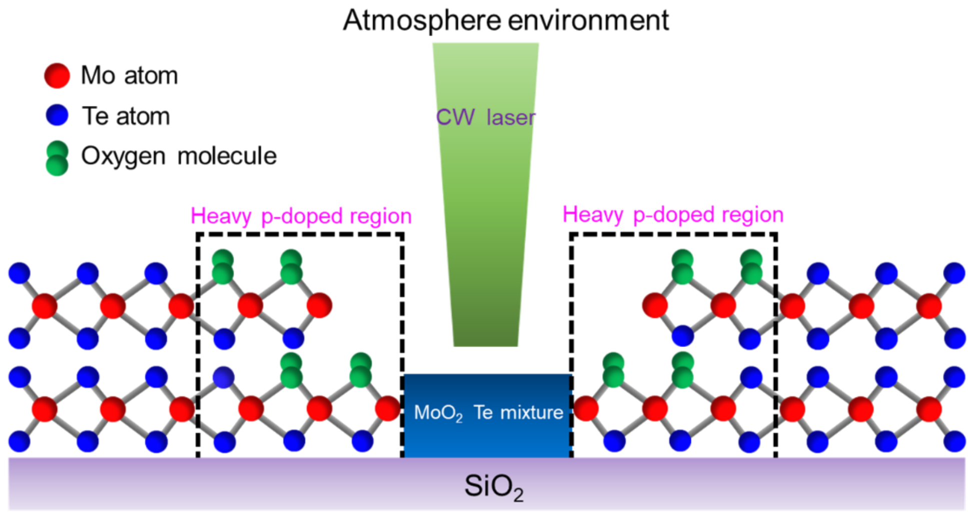

Fig. 3.20 Schematic diagram of heavy p-type doping via laser irradiation in air.

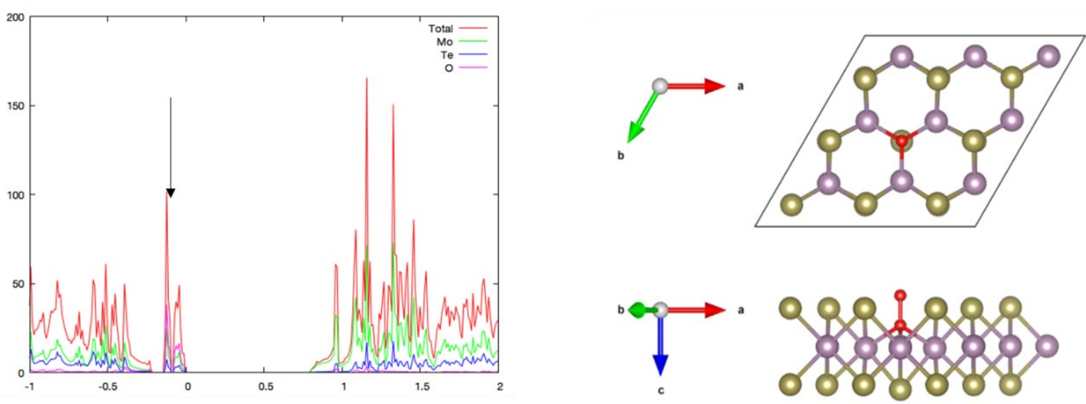

Fig. 3.21 DFT calculation of energy level in the band gap of $MoTe_2$ with an oxygen molecule adsorbing onto Te vacancy.

3.3. Conclusion

This section discussed the impact of high-intensity laser irradiation on the crystal structure and electrical properties of the 2H-$MoTe_2$. Laser irradiation is analogous to a rapid thermal annealing process, and different irradiation environments or crystal regions can result in different induced effects. These effects can be classified into four categories based on the irradiation environment and crystal region, as shown in **Table 3.1**. The area of the directly irradiated region is typically determined by the size of the laser spot. In the atmosphere, Mo atoms react chemically with oxygen at high temperatures caused by laser irradiation, ultimately forming a layer of mixed Mo oxide (MoO_2) and Te atoms with good conductivity. In a vacuum environment, laser irradiation raises the crystal temperature, destabilizing the 2H phase at high temperatures and transforming it into the 1T phase. This laser-induced 1T phase exhibits semi-metallic properties and can remain stable in the atmosphere for a long time. A common feature of laser irradiation in both environments is the reduction in thickness due to the sublimation of the crystal caused by the high temperature of the surface. Moreover, the generated products after irradiation in both cases exhibit semi-metallic electrical characteristics, which are crucial for the application of $MoTe_2$ in integrated circuits. This is because it can form metal-semiconductor homojunction contacts, thus improving contact properties and simplifying integration processes of $MoTe_2$-based electrical devices. The adjacent region near the irradiated area is also heated due to the Gaussian profile of the laser, but the temperature is not as high as in the directly irradiated area; thus, the phenomena mentioned above do not occur. However, the increase in crystal temperature causes an increase in Te vacancies, which significantly affects its electrical properties. In a vacuum, these Te vacancies induced by laser irradiation form a strong donor level in the band gap, resulting in a heavily n-doped region. In the case of irradiation in the atmosphere, oxygen molecules adsorb onto the Te vacancies instantly, and these oxygen molecules form an acceptor level in the band gap, resulting in a heavily p-doped region. Achieving heavy doping in 2D materials has always been challenging; however, due to its region selectivity and

controllability, this laser-induced doping technology can be widely used in various electronic devices, such as FETs and TFETs. Additionally, ultra-high-intensity laser irradiation also has an etching effect on 2D materials, providing selectivity for the etching process of 2D electrical devices in the future.

Crystal position / Irradiation environment	Irradiated region	The vicinity of the irradiated region
Air	Layer-thinning MoO_2, Te mixture	Heavy p-doping
Vacuum	Layer-thinning Phase transition: 2H to 1T	Heavy n-doping

Table 3.1 Effect of high-intensity laser irradiation on 2H-$MoTe_2$.

Reference

[1] S. Cho, S. Kim, J. H. Kim, et al. Science **349**, 625 (2015).
[2] K. Sakanashi, H. Ouchi, K. Kamiya, et al. Nanotechnology **31**, 205205 (2020).
[3] Q. Luo, G. Tang, M. Sun, et al. Optical Materials Express **10**, 1072 (2020).
[4] R. Narro-García, N. Méndez, L. M. Apátiga, et al. International Journal of Electrochemical Science **12**, 3907 (2017).
[5] T. A. Empante, Y. Zhou, V. Klee, et al. ACS nano **11**, 900 (2017).
[6] M. Kan, H. G. Nam, Y. H. Lee, et al. Physical Chemistry Chemical Physics **17**, 14866 (2015).
[7] I. Stenger, L. Schué, M. Boukhicha, et al. 2D Materials **4**, 031003 (2017).
[8] X. Liu, A. Islam, J. Guo, et al. ACS nano **14**, 1457 (2020).
[9] S. Y. Seo, J. Park, J. Park, et al. Nature Electronics **1**, 512 (2018).

4. Contact engineering on $MoTe_2$-FET via laser irradiation

4.1. Polymorphic contact

In 2D-FETs, the contact properties play a crucial role, directly affecting the electrical conductivity, switching speed, and power consumption. For $MoTe_2$, the poor contact properties resulting from the severe FLP effect have significantly limited its applications in electronic devices. Therefore, research to improve its contact properties has been frequently reported recently. One meaningful approach involves utilizing the polycrystalline nature of $MoTe_2$ by exploiting its 1T' phase, which exhibits semi-metallic characteristics, to contact the 2H semiconductor phase, thus obtaining favorable contact properties. **Figure 4.1** shows the 1T'/2H/1T' polymorphic junction obtained by the CVD growth method and the construction of metal electrodes on the 1T' semi-metallic phase, achieving an ohmic contact with higher carrier injection efficiency than traditional metal contacts [1]. Due to the low density of states of the semimetal at the Fermi level, the MIGS effect can be avoided, and this structure can also prevent damage to the semiconductor channel during metal deposition, indicating that the 1T' semi-metallic phase is well-suited as a contact metal for the 2H semiconductor phase. However, obtaining this structure via the CVD method is time-consuming and challenging to integrate on a large scale. Thus, this study provides a simple, efficient, and scalable polymorphic contact method. As stated before, the proper high-intensity laser irradiation on $MoTe_2$ crystals in a vacuum induces a transition from the 2H phase to the 1T phase. Therefore, in this study, a 1T/2H/1T polymorphic junction structure was constructed via localized laser irradiation, and the properties of $MoTe_2$-FET with 1T-phase contact were investigated. In addition, since previous studies did not demonstrate the polarity of 1T'-phase contact FET, this study also confirmed the polarity and contact properties of 1T'-phase contact FET by constructing 1T'/2H/1T' heterojunction structure via dry transfer techniques.

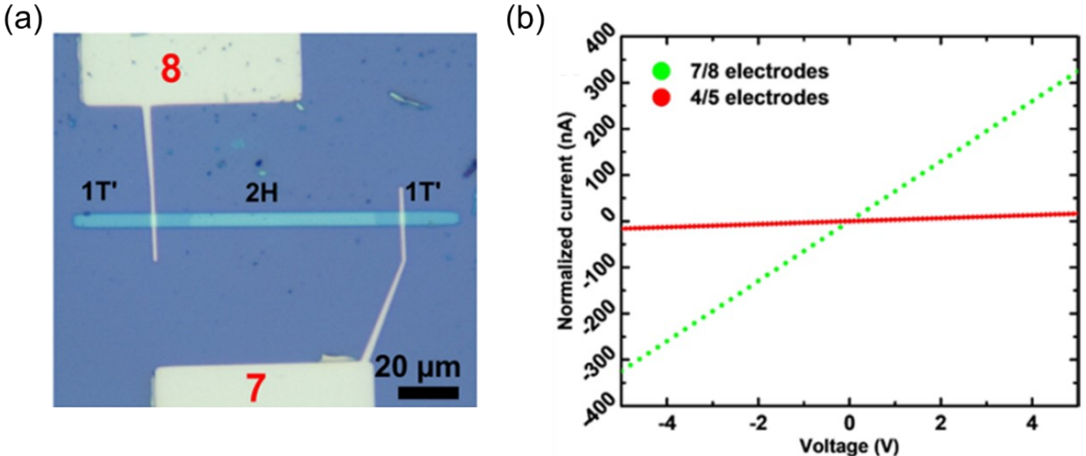

Fig. 4.1 (a) 1T'/2H/1T' homojunction obtained by CVD growth method. (b) I_d-V_d curves of 1T' contact and conventional metal contact [1].

4.1.1. Laser-induced 1T-phase contact

A 1T/2H/1T polymorphic junction structure based on a single $MoTe_2$ crystal was formed by irradiating only both sides of the 2H phase in a vacuum. A crystal of a large length (~ 30 μm) was used to avoid the influence of laser irradiation on the channel region. The laser-induced 1T phase was used to contact the 2H phase instead of the metal contact. Metal electrodes (Cr/Au) were then fabricated to the laser-induced 1T phase and the middle part of the 2H phase, respectively. **Figure 4.2** shows the schematic and the optical image of the structure, including 1T contact-FET and Cr contact-FET. The channel length of 1T contact-FET is about three times that of Cr contact-FET, which means that its channel resistance is almost three times that of Cr contact-FET because of the same channel widths of the two FETs.

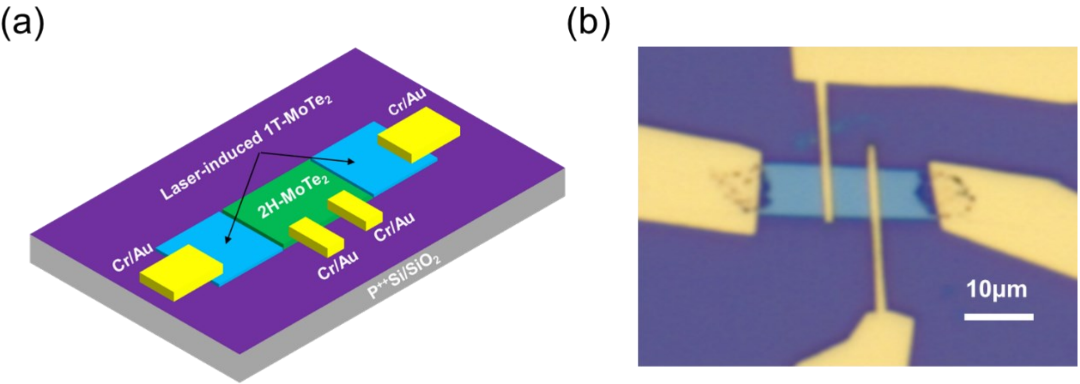

Fig. 4.2 Schematic (a) and the optical image (b) of the FETs sample with a 1T/2H/1T homojunction structure formed by local laser irradiation.

Figure 4.3 (a) shows the I_d-V_g curves of 1T contact-FET and Cr contact-FET at room temperature, respectively. It can be observed that both the 1T and Cr contact-FETs exhibit n-type dominant ambipolar transfer characteristics. However, compared to the Cr contact, the 1T contact demonstrates a larger on/off ratio and on-state current despite its higher channel resistance. Additionally, it shows a lower *SS* value, implying a faster switching speed. This suggests that 1T contact-FET has higher carrier injection efficiency than Cr contact-FET. **Figure 4.3 (b)** shows the I_d-V_d curves of these two FETs at room temperature. The 1T contact-FET shows ohmic contact characteristics, while the Cr-contact shows Schottky contact, indicating a lower Schottky barrier is obtained at the interface between the laser-induced 1T phase and the original 2H phase.

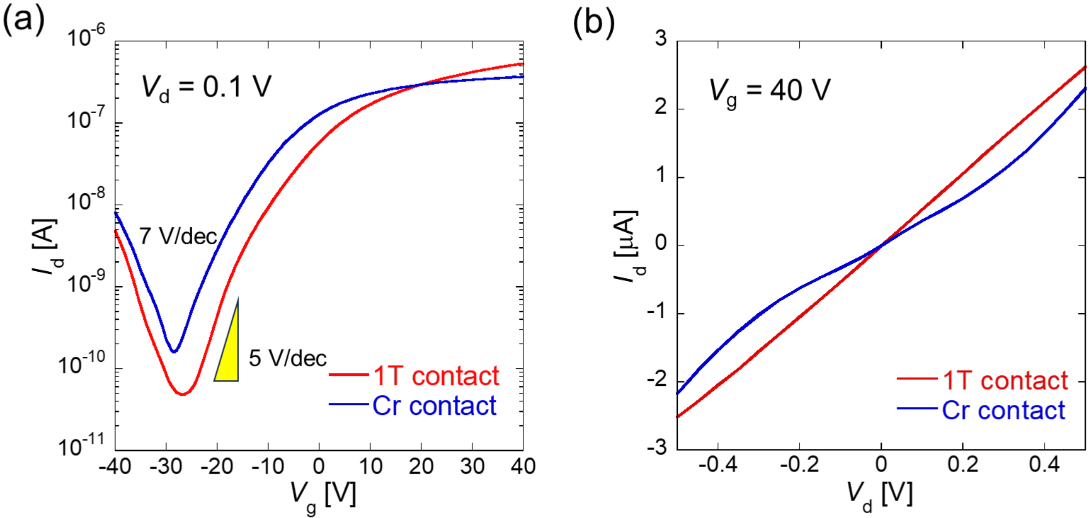

Fig. 4.3 (a) I_d-V_g and (b) I_d-V_d curves of the 1T contact-FET and Cr contact-FET at room temperature.

I_d-V_g curves at different temperatures for both FET were also measured, as shown in **Fig. 4.4**. The distinction between the 1T contact and Cr contact is evident when the FET is in the on state: the on-state current of the 1T contact remains unaffected by

temperature variations, whereas the Cr contact demonstrates a notable temperature-dependent characteristic. This discrepancy suggests a higher Schottky barrier exists at the interface between Cr and $MoTe_2$.

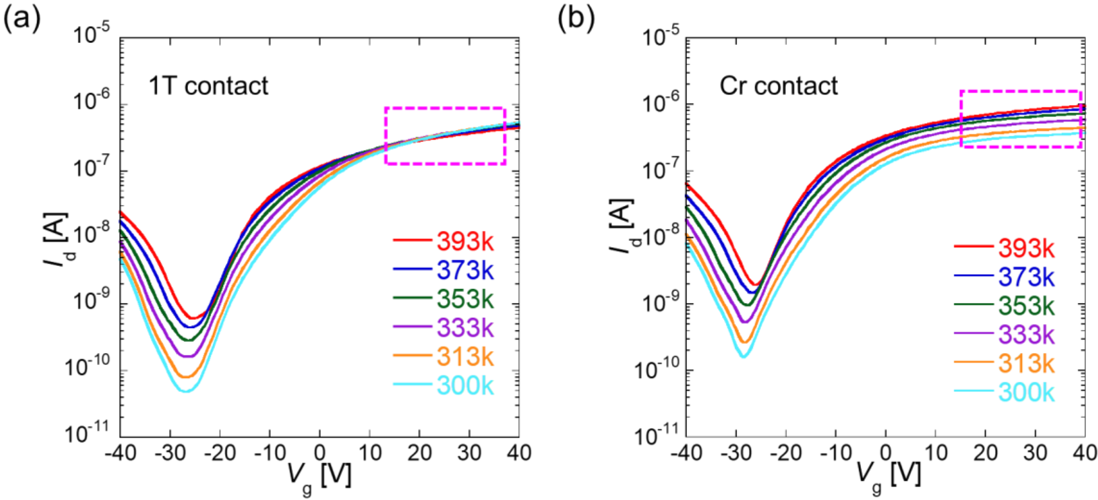

Fig. 4.4 I_d-V_g curves (V_d = 0.1 V) of the 1T contact-FET (a) and Cr contact-FET (b) at different temperatures.

Due to the FLP effect, the Schottky-Mott rule no longer applies to extracting the Schottky barrier, and thermionic emission equations are required in this case. The derivation of 2D and 3D thermionic emission equations is described as follows [2,3]:

Thermionic emission:

$$I_{S\to M} = Aqn\left(\frac{kT}{2\pi m^*}\right)^{\frac{1}{2}} \exp\left(-\frac{q(V_{bi}-V)}{kT}\right)] \tag{4.1}$$

Carrier concentration:

$$n = \int_{E_C}^{\infty} g(E)\,f(E)dE \tag{4.2}$$

Fermi-Dirac distribution function:

$$f(E) = \exp(\frac{-(E-E_f)}{kT}) \quad @(E > E_{C'}E_C\ \ E_f \gg kT) \tag{4.3}$$

3D density of states & thermionic emission:

$$g(E)_{3D} = \frac{4\pi(2m^*)^{\frac{3}{2}}}{h^3}\sqrt{E-E_C} \quad (4.4)$$

$$n_{3D} = 2(\frac{2\pi m^* kT}{h^2})^{\frac{3}{2}}\exp(\frac{-(E-E_f)}{kT}) \quad (4.5)$$

$$I_{3D} = AA_{3D}^*T^2\exp\left(-\frac{q\emptyset_B}{kT}\right)[1-\exp\left(-\frac{qV_d}{kT}\right)] \quad (4.6)$$

$$A_{3D}^* = \frac{4\pi q m^* k^2}{h^3}$$

2D density of states & thermionic emission:

$$g_{2D} = \frac{4\pi m^*}{h^2}$$

$$n_{2D} = \frac{4\pi m^* kT}{h^2}\exp(\frac{-(E_C-E_f)}{kT}) \quad (4.7)$$

$$I_{2D} = WA_{3D}^*T^{\frac{3}{2}}\exp\left(-\frac{q\emptyset_B}{kT}\right)[1-\exp\left(-\frac{qV_d}{kT}\right)] \quad (4.8)$$

$$A_{2D}^* = \frac{q\sqrt{8\pi m^* k^3}}{h^2}$$

Due to

$$qV_d \gg kT$$

Thus,

$$I_{2D} = WA_{3D}^*T^{\frac{3}{2}}\exp\left(-\frac{q\emptyset_B}{kT}\right) \quad (4.9)$$

$$\emptyset_B = \frac{k}{q}\left[\frac{\Delta\ln\left({I_d}/{T^{\frac{3}{2}}}\right)}{\Delta T^{-1}}\right] \quad (4.10)$$

Here, I_d is the drain current, W the channel width, A_{2D}^* is the modified Richardson constant, k is the Boltzmann constant, q is the electrical charge, m^* is the effective mass, $\emptyset_B$ is the Schottky barrier height, and V_d is the applied drain voltage. $\left[\frac{\Delta\ln\left({I_d}/{T^{\frac{3}{2}}}\right)}{\Delta T^{-1}}\right]$ is the slope of the Arrhenius curve for current, as shown in **Fig. 4.5**.

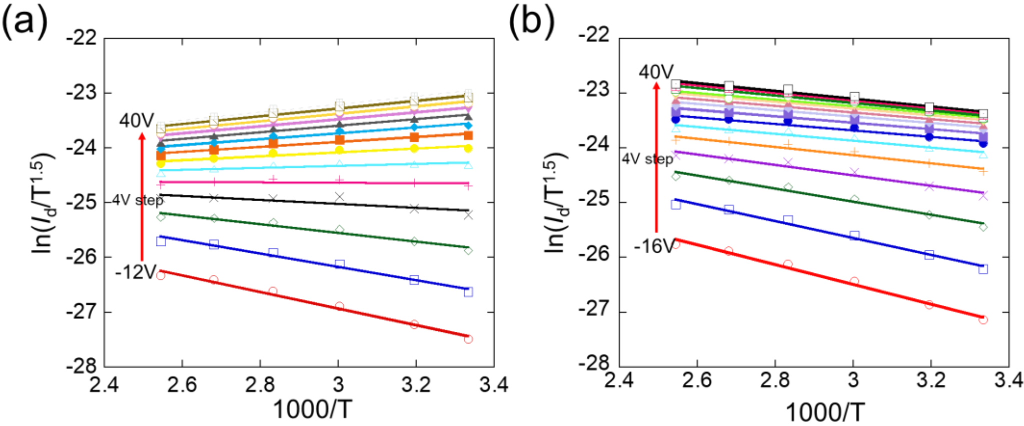

Fig. 4.5 Arrhenius curve for current of (a)1T contact-FET and (b) Cr contact-FET.

The Schottky barrier heights at different gate voltages of these two FETs were calculated by extracting the slope of each Arrhenius curve. The effective barrier height can be derived from the turning point of the slope of the curve corresponding to the flat band condition. The effective barrier of 1T contact-FET was almost 0 eV, indicating no Schottky barrier was formed at the contact interface, while Cr-contact showed 90 meV of the n-branch conduction, as shown in **Figs. 4.6 (a)** and **(b)**. The extracted SBH of 90 meV suggests a strong FLP effect occurred at the interface between Cr and 2H-$MoTe_2$, which was caused by metal deposition. In the ideal case, when a 2D semiconductor is contacted by a metal with a work function higher than its conduction band, the electrons will flow into the semiconductor from the metal until the Fermi level of the semiconductor is consistent with the work function of the metal, resulting in a heavy n-doped contact area underneath the metal. Thus, the Schottky barrier will be zero in this case. Unfortunately, it's very challenging to accurately measure the work function of the laser-induced 1T phase because we currently cannot obtain a very uniform and complete 1T phase crystal via laser irradiation. However, in our case, the vicinity of the laser-induced 1T phase was heavily n-doped by the laser irradiation, as introduced before. **Figure 4.6 (c)** shows the energy band of the 1T contact-FET and Cr contact-FET at the on- and off-state. In the on-state of 1T contact-FET, electrons tunnel from the 1T phase to the heavily n-doped region and then flow into the channel without the

Schottky barrier. However, in the case of the Cr contact-FET, the presence of the Schottky barrier necessitates electrons from the metal to overcome the barrier, leading to thermal conduction. Thus, the on-state current of 1T contact-FET is almost independent of temperature, while the Cr one is dependent.

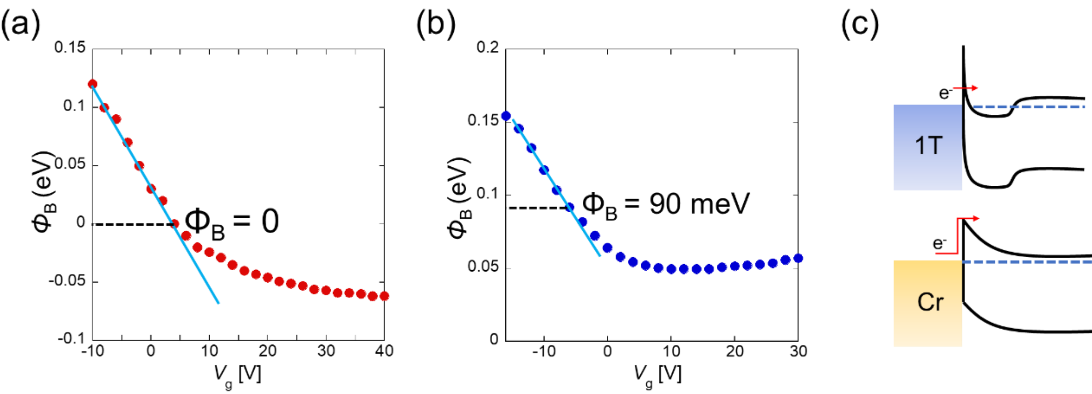

Fig. 4.6 Calculated Schottky barrier heights of 1T contact-FET (a) and Cr contact-FET (b) at n-branch conduction. Energy band of 1T contact and Cr contact-FET at on-state.

4.1.2. 1T'-phase top contact

The laser-induced-1T contacted 2H-$MoTe_2$ FET exhibits n-type polarity, and this part will discuss the polarity and properties of the 1T' contacted one. However, the 1T'-$MoTe_2$ cannot be obtained through phase transition; thus, the multilayer 1T'-$MoTe_2$ was obtained by exfoliating bulk crystal in the same way as 2H-$MoTe_2$. A 1T'/2H/1T' heterojunction was achieved by transferring the 1T'-$MoTe_2$ at both sides of a 2H-$MoTe_2$ crystal. The schematic view and optical microscope image of the 1T'/2H/1T' heterojunction are shown in **Figs. 4.7 (a)** and **(b)**, respectively. No bubbles and impurities can be observed in the contact area between the 1T'- and 2H-$MoTe_2$ crystals, indicating relatively clean 2D-2D contact formation at the interface. The electrical properties of 1T'-$MoTe_2$ at room temperature were first confirmed as shown in **Figs. 4.8 (a)** and **(b)**. The 1T'-$MoTe_2$ displayed a semi-metallic characteristic, wherein the current remained unaffected by the gate voltage. The two-terminal resistance, including

the contact resistance and sheet resistance extracted from the I_d-V_d curve, is 600 Ω, which is negligible in the property of 1T' contact-FET.

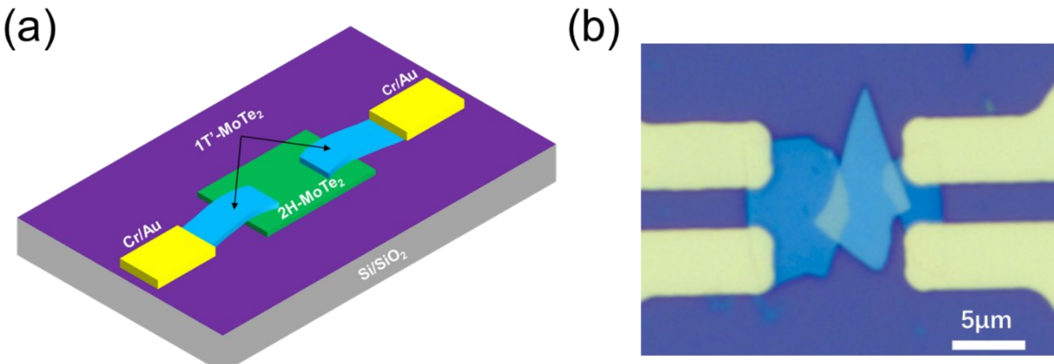

Fig. 4.7 Schematic (a) and the optical image (b) of the 1T'/2H 1T' heterojunction structure formed by the dry transfer process.

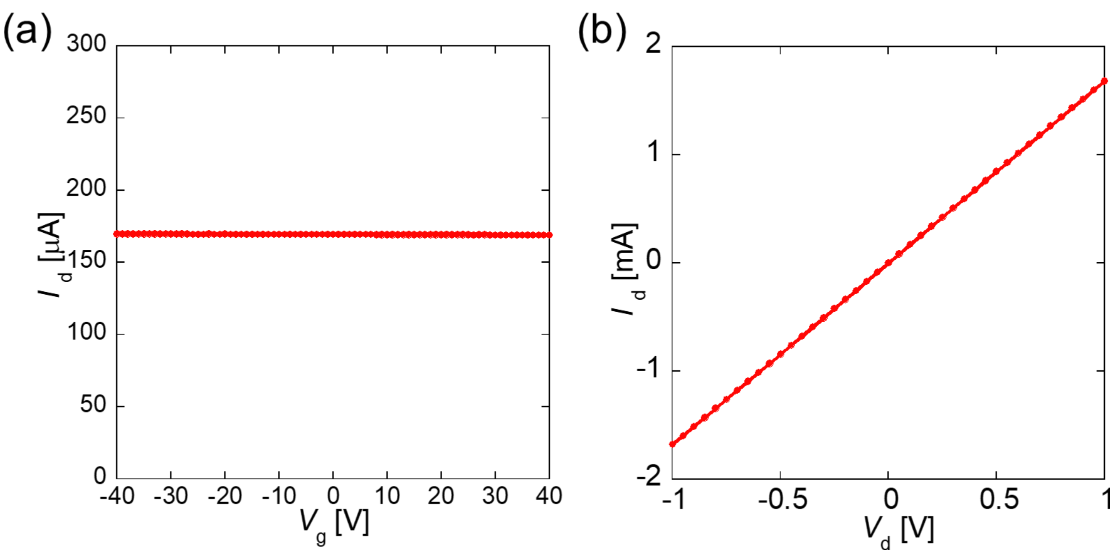

Fig. 4.8 Electronic properties of 1T'-$MoTe_2$ at room temperature: (a) I_d-V_g curve and (b) I_d-V_d curve.

The I_d-V_g curves of the 1T' contact-FET were measured at various temperatures, as shown in **Fig. 4.9**. Drain voltage $V_d = |0.1|$ V was applied for every measurement. The 1T' contact-FET exhibited a p-type semiconducting behavior however the current was also increased slightly by applying a high positive gate voltage above room temperature. The on/off ratio reached 10^5 at room temperature and reduced gradually with increasing

temperature due to increasing the off-state current values caused by the increased thermal energy. At low temperatures, low thermal energy causes a reduction in the number of carriers transmitted across the barrier, resulting in a decrease in the "ON" state current. The temperature dependence of the p-branch current at low temperatures indicates that the hole transportation is thermal-dominated.

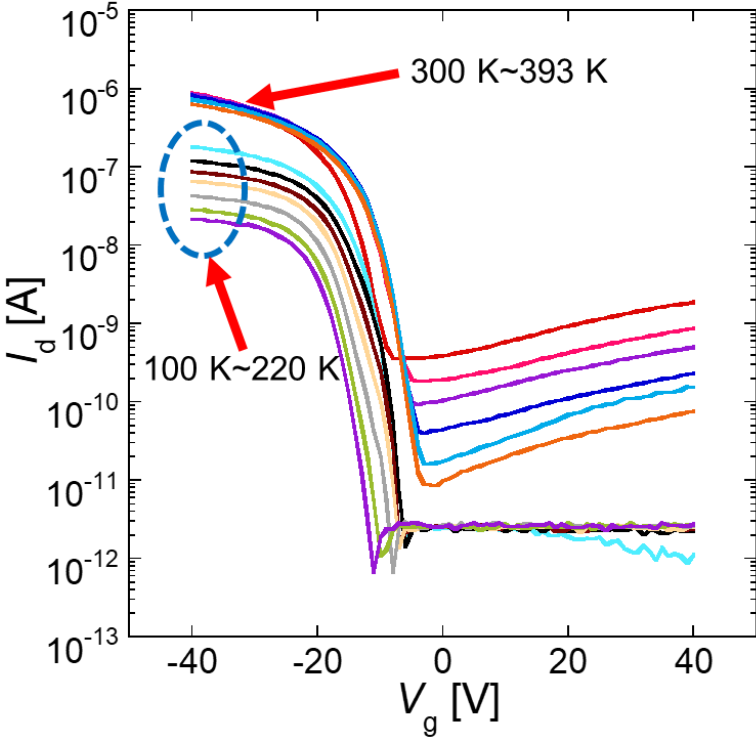

Fig. 4.9 I_d-V_g curves of 1T' contact-FET at different temperatures (V_d = |0.1| V).

The performance of the device at room temperature is particularly important. **Figures 4.10 (a)** and **(b)** reveal the output properties at room temperature under the negative and the positive gate voltage conditions, respectively. By applying a negative gate voltage, the hole current is initially linearly increased at a small bias region and then gradually saturated at a strong bias region. Meanwhile, the 1T' contact-FET exhibited Schottky contact characteristics with small electron current at the n-branch when the positive gate voltage was applied, indicating that electrons are conducting across the Schottky barrier through thermal excitation are more difficult than holes; that is, the Schottky barrier height of the n-branch is much higher than that of the p-branch.

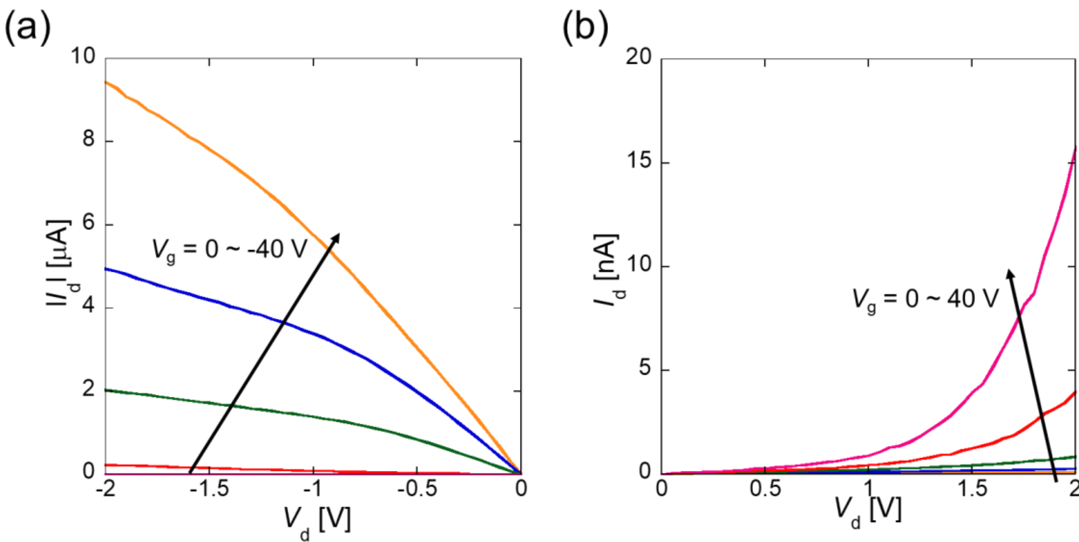

Fig. 4.10 I_d-V_d curves of 1T' contact-FET at (a) p-branch and (b) n-branch.

To identify this transmission mechanism, we extracted the Schottky barrier between the 1T'-$MoTe_2$ and 2H-$MoTe_2$ and clarified the evolution of the barrier height with sweeping gate voltage. Due to the hole current having obvious temperature dependence at low-temperature conditions, we extracted the Schottky barrier of the p-branch by using transfer curves at 100 K~220 K. The Arrhenius plot curve and Schottky barrier height (SBH) with respect to negative gate voltage are shown in **Figs. 4.11 (a)** and **(b)**, respectively. The inflection point of the curve slope at V_g = - 18 V exhibits the flat band condition and the effective SBH was approximately 39 meV for the hole injection. The evolution of the energy band diagram of the contact interface with sweeping the gate voltage was described in **Fig. 4.12**. It notes here that the work function of exfoliated 1T'-$MoTe_2$ was 4.86 eV measured by electrostatic force microscope (EFM), indicating the work function of 1T'-$MoTe_2$ is very close to the level of the valence band edge of the 2H-$MoTe_2$. Without the FLP effect, the SBH of the p-branch can be derived from the Schottky-Mott rule, which was given by the difference between the work function of 1T'-$MoTe_2$ and the valence band energy level of 2H-$MoTe_2$. Since our result calculated from thermionic equations is almost the same as the theoretical value of 40 meV derived from the Schottky-Mott rule, it proves that no FLP effect occurs at the

contact interface between 1T'- and 2H-$MoTe_2$. Since the point corresponding to the minimum current level appeared at the slightly negative gate voltage region, the Fermi level of the 2H-$MoTe_2$ was not originally situated at the center of the bandgap but a little close to the conduction band. It may be caused by the n-type doping effect from the residue of the polycarbonate used during the transfer process. After the 1T'-$MoTe_2$ contacting with the 2H-$MoTe_2$, to flatten the Fermi level of the two materials at the same level, electrons flow from 2H-$MoTe_2$ to 1T'-$MoTe_2$, causing the energy band at the interface of the 2H-$MoTe_2$ bend downward. Applying the positive gate voltage caused the Fermi level to approach the conduction band gradually, and the energy band was strongly bent downward. At high temperatures, some electrons with higher energy undergo thermal-assisted tunneling [4], thus forming a small electron current. At low temperatures, no current was generated since thermal energy is not enough to excite electrons to overcome the barrier. However, when the negative gate voltage was applied, the Fermi level of 2H-MoTe2 gradually approached the valence band, decreasing the degree of downward bending at the small gate voltage region. The minimum current point and the flat band appeared at Vg = -10 V and Vg = -18 V, respectively. The energy band started to bend upwards by increasing the negative gate voltage further from the flat band voltage of -18 V and the current was consequently enhanced.

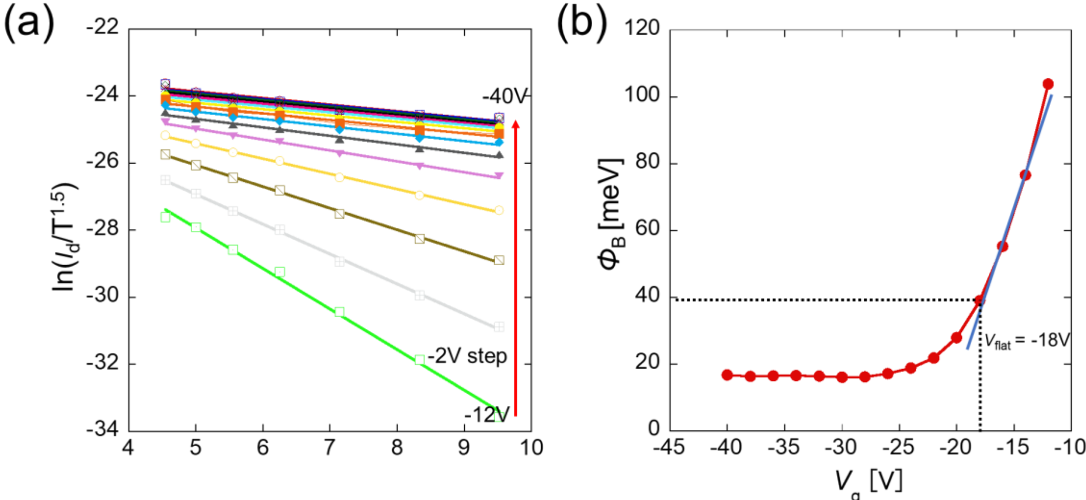

Fig. 4.11 Arrhenius spot (a) and Schottky barrier height (b) with negative gate voltage.

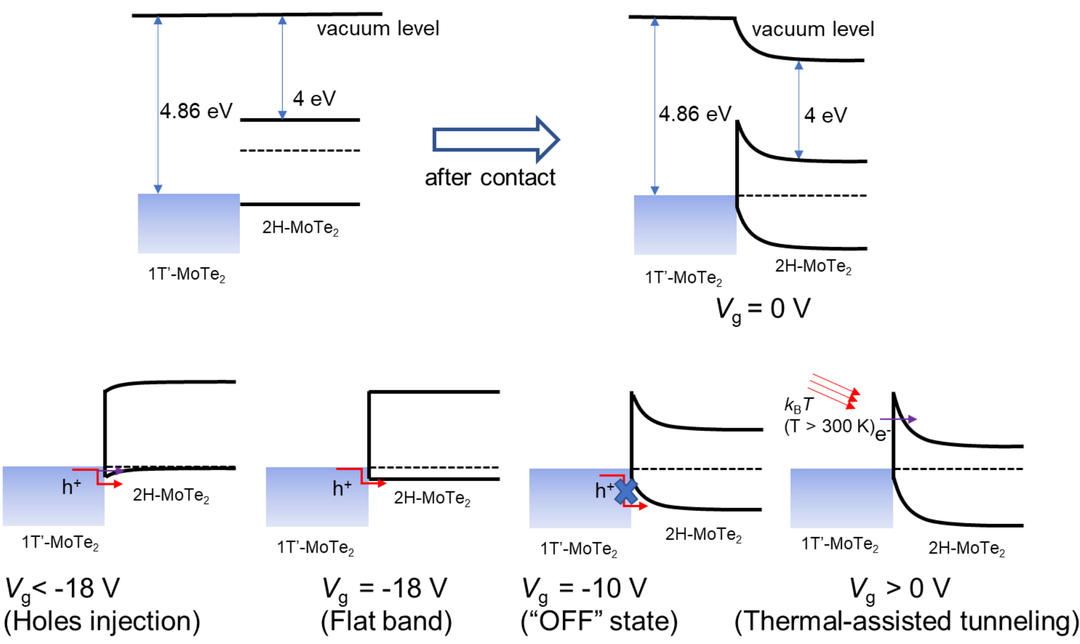

Fig. 4.12 Evolution of the energy band diagram of 1T'-2H interface with the sweeping gate voltage.

4.2. Contact doping

Contact doping is also an excellent way to decrease contact resistance by reducing the Schottky barrier width at the interface between the metal and semiconductor. However, traditional heavy doping methods, such as ion implantation, are significantly challenging to apply to TMDC materials because of the severe damage caused to the crystal, and thermal repair is not applicable. Chemical doping is a promising method for TMDC materials; however, its doping concentration is usually low [5]. So far, it has only been used to dope the carrier to change the polarity of the device and improve its performance [6]. Although there is a report on chemically heavy n-type doping of 2H-$MoTe_2$ crystal using a benzyl viologen solution, this doping method is not regioselective and is unsuitable for large-scale integrated circuits [7]. Recently, several studies have reported using ozone by UV irradiation to form a WO_x layer with a high work function on the surface of WSe_2, which absorbs electrons from the underlayer and thus heavily dopes the crystalline in p-type by charge transfer mechanism [8,9]. However, this method is unstable, and regioselective doping is difficult. In addition, the technique is suitable only for p-type doping, and whether the WO_x layer participates in the conduction has not been clarified yet. Thus, in this study, the contact doping method via laser irradiation is applied to thin the Schottky barrier caused by the FLP effect and reduce the contact resistance. **Figure 4.13** shows a schematic diagram and an optical microscope image of the contact-doped $MoTe_2$-FET. Source and drain electrodes were deposited on the two heavily n-doped regions prepared by laser irradiation in a vacuum condition. For the $MoTe_2$-crystal of the contact region, due to the high intensity of the laser, the directly irradiated region undergoes sublimation and disappears, while the crystal near the irradiated area is preserved as the part in contact with the metal. This region is heavily n-doped due to the Te vacancies induced by laser radiation; thus, the contact interface essentially forms a model of degenerate semiconductor-metal contact.

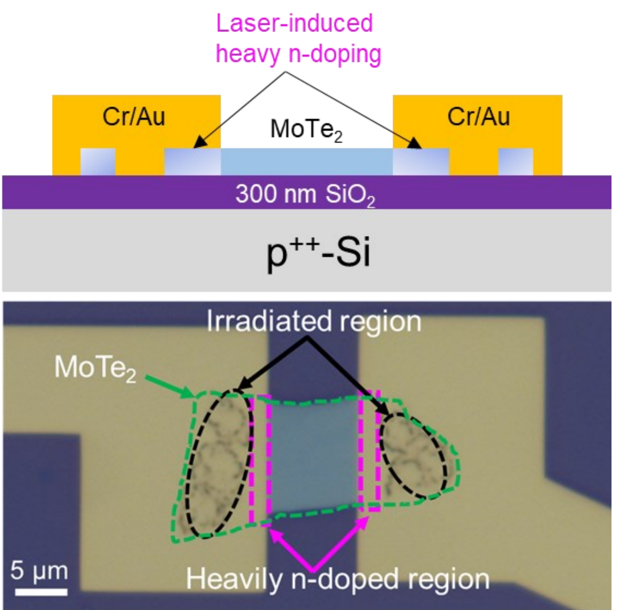

Fig. 4.13 Schematic diagram and an optical microscope image of the contact-doped $MoTe_2$-FET.

The contact-doped $MoTe_2$-FET exhibits n-type transfer characteristics with a threshold voltage of 10 V, as shown in **Fig. 4.14 (a)**. It demonstrates a remarkably high on/off ratio at a low temperature of 125 K. I_d-V_g curves were measured at different temperatures, as shown in **Fig. 4.14 (b)**, revealing a significant current temperature dependence during the transition from the off to the on-state. Once the FET transitions into the on-state, the temperature dependence of the current notably diminishes. These results suggest the persistence of a Schottky barrier despite doping in the contact region. However, this barrier is exceedingly small, as carrier conduction becomes uninhibited by it upon the application of a gate voltage surpassing the V_{th}. The I_d-V_d curves of conventional $MoTe_2$-FETs typically exhibit a Schottky characteristic. This indicates that the FET's performance is constrained in a low-bias region due to the substantial energy barrier at the contact interface between the metal and the $MoTe_2$. However, the contact-doped $MoTe_2$-FET shows good ohmic characteristics at room temperature, as shown in **Fig. 4.15 (a)**. Moreover, even at 125 K, the sample still shows ohmic features, as shown in **Fig. 4.15 (b)**, indicating that suitable contact properties are obtained via the contact doping technique by laser irradiation.

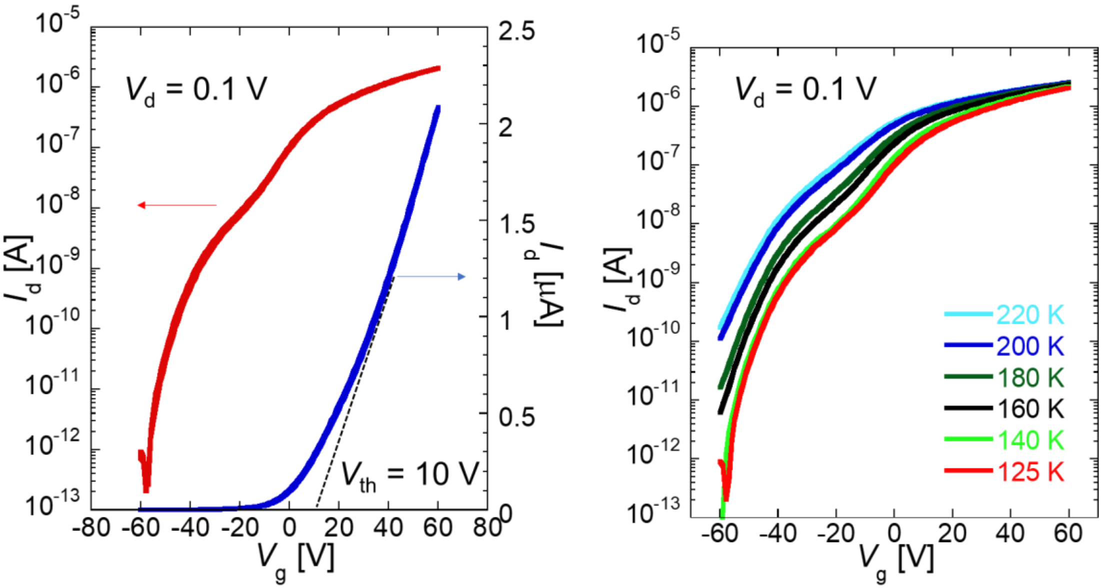

Fig. 4.14 (a) I_d-V_g curve measured at 125 K in logarithmic and linear form. (b) I_d-V_g curves at different temperatures.

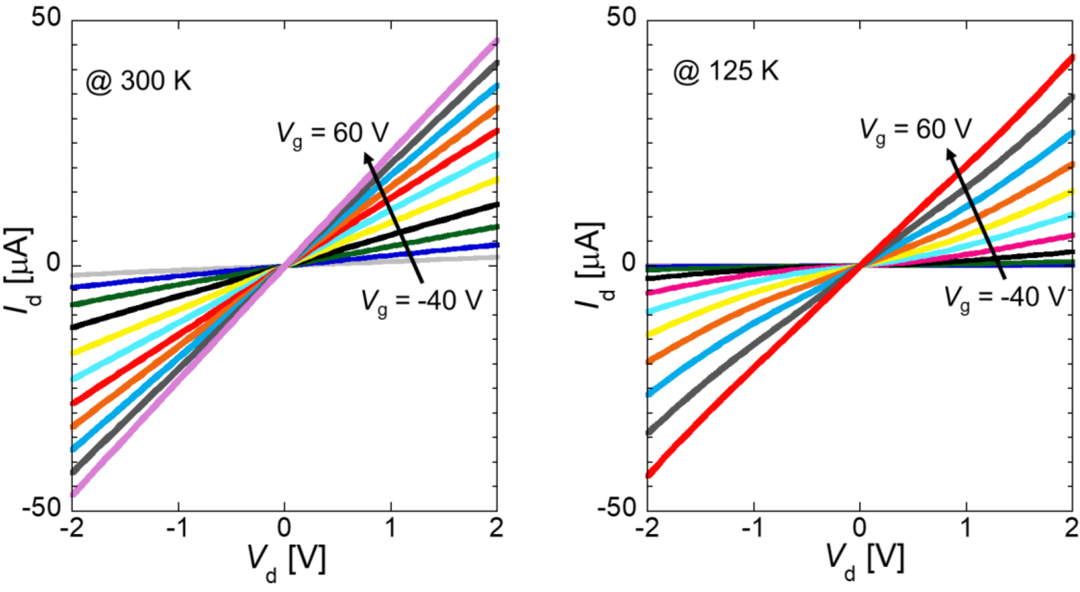

Fig. 4.15 I_d-V_d curves measured at (a) room temperature and (b) low temperature.

The Schottky barrier height and contact resistance are estimated using the thermionic equations. **Figure 4.16 (a)** shows the Schottky barrier height at various gate voltages, and the effective barrier height is derived from the turning point of the slope, which shows just 6 meV. This indicates that the sample can exhibit good contact properties when the temperature is above 70 K. This is consistent with the experimental result where the FET maintains ohmic contact characteristics even at low temperatures of 125 K. To prove the excellent contact property further, contact resistance is estimated using the Y-function method, which is defined as

$$Y = \frac{I_d}{\sqrt{g_m}} = \frac{I_d}{\sqrt{dI_d/dI_g}} \tag{4.11}$$

Where g_m is the transconductance defined by dI_d/dV_g. The threshold voltage (V_{th}) is extracted through the Y-V_g curve. Then, the low-field mobility (μ_0) can be calculated as

$$Y = \left(V_g - V_{th}\right)\sqrt{\frac{W}{L} C_{ox}\mu_0 V_d} \tag{4.12}$$

Here, L is the channel length, and C_{ox} is the capacitance of the gate insulator. Next, the mobility attenuation factor (θ) is obtained by using the equation of

$$I_d = \frac{W}{L} C_{ox}\left(V_g - V_{th}\right)\frac{\mu_0}{1+\theta\left(V_g - V_{th}\right)} \times V_d \tag{4.13}$$

Finally, the contact resistance can be calculated from the relation between θ and R_C, namely,

$$\theta = \frac{W}{L}\mu_0 C_{ox} R_c \tag{4.14}$$

For the contact resistance in the on-state (V_g > 10 V) at room temperature, an average value of 56 kΩμm was obtained, as shown in **Fig. 4.16 (b)**. Such a small contact resistance proves that good contact properties have been achieved in contact-doped $MoTe_2$-FET.

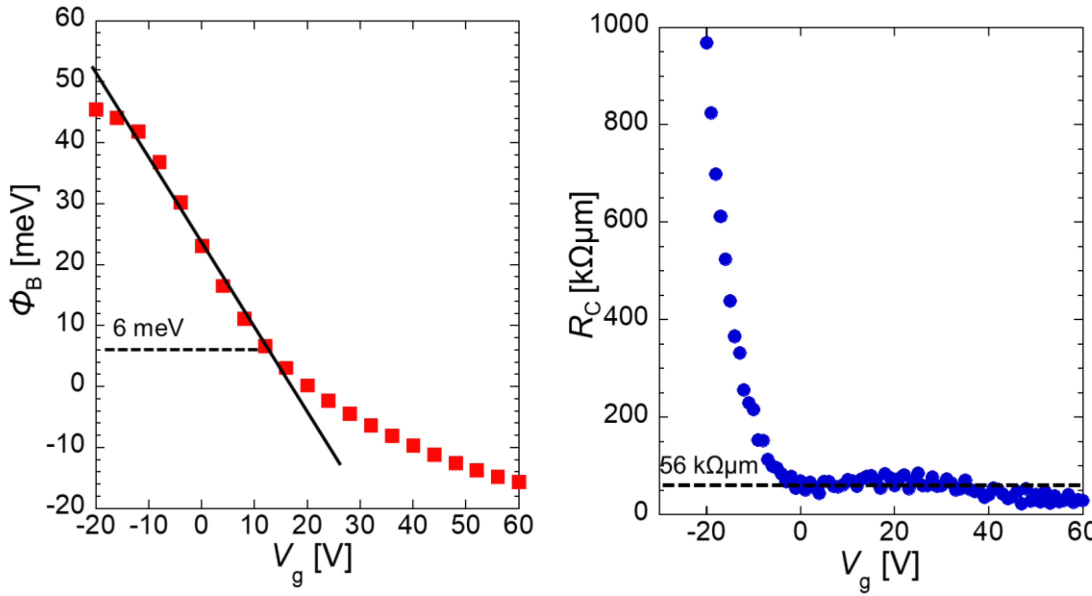

Fig. 4.16 (a) Schottky barrier extraction of contact-doped $MoTe_2$-FET. (b) Calculated contact resistance using the Y-function method.

The mobility is the speed of charge carriers (electrons or holes) moving in a semiconductor per unit electric field. In electronic devices such as FET, mobility is a critical parameter for evaluating device performance, directly impacting response time, current driving capability, and power consumption. The two-terminal mobility in 2D-FET can be calculated using the following formula:

$$\mu = \frac{L}{W}\frac{1}{C_{ox}}\frac{dI_d}{dV_g} \tag{4.15}$$

Where L and W are the channel length and width, C_{ox} is the capacitance of gate oxide. **Figure 4.17** shows the temperature dependence of the mobility at V_g = 40 V. The mobility at room temperature is 22 cm^2/Vs. If the contact properties are poor, the mobility decreases with decreasing temperature due to the high contact resistance [10]. However, the mobility of this sample increases with decreasing temperature, which indicates that the phonon scattering process in the channel is the dominant mechanism in the sample rather than the contact barrier. These experimental results prove that laser irradiation is a suitable method for contact doping to enhance the device performance of the $MoTe_2$-FET. Similarly, doping the contact region through laser irradiation in an atmosphere environment can also improve the contact properties of p-channel $MoTe_2$-

FETs.

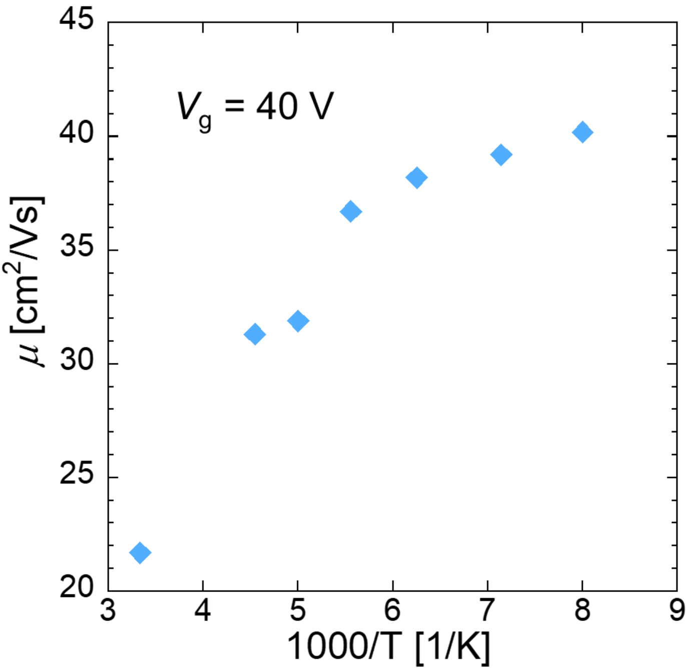

Fig. 4.17 (a) Two-terminal mobilities at different temperatures.

4.3. CMOS inverter fabrication

Contact doping for $MoTe_2$-FET not only enhances the contact characteristics but also allows for the control of the FET's polarity. Due to the small bandgap of $MoTe_2$, applying a gate voltage can change the position of the Fermi level, leading to the formation of both n-FET and p-FET operations, typically exhibited as ambipolar transfer characteristics. However, ambipolar characteristics are not suitable for the application of logic devices. In this study, contact doping through laser irradiation enhances one polarity's conductivity, transforming it into either an n-channel or p-channel dominated FET. Additionally, an *h*-BN encapsulation has been applied to both FETs' channels to improve carrier mobility and safeguard the channel from external perturbations. Lastly, these two FETs are interconnected to form a CMOS inverter, exhibiting outstanding performance with a high gain value.

Figure 4.18 (a) ~ (e) illustrates the fabrication process of the sample. Firstly, a graphite/*h*-BN stack was prepared on a substrate by dry transfer process to pick up the materials in order. Graphite was connected to a metallic pad used as a global back gate, while *h*-BN served as the gate dielectric. Subsequent to the fabrication of source electrodes (Cr/Pd) on the *h*-BN layer, two $MoTe_2$ flakes, with an *h*-BN covering the middle region, were precisely positioned onto the bottom *h*-BN substrate, establishing electrical contact with the prefabricated electrodes via the dry transfer process, as depicted in **Fig. 4.18 (c)**. Subsequently, drain electrodes were constructed on the lateral side of the two $MoTe_2$ flakes. To reduce the barrier height on the drain side, In and Pd were used as contact metals for the n-FET and p-FET, respectively. Finally, the region that was exposed to air on one of the $MoTe_2$ flakes was selectively irradiated by a laser under a vacuum condition, resulting in the formation of a heavily n-doped region in the contact area. Conversely, the other $MoTe_2$ flake was irradiated in the atmosphere, leading to the formation of a heavily p-doped region in the contact area, as shown in **Fig. 4.18 (e)**. The top *h*-BN was used as a protective layer to avoid the underlayer channel being influenced by laser irradiation. Consequently, each $MoTe_2$-FET featured channel encapsulation with top and bottom *h*-BN layers to maintain its intrinsic state.

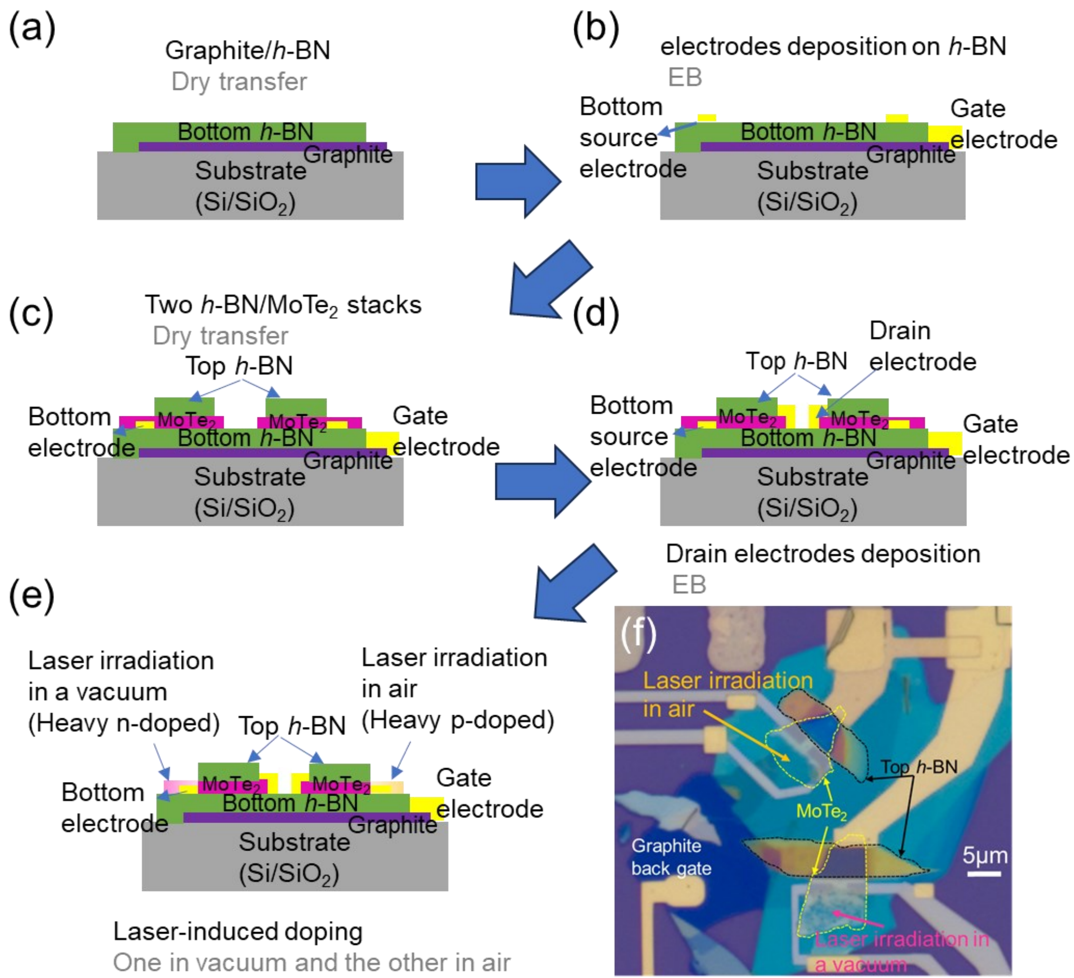

Fig. 4.18 (a) ~ (e) Fabrication process flow of n- and p-$MoTe_2$ FET at the same substrate. (f) Optical image of the sample.

Figure 4.18 (f) shows the optical image of the sample after laser irradiation. Here, the doping levels under these two conditions were confirmed by measuring their I_d-V_g curves, as shown in **Fig. 4.19**. The current in the n-doped region exhibited negligible dependence on the gate voltage, signifying that the Fermi level resided above the conduction band of $MoTe_2$, indicative of a high doping level. Furthermore, within the p-doped region, the threshold voltage appeared notably positive, confirming the successful heavy p-doping of the crystal. The p-type doping arises from the rapid and substantial absorption of oxygen molecules into vacancies induced by laser irradiation. However, it is noteworthy that not all vacancies are filled by oxygen molecules, and the surplus vacancies create weak donor energy levels. These excessive vacancies compete

with the p-type doping introduced by oxygen molecules, resulting in an overall p-type doping level lower than the n-type doping achieved under a vacuum condition. Thus, the current dropped slightly with a positive sweeping of gate voltage.

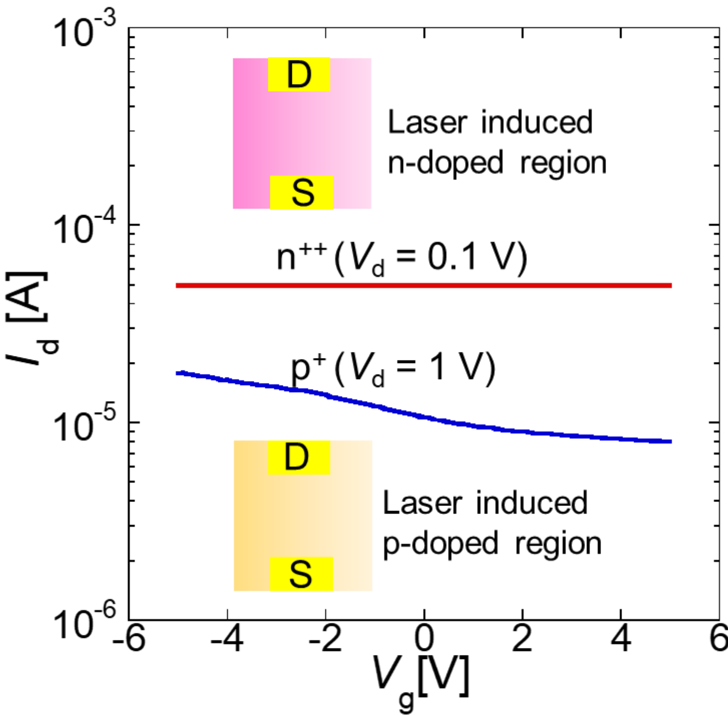

Fig. 4.19 I_d-V_g curves of the heavily n and p-doped regions.

Figure 4.20 shows the I_d-V_g curves of the n- and p-FET measured at room temperature. Both FETs exhibit a substantial on/off ratio of 10^4 under an applied drain voltage of 0.1 V. The n-FET shows a subthreshold swing value of 300 mV/dec, whereas the p-FET shows a subthreshold swing value of 1000 mV/dec. In an ideal scenario, the polarity of TMDC-FETs is primarily determined by the choice of contact metal. Specifically, when a TMDC material interfaces with a metal possessing a low work function, such as aluminum (Al) or indium (In), it tends to exhibit n-type polarity. Conversely, when the TMDC material interfaces with a metal characterized by a high work function, such as palladium (Pd) or platinum (Pt), it tends to display p-type polarity. However, in practical situations, due to inherent defects within the TMDC material and the surface damage induced by metal evaporation during contact formation, a pronounced FLP effect occurs at the contact interface. This effect presents challenges

in controlling channel polarity through the choice of different metals. In this study, polarity control was effectively achieved through contact doping via laser irradiation. On the one hand, the heavily doped contact regions with a high carrier density facilitate the efficient injection of carriers into the channel. This is attributed to the proximity of the Fermi Level of the contact regions to the conduction or valence band of the channel. On the other hand, as the metal is in contact with the heavily doped region, there is no occurrence of the FLP effect at the contact interface, and the carriers almost tunnel from the metal to the heavily doped region. The band alignment of n- and p-FET are shown as an inset graph in **Fig. 4.20**. Thus, the polarity of the channel only depends on the doping condition. In addition, owing to channel encapsulation with *h*-BN, the electron (hole) mobilities of n (p) -FET at room temperature reached 22.5 $cm^2/V{\cdot}s$ (11.2 $cm^2/V{\cdot}s$), which is higher than some previous studies [11,12].

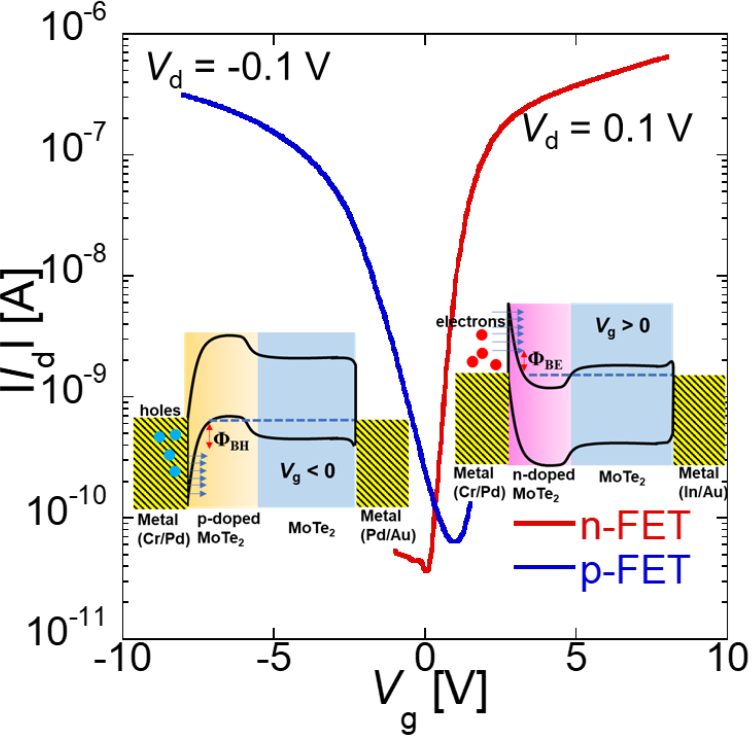

Fig. 4.20 I_d-V_g curves of n- and p-FET at room temperature.

Figure 4.21 shows the I_d-V_d curves of the n- and p-FET under different gate voltages. In both cases, saturation characteristics are observed in high drain bias regions, while

Ohmic characteristics are evident in low drain bias regions. This behavior suggests an exceedingly low Schottky barrier at the contact interface. It substantiates the enhancement of contact properties in the n- and p-FET achieved through laser-induced contact doping. Moreover, the transfer and output characteristics of both FETs are matched, making them highly suitable for implementing a CMOS inverter. However, the properties of the p-FET exhibit slight inferiority compared to the n-FET, which can be attributed to two primary factors: 1) The contact doping level in the p-FET is lower than that in the n-FET, leading to a comparatively higher contact resistance in the former; 2) Despite the channel's protection by *h*-BN, it still retains intrinsic Te vacancies. This situation caused the Fermi level to approach the conduction band, which made hole injection harder than electron injection.

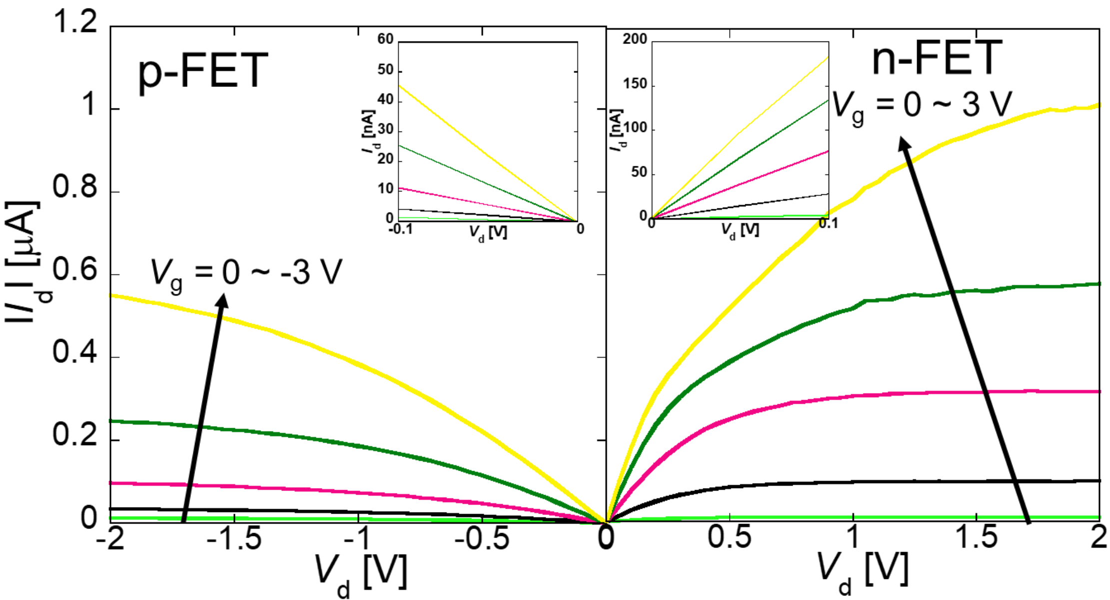

Fig. 4.21 I_d-V_d curves of n- and p-FET at room temperature.

The I_d-V_g curves of both the n-FET and p-FET were measured at various temperatures, as shown in **Figs. 4.22 (a)** and **(b)**. In comparison to room temperature, a significant reduction in the off-state current is observed at lower temperatures. However, the on-state current had only a slight decrease, resulting in a higher on/off ratio of 10^6. Given the relatively small band gap of multilayer $MoTe_2$, the off-state current in $MoTe_2$-FET is considerably reliant on ambipolar current. At lower

temperatures, the ambipolar current is substantially attenuated due to carriers lacking sufficient energy to surmount the elevated barrier associated with the ambipolar branch. This suppression of ambipolar current leads to a reduction in the off-state current.

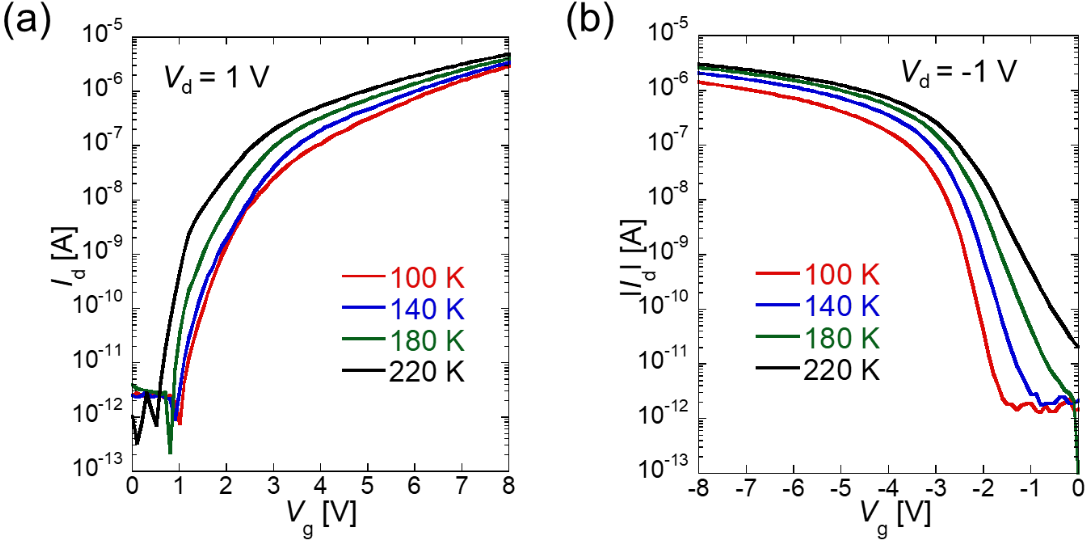

Fig. 4.22 I_d-V_g curves of n- (a) and p-FET (b) at different temperatures.

Notably, both the n-FET and p-FET exhibit evident temperature-dependent behavior in terms of current. Hence, the Schottky barrier can be estimated using the thermionic equations. In the n-FET, the extracted effective barrier height was 25 meV, whereas in the p-FET, it was 47 meV, as shown in **Figs. 4.23 (a)** and **(b)**. This notably small Schottky barrier proves the successful enhancement of contact properties achieved via our laser-induced contact doping method. The contact resistances of the n-FET and p-FET were determined using the Y-function method. The Y-function results reveal that the contact resistance of the n-FET and p-FET amounted to 0.1 MΩ·µm and 0.75 MΩ·µm, respectively, as shown in **Figs. 4.24 (a)** and **(b)**, which are lower values compared to some prior studies [13]. It is important to note that the contact resistance extracted from the Y-function method tends to be higher than the actual value. Consequently, the true contact resistance for both FETs is expected to be less than 0.1 MΩ·µm and 0.75 MΩ·µm. However, compared to the n-FET, both the Schottky barrier

and contact resistance of the p-FET were higher, indicating the doping level in the contact region is significantly important for achieving superior contact properties.

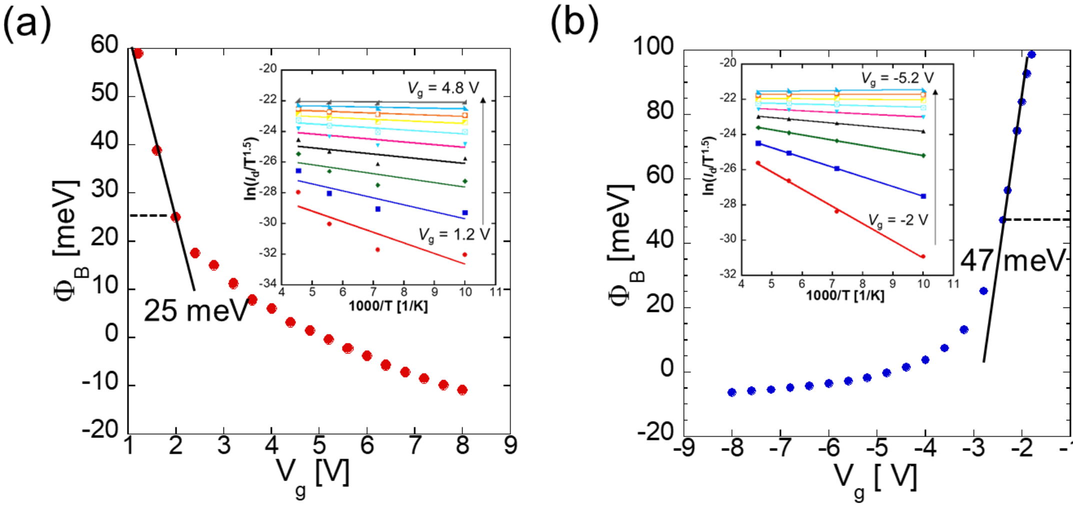

Fig. 4.23 Schottky barrier extraction of (a) n- and (b) p-FET.

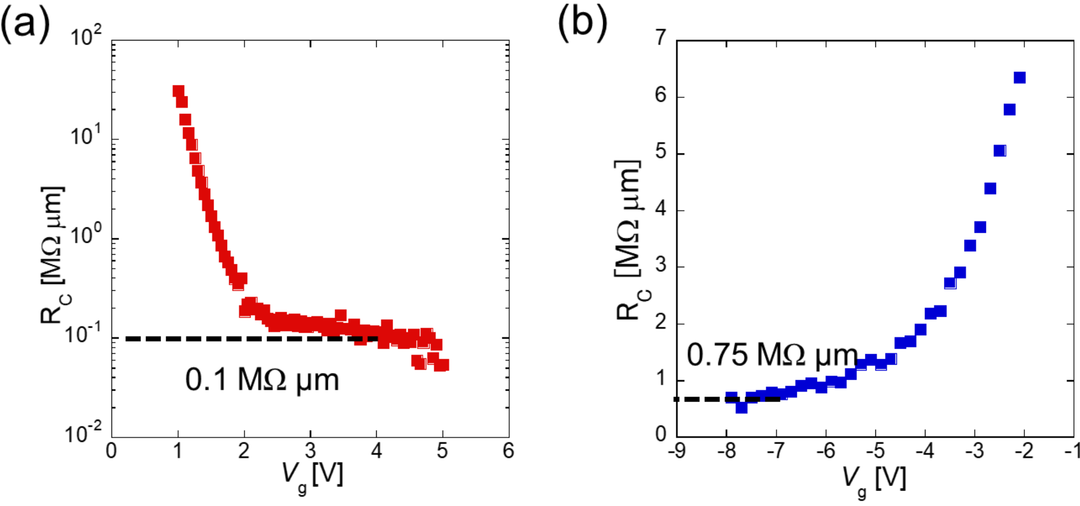

Fig. 4.24 Contact resistance calculation of (a) n- and (b) p-FET by Y-function method.

To evaluate the properties of the CMOS inverter, both n- and p-FET are controlled by the same graphite back gate that acts as the input voltage (V_{in}) electrode. The source of n-FET was grounded, and the supply voltage (V_{dd}) was applied to the source of p-

FET. Output voltage (V_{out}) was measured by the common drain electrodes. **Figure 4.25 (a)** shows the voltage transfer characteristics (VTC) of the CMOS inverter as a function of V_{dd} from 1 V to 4 V with a step of 1 V. Clean signal inversions are observed in each VTC curve, and the transition voltages are located near $V_{dd}/2$, especially at V_{dd} = 2 V. **Figure 4.25 (b)** depicts the gain values (dV_{out}/dV_{in}) corresponding to each V_{dd} level. The inverter exhibits maximum gain values of 4.7, 12.5, 23.5, and 31 at V_{dd} ranging from 1V to 4V, respectively, which is higher than the previous $MoTe_2$-based CMOS inverter [12]. The favorable inverter characteristics are attributed to the optimization of contact doping and channel encapsulation for both the n- and p-FETs.

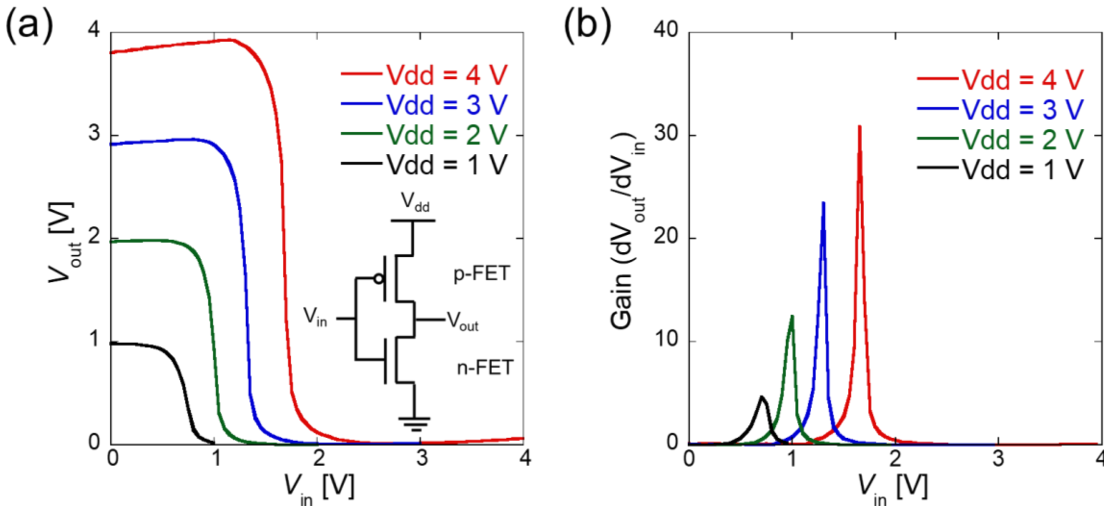

Fig. 4.25 (a)Transfer characteristics (V_{out}-V_{in}) of CMOS inverter as a function of V_{dd}. (b) D.C. voltage gain of the CMOS inverter.

Estimating the noise margin is crucial when assessing the suitability of a CMOS inverter for use in a multi-stage logic circuit. This estimation helps gauge the level of noise a CMOS circuit can tolerate without affecting its performance. Output High Voltage (V_{OH}), Output Low Voltage (V_{OL}), Input High Voltage (V_{IH}), and Input Low Voltage (V_{IL}) were extracted from VTC curves, and the high margin (NM_H) and low margin (NM_L) values were calculated by the equations of $NM_H = V_{OH} - V_{IH}$ and $NM_L = V_{IL} - V_{OL}$. **Figure 4.26** summarizes NM_H and NM_L values, along with their ratios to V_{dd}, under each V_{dd} condition. Except for V_{dd} = 1 V, all the conditions show high NM_H

and NM_L, indicating this inverter demonstrates a robust capability to withstand noise interference.

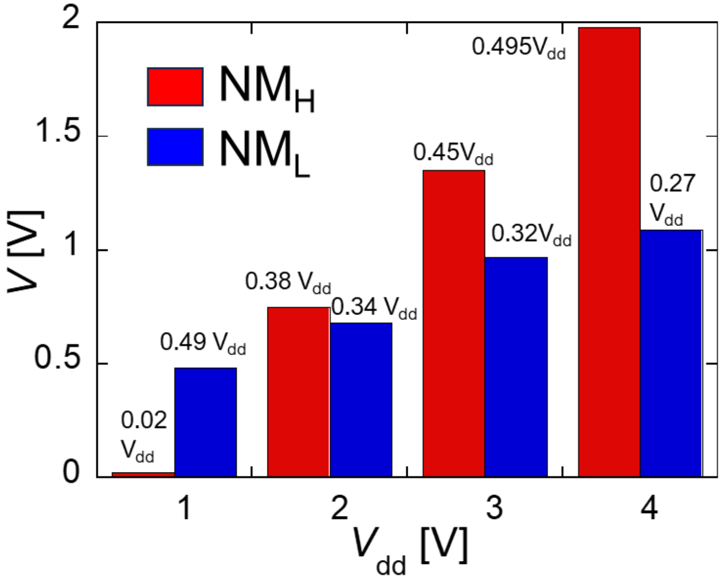

Fig. 4.26 NM_H and NM_L values of CMOS inverter at each V_{dd}.

The evaluation of the CMOS inverter's AC performance involves monitoring its dynamic behavior. **Figure 4.27** shows the input and output waveforms of the dynamic response at V_{dd}= 3 V with 1 Hz,10 Hz, 50 Hz, and 100 Hz operation frequencies. Clear inversions can be observed up to operation frequencies of 100 Hz. Unfortunately, the dynamic behavior cannot be obtained at frequencies much higher than 100 Hz. Therefore, it is necessary to improve the properties of the FET, such as reducing the *SS* value and minimizing the overlap region between the source/drain (S/D) and the gate to reduce the parasitic capacitance.

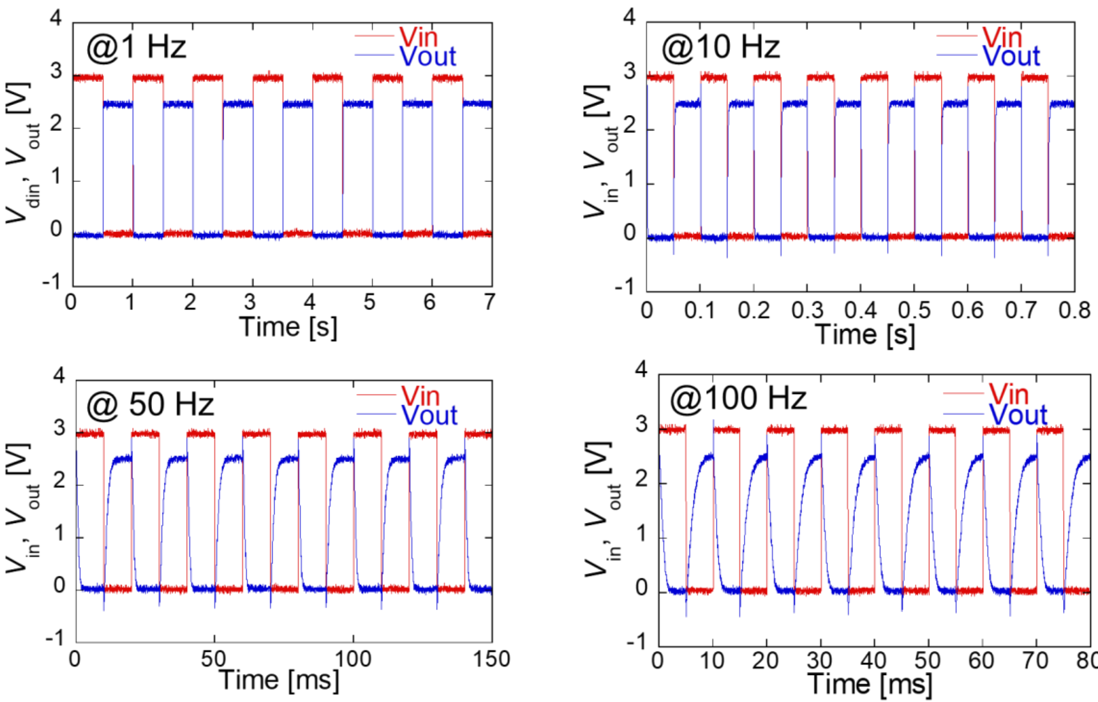

Fig. 4.27 Input and output waveforms of the dynamic response at V_{dd} = 3 V with 1 Hz, 10 Hz, 50 Hz, and 100 Hz operation frequencies.

4.4. Conclusion

This section discusses the application of laser irradiation effects on $MoTe_2$-FET, primarily focusing on improving the contact properties. Initially, laser irradiation is selectively induced at both ends of the $MoTe_2$ crystal in a vacuum environment, causing it to transform into a 1T phase with semi-metallic properties, forming a 1T/2H/1T polymorphic junction structure. Subsequently, a $MoTe_2$-FET was fabricated, with electrodes constructed on the 1T phase, thereby avoiding contact issues such as the FLP effect caused by directly depositing metal onto the semiconductor crystal. Electric measurement reveals that 1T-contacted 2H-$MoTe_2$ FET exhibits n-type dominated polarity and better contact properties compared to traditional metal-contacted FET, exhibiting Ohmic contact with a Schottky barrier of 0 meV at room temperature. In addition, the exfoliated 1T′-$MoTe_2$ also shows an excellent contact property with 2H-$MoTe_2$, which was confirmed by fabricating a 1T'/2H/1T' heterojunction structure via the dry transfer process. The 1T′-contacted 2H-$MoTe_2$ FET exhibits p-type dominated polarity and a small Schottky barrier. Besides inducing phase transition in the contact area, laser-induced contact doping is also an effective method to improve contact properties. Due to the highly doped region near the irradiated area, utilizing this region as the part in contact with the metal can reduce the width of the Schottky barrier, allowing most carriers to tunnel into the channel, thereby enhancing carrier injection efficiency and significantly reducing the effective Schottky barrier. Moreover, the contact resistance is lower by 1 to 2 orders of magnitude compared to traditional metal-contacted $MoTe_2$-FETs. Contact doping not only improves contact properties but also allows for the control of the polarity of the $MoTe_2$-FET. After heavy n-type doping of the contact area, the FET exhibits n-type dominant transfer characteristics. Conversely, after heavy p-type doping of the contact area, the FET exhibits p-type dominant transfer characteristics. Consequently, this study successfully fabricates both n- and p-channel FETs on the same substrate using the laser-induced contact doping method, with the channel region protected by *h*-BN encapsulation. Both FETs exhibit good electrical performance. Therefore, an inverter with a high gain of 32 at V_{dd} = 4 V was achieved

by combining these two FETs. In addition, this inverter demonstrates strong noise immunity and is capable of operating at a frequency of up to 100 Hz.

Reference

[1] X. Zhang, Z. Jin, L. Wang, et al. ACS applied materials & interfaces **11**, 12777 (2019).
[2] C. Kim, I. Moon, D. Lee, et al. ACS nano **11**, 1588 (2017).
[3] S. B. Mitta, M. S. Choi, A. Nipane, et al. 2D Materials **8**, 012002 (2020).
[4] A. Ruotolo, C. Y. Lam, W. F. Cheng, et al. Phys. Rev. B, **76**, 075122 (2007).
[5] M. W. Iqbal, A. Amin, M. A. Kamran, et al. Superlattices and Microstructures **135**,106247 (2019).
[6] M. W. Iqbal, E. Elahi, A. Amin, et al. Superlattices and Microstructures **137**, 106350 (2020).
[7] D. Qu, X. Liu, M. Huang, et al. Advanced Materials **29**, 1606433 (2017).
[8] S. Yang, G. Lee, J. Kim, ACS Applied Materials & Interfaces **13**, 955 (2020).
[9] M. Yamamoto, S. Nakaharai, K. Ueno, et al. Nano letters **16**, 2720 (2016).
[10] Y. Hu, G. Li, Z. Chen. IEEE Electron Device Letters **39**, 276 (2017).
[11] W. R. Choi, J. H. Hong, Y. G. You, et al. Applied Physics Letters **119** (2021).
[12] Y. J. Park, A. K. Katiyar, A. T. Hoang, et al. Small **15**, 1901772 (2019).
[13] J. Kim, A. Venkatesan, H. Kim, et al. Advanced Science **8**, 2100102 (2021).

5. $MoTe_2$-TFET fabrication via laser-induced doping

2D-TFET has great potential for applications in low-power devices, and in recent years, TFETs with excellent performance based on various 2D materials have been reported successively. However, the development of 2D-TFETs is hindered by limitations in doping techniques for 2D materials. This study achieved controllable and selective heavy doping of $MoTe_2$ crystals through laser irradiation, enabling the preparation of TFETs based on $MoTe_2$. This section mainly introduces various $MoTe_2$-TFETs fabrication using laser-induced doping techniques, including different structures such as lateral homojunction (in-plane) and vertical heterojunction (out-of-plane). Due to the difficulty in heavy n-type doping for 2D material, there are few reports related to the fabrication of p-type 2D-TFETs. This study has realized high-performance p-channel TFETs, which are of significant importance for applying 2D materials in the TFETs field. In the fabrication of TFETs, *h*-BN is often used as the device substrate and gate-insulating layer, while graphene or graphite is frequently employed as the globe back gate. Compared to SiO_2, heat is more easily dissipated through *h*-BN; thus, when performing laser irradiation on $MoTe_2$ situated on top of *h*-BN, a much higher laser power, nearly 2 ~ 3 times, is required to achieve the same effect in the case of situating on SiO_2.

5.1. Out-of-plane $MoTe_2/MoS_2$ n-TFET

Out-of-plane TFETs are bilayer structures composed of two materials that charge carriers conduct longitudinally, as shown in **Fig. 1.9 (c)**. For n-TFET, heavily p-doped semiconductors serve as the source material, while n-type or intrinsic semiconductors serve as the channel directly connected to the drain electrode. According to the WKB approximation, a smaller bandgap and a larger tunneling window can increase the tunneling probability, thus enhancing the tunneling current. The multilayer $MoTe_2$ has a bandgap of only 0.88 eV, and the energy levels of the valence band are relatively shallow compared to other TMDC materials. Therefore, heavily p-doped $MoTe_2$ is highly suitable as the source material for n-TFETs. The choice of channel material is also crucial. The higher the electron affinity of the channel material, the more favorable it is to form a larger tunneling window at a small reverse bias after contacting heavily p-doped $MoTe_2$. This facilitates the tunneling of carriers, leading to a higher tunneling current. The conduction band of MoS_2 is located at around 4.2 ~ 4.4 eV (monolayer ~multilayer) from the vacuum level, which is only 0.5 ~ 0.7 eV higher than the valence band level of 4.9 eV of $MoTe_2$. This value indicates that the TFET formed by $MoTe_2/MoS_2$ vertical heterostructure can be turned on under a smaller reverse bias voltage. **Figure 5.1** illustrates the band alignment of heavily p-doped $MoTe_2$ and multilayer MoS_2 after contact and the band evolution under applied voltages.

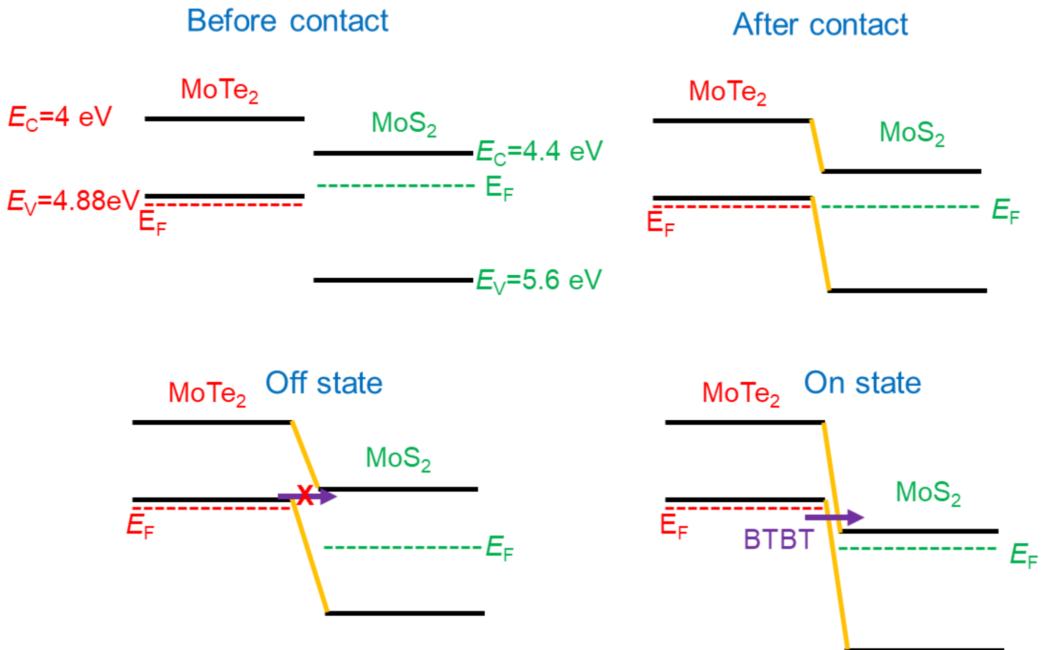

Fig. 5.1 Band alignment of heavily p-doped $MoTe_2$ and few-layer MoS_2 after contact and the evolution under applied voltages.

Figure 5.2 illustrates the optical image at each fabrication process of a TFET based on the $MoTe_2/MoS_2$ heterojunction vertical structure in this study. This TFET utilizes two *h*-BN flakes, with the one below, called the bottom *h*-BN, serving as substrate and the one above, called the top *h*-BN, serving as gate insulator.

1. A portion of the exfoliated graphite crystal was connected to the electrode pad, while another thinner portion (Bi-layer graphene) was retained as the device's drain electrode, as shown in **Fig. 5.2 (a)**.
2. A thickness of approximately 30 nm of bottom *h*-BN was placed adjacent to the graphene crystal using the dry transfer technique, replacing SiO_2 as the device substrate, as shown in **Fig. 5.2 (b)**. The advantage of using *h*-BN as the substrate lies in its smooth surface and the clean van der Waals contacts with 2D semiconductor materials, minimizing charge traps at the interface. Additionally, *h*-BN can serve as a protective layer for the bottom surface of the 2D semiconductor material.
3. Bottom electrodes were fabricated at specific locations on the bottom *h*-BN through electron beam lithography and evaporation, as shown in **Fig. 5.2 (c)**.

4. A multilayer $MoTe_2$ was placed onto the bottom *h*-BN using the dry transfer technique, ensuring contact with the bottom electrodes, as shown in **Fig. 5.2 (d)**.
5. The crystal of $MoTe_2$ near the electrodes was subjected to high-intensity laser irradiation in the atmosphere, inducing heavy p-type doping in the crystal region above the bottom electrodes, as shown in **Fig. 5.2 (e)**.
6. Picked up the top *h*-BN and then used the top *h*-BN to pick up the three-layer MoS_2 onto the bottom *h*-BN, ensuring one side contacts $MoTe_2$ and the other side contacts graphene, as shown in **Fig. 5.2 (f)**.
7. Gate metal was deposited on top of *h*-BN, covering the entire MoS_2 region, as shown in **Fig. 5.2 (g)**. The schematic diagram of the cross-section of the final sample is shown in **Fig. 5.3**.

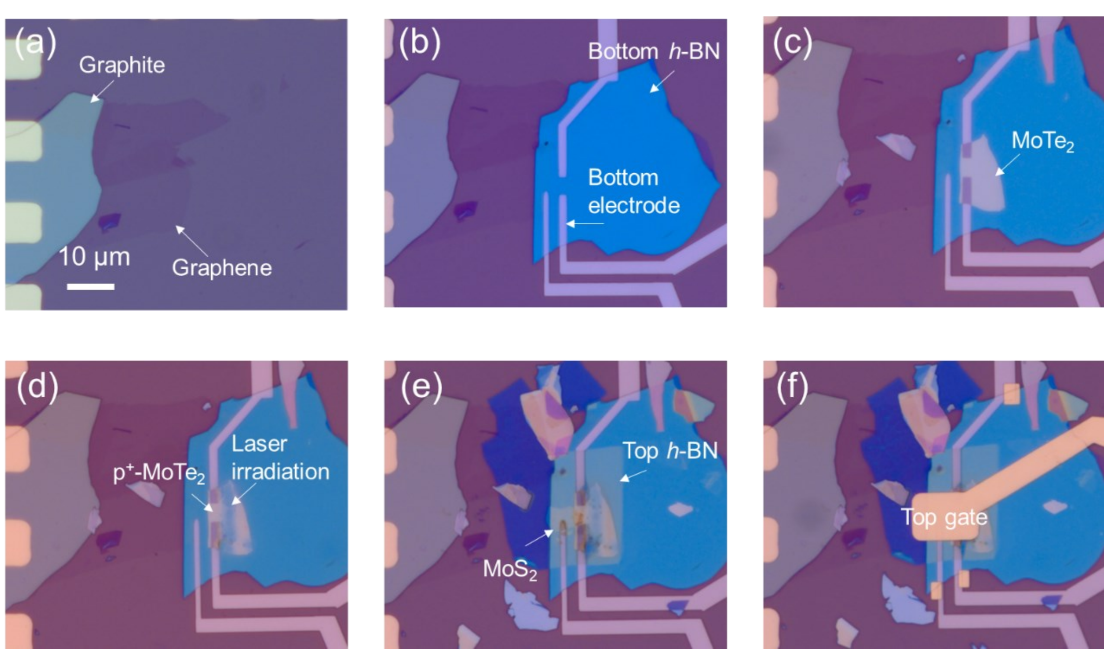

Fig. 5.2 Optical image at each $MoTe_2/MoS_2$ TFET fabrication process.

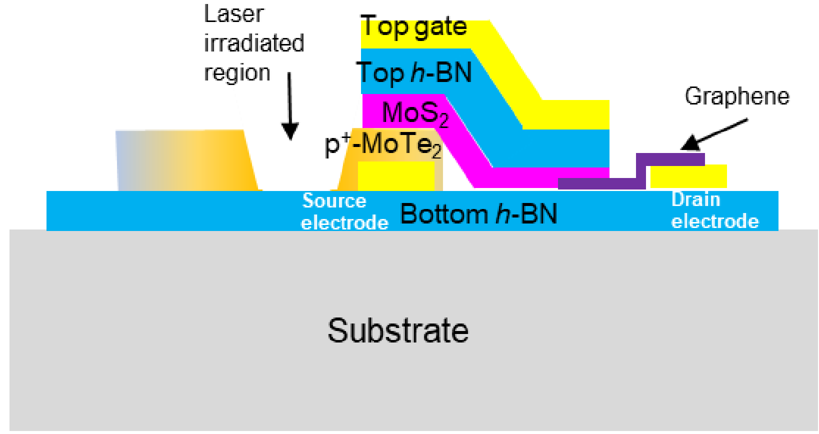

Fig. 5.3 Schematic diagram of the cross-section of $MoTe_2/MoS_2$ TFET.

The purpose of using graphene as the contact electrode for MoS_2 is to minimize the impact of the contact resistance at the drain side of the TFET. Graphene exhibits excellent conductivity, and its Fermi level is approximately located at 4.5 eV, close to the conduction band of MoS_2; thus, the Schottky barrier is very small when the two materials come into contact. Moreover, the 2D-2D contact interface is very clean, with fewer impurity levels compared to traditional metal contact, and it avoids crystalline damage caused by directly depositing metal onto the 2D semiconductor material. **Figure 5.4** illustrates the I_d-V_d curve of the MoS_2-FET with graphene as the contact electrode at room temperature. The MoS_2-FET exhibits ohmic contact behavior at a low drain voltage range, while at a high bias voltage range, the MoS_2-FET demonstrates excellent saturation characteristics. Previous reports have also indicated that graphene is well-suited as a contact material for MoS_2 [1].

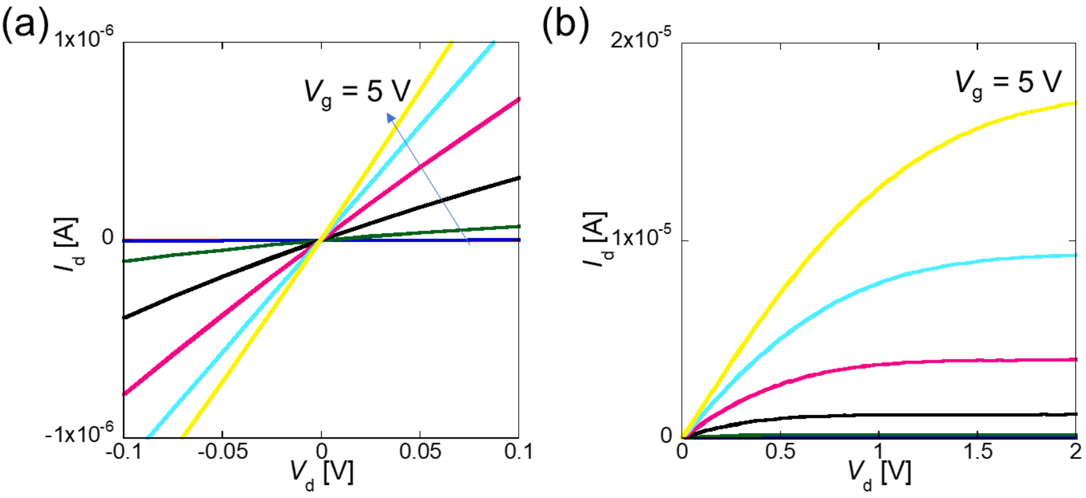

Fig. 5.4 I_d-V_d curve of the MoS_2-FET with graphene as the contact electrode.

The electrical property of $MoTe_2$ at room temperature subjected to laser-induced doping in the atmosphere is shown in **Fig. 5.5**. At a drain voltage of 1 V, the current reaches almost 0.1 milliamps, indicating that the $MoTe_2$ located on the surface of *h*-BN can also be effectually doped by laser irradiation to a high doping level. Then, the electrode in contact with $MoTe_2$ is grounded as the source terminal, while the graphene electrode in contact with MoS_2 is applied a positive voltage. This situation is equivalent to applying a reverse bias to a p/n junction. The I_d-V_g curve obtained by sweeping the gate voltage at 120 K is shown in **Fig. 5.6**, where the blue and red curves represent linear and logarithmic forms, respectively. Initially, with the increase in positive gate voltage, the current increases exponentially from picoamperes to microamperes. This indicates that the application of drain voltage and positive gate voltage changes the band alignment from type II to type III, gradually forming a larger tunneling window and a thin tunneling barrier width. A large number of electrons tunnel from the valence band of heavily p-doped $MoTe_2$ to the conduction band of MoS_2, then flow into the graphene drain electrode. The V_{th} of this n-channel TFET is 3.2V, with a high on-off ratio of nearly 10^7 and an average *SS* value of 300 mV/dec. An extremely steep *SS* value (< 60 mV/dec) is an important indicator of TFET performance, however, the gate-insulating layer used in this experiment is *h*-BN with a low dielectric constant (~3.9), a thickness of 30 nm corresponds to an EOT of 30; thus, achieving an *SS* value of 300

mV/dec under such high EOT conditions is quite good, demonstrating the advantage of using heavily p-doped $MoTe_2$ as the source material for n-TFET fabrication.

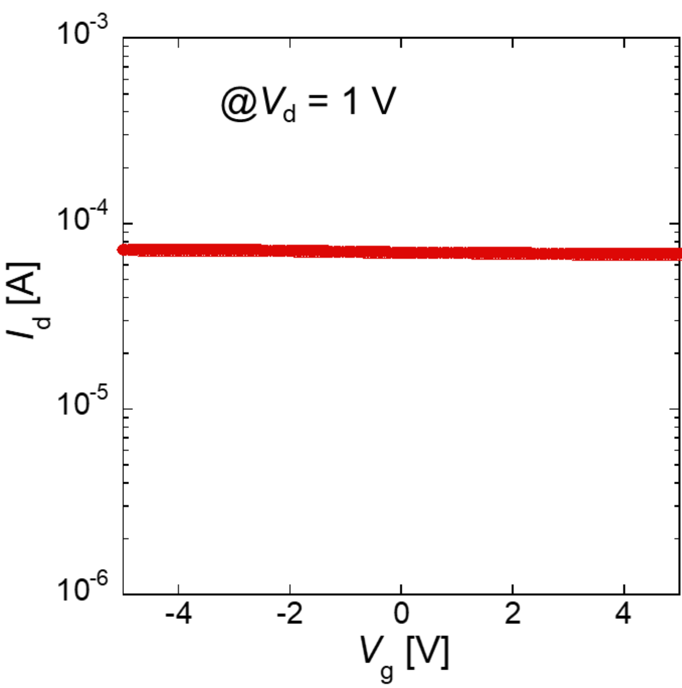

Fig. 5.5 I_d-V_g curve of the $MoTe_2$-FET on *h*-BN after laser-induced doping.

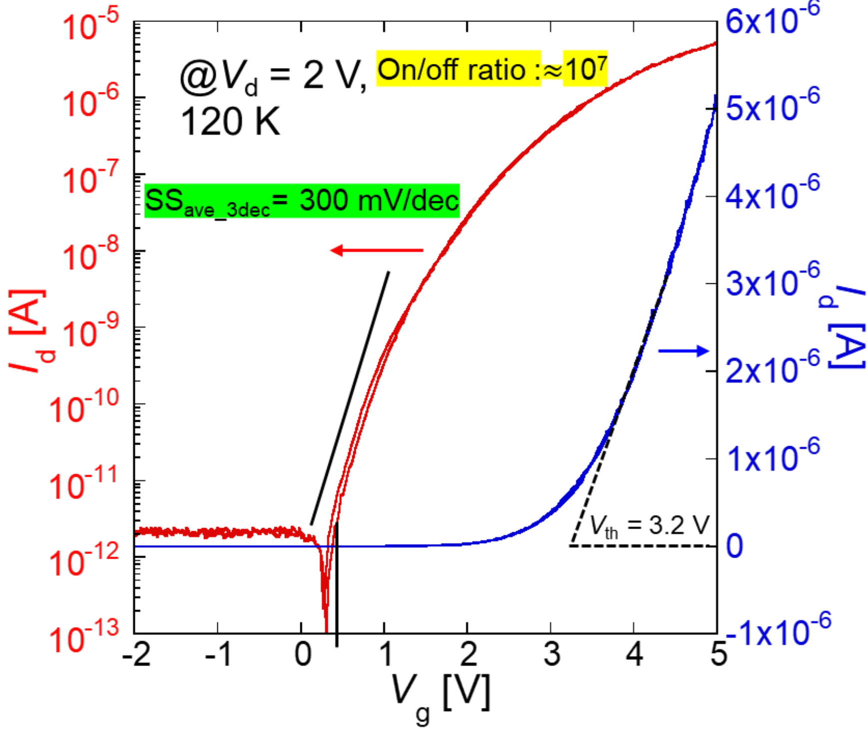

Fig. 5.6 I_d-V_g curve of the $MoTe_2$/MoS_2 TFET.

Figure 5.7 (a) shows the I_d-V_d curve of the sample at 120 K. The left portion of the I_d-V_d curve represents the forward bias region, where the current is dominated by the thermal diffusion mechanism. Here, the applied forward bias voltage reduces the built-in electric field of the p/n junction, causing electrons to flow from MoS_2 to $MoTe_2$ while holes flow from $MoTe_2$ to MoS_2, resulting in a strong diffusion current. The right portion of the I_d-V_d curve represents the reverse bias region, where the current is dominated by the BTBT mechanism. Applying reverse bias voltage enlarges the tunneling window, allowing electrons from the valence band of $MoTe_2$ to tunnel into the conduction band of MoS_2 and subsequently flow into the graphene electrode. As observed from the linear curve, the tunneling current is several times smaller than the thermal diffusion current due to the limitations in tunneling probability. The inset graph shows the logarithmic form of the I_d-V_d curve, revealing that the tunneling current exhibits a clear dependency on the gate voltage compared to the diffusion current. Applying positive gate voltage reduces the width of the tunneling barrier, thereby increasing the tunneling probability. In the case of the diffusion current, the increase in gate voltage within this range (0 ~ 5 V) has a minor effect on carrier concentration, hence no significant change in current. **Figure 5.7 (b)** magnifies the I_d-V_d curve in liner form dominated by the BTBT mechanism at the reverse bias region. It can be observed that at low reverse bias voltages, the tunneling current is almost zero, suggesting that the tunneling window requires sufficient voltage to open. In the high reverse bias region, the tunneling current exhibits significant saturation characteristics, indicating that it no longer influences the tunneling probability of electrons beyond a certain extent of tunneling window enlargement. At this moment, the tunneling probability is solely regulated by the width of the tunneling barrier, which is controlled by the gate voltage.

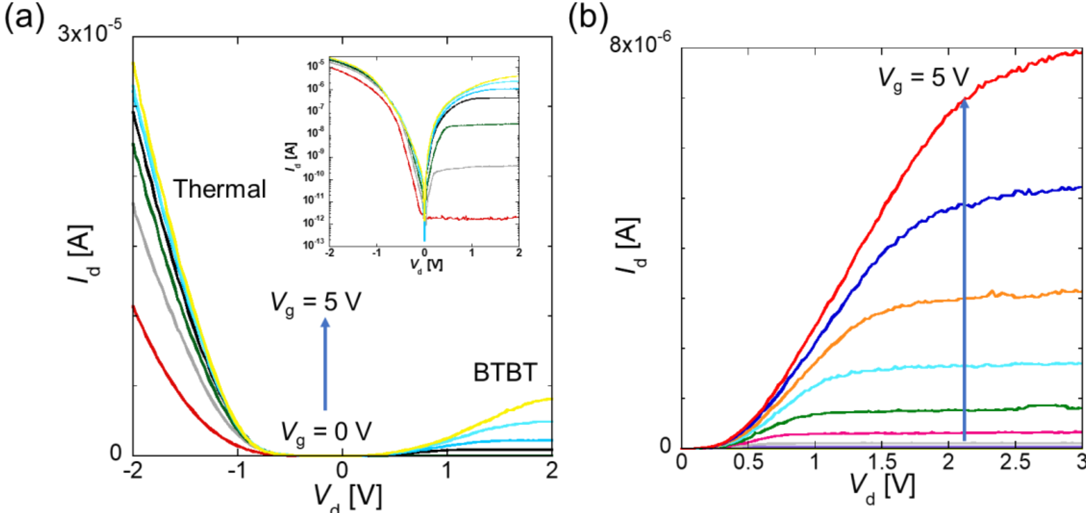

Fig. 5.7 (a) I_d-V_d curve of the $MoTe_2/MoS_2$ TFET, inset figure shows the logarithmic form. (b) I_d-V_d curve in liner form dominated by the BTBT mechanism at the reverse bias region.

Figure 5.8 shows the I_d-V_d curves at different temperatures when V_g = 4 V. In comparison to the thermal diffusion current, the tunneling current under reverse bias is barely affected by temperature, consistent with the characteristics of the BTBT conduction mechanism. Under ideal conditions, the current flowing in the TFET is solely determined by the tunneling probability, with the formula for calculating the tunneling probability not incorporating temperature parameters. However, under non-ideal conditions, the impact of barriers at the drain side and traps at the tunneling interface can lead to a certain degree of temperature dependence on the current. Therefore, the minor temperature dependence observed in the $MoTe_2/MoS_2$ TFET fabricated in this study can be attributed to the clean tunneling interface and the use of a graphene drain electrode.

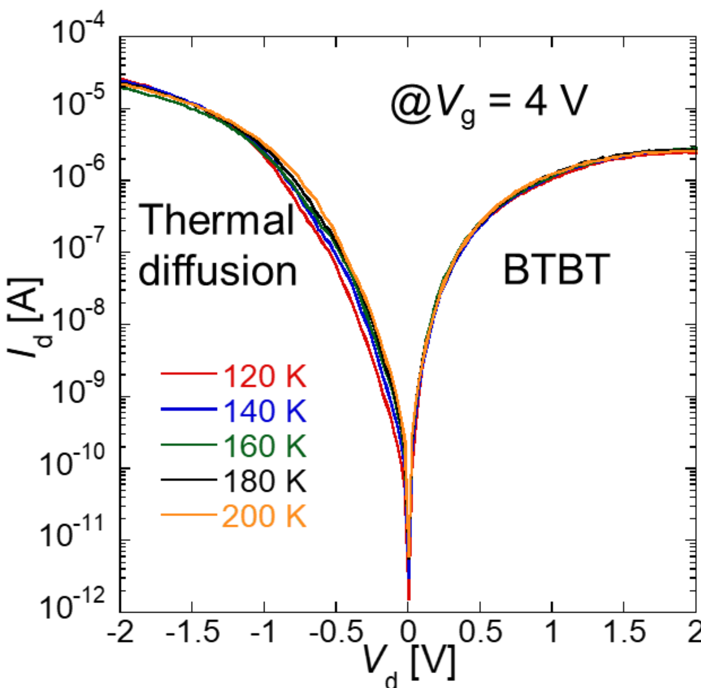

Fig. 5.8 I_d-V_d curves of the $MoTe_2/MoS_2$ TFET at different temperatures when $V_g = 4$ V.

5.2. In-plane $MoTe_2$ n-TFET

Although out-of-plane structures offer advantages such as larger tunneling areas and cleaner tunneling interfaces, their complexity arises from the requirement for two different materials, making the integration process difficult at large scales. In contrast, in-plane TFETs based on a single material have the advantage of simpler integration processes. The limited research on in-plane TFETs based on 2D materials is due to the lack of controllable and region-selective doping techniques. However, the laser-induced doping discovered in this study possesses these characteristics and can be utilized in the fabrication process of in-plane 2D-TFETs. This section and subsequent sections will discuss various in-plane $MoTe_2$-TFETs fabricated using laser-induced doping techniques. This section specifically discusses the realization of n-channel $MoTe_2$-TFET. **Figure 5.9** depicts optical images of the sample at each process for in-plane n-channel $MoTe_2$ -TFET fabrication. The fabrication steps are as follows:

1. The graphite/*h*-BN heterostructure was prepared in the center position of the pre-fabricated metal pad using the dry transfer technique. Here, *h*-BN serves as the substrate and gate insulator for $MoTe_2$, while graphite is used as the globe back gate, as shown in **Fig. 5.9 (a)**.
2. Two bottom electrodes were prepared on the surface of *h*-BN to serve as the source electrodes for the TFET operation. Subsequently, the *h*-BN/$MoTe_2$ stack was placed on the bottom *h*-BN using the dry transfer technique. Only the middle portion of $MoTe_2$ was encapsulated by *h*-BN to serve as the channel, with one side contacting the pre-prepared source electrode and ensuring enough extra crystal for laser irradiation; the other side was exposed for contact with the drain electrode, as shown in **Fig. 5.9 (b)**.
3. The drain electrode was fabricated, and all electrodes were connected to metal pads, as shown in **Fig. 5.9 (c)**.
4. Laser irradiation was applied to the crystal region near the source electrode of $MoTe_2$ in the atmosphere, causing the crystal above the electrode to be heavily p-

doped, as shown in **Fig. 5.9 (d)**. **Figure 5.9 (e)** illustrates the 3D schematic of the TFET with a p/i structure.

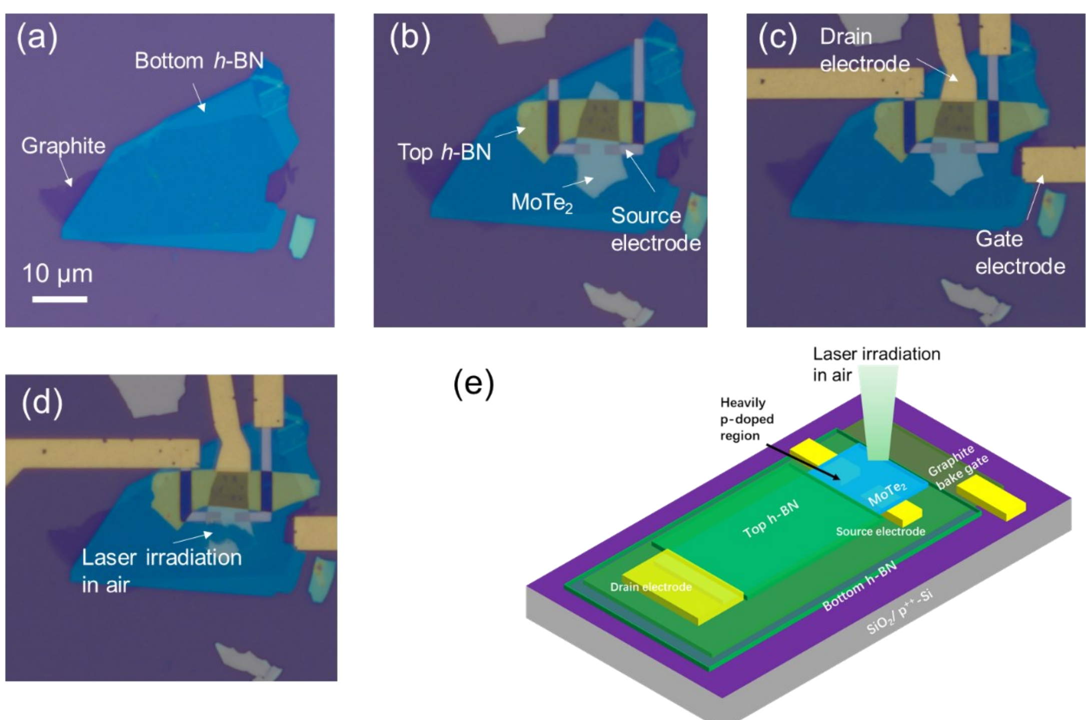

Fig. 5.9 (a) ~ (d) Optical images of the sample at each process. (e) 3D schematic of the in-plane TFET sample with a p/i structure.

The electrical property of $MoTe_2$ after laser-induced doping was confirmed, as shown in **Fig. 5.10**. The I_d-V_g curves at different temperatures show the current level reaches 0.1 milliamps at a drain voltage of 1V, similar to the previous sample. This suggests a high carrier concentration, indicating that laser irradiation achieved a high doping level. Moreover, this doping level remained stable even at low temperatures and showed no significant changes with temperature variation. Due to the current varying slightly with the gate voltage, the Fermi level is extremely close to the valence band, so it can be considered a p^+-$MoTe_2$.

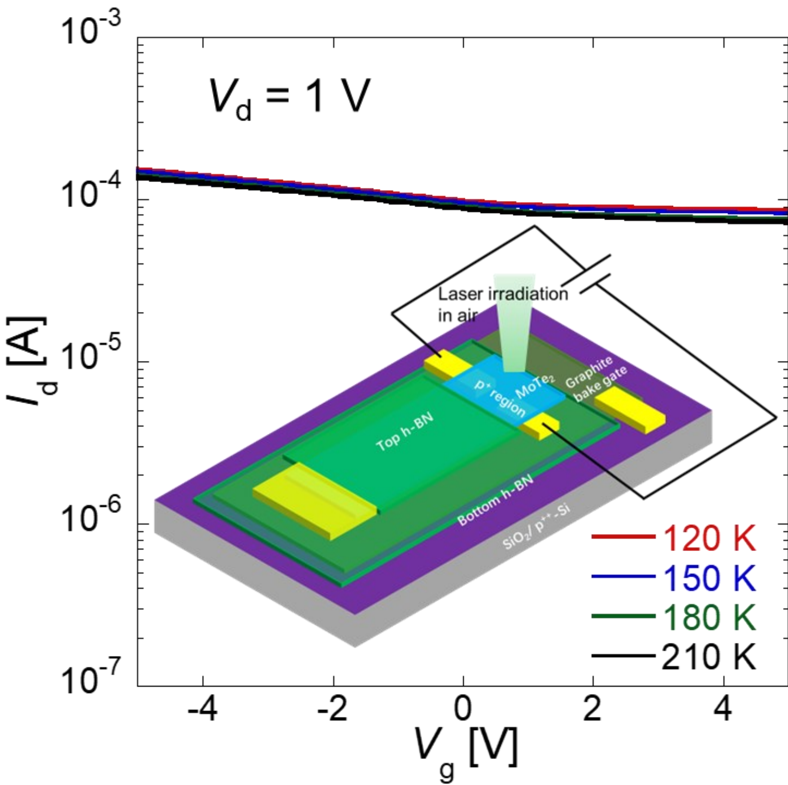

Fig. 5.10 I_d-V_g curves of the heavily p-doped $MoTe_2$ at different temperatures.

Figure 5.11 illustrates the I_d-V_g curve of the in-plane TFET structure at 120 K, with the doped region serving as the source and the *h*-BN-encapsulated region serving as the channel at a drain voltage of 1V. Upon applying a positive gate voltage, the current is generated by the BTBT mechanism. This TFET exhibits a high on/off ratio of 10^6 and a high on-state current. The region encapsulated by *h*-BN avoids the influence of laser radiation and retains its intrinsic characteristics. When a positive gate voltage is applied, it exhibits n-type polarity; thus, a lateral p/n junction is formed between the heavily p-doped crystalline region above the electrode and the *h*-BN-encapsulated crystalline region. Applying a reverse bias and positive gate voltage to this lateral p/n junction opens the tunneling window and reduces the tunneling barrier width at the p/n interface, allowing electrons to tunnel from the valence band of p-$MoTe_2$ to the conduction band of n-$MoTe_2$, generating a lateral tunneling current. The band evolution diagram is shown in **Fig. 5.12**. The p/n interface is located at the boundary between the *h*-BN-encapsulated and unencapsulated crystalline regions.

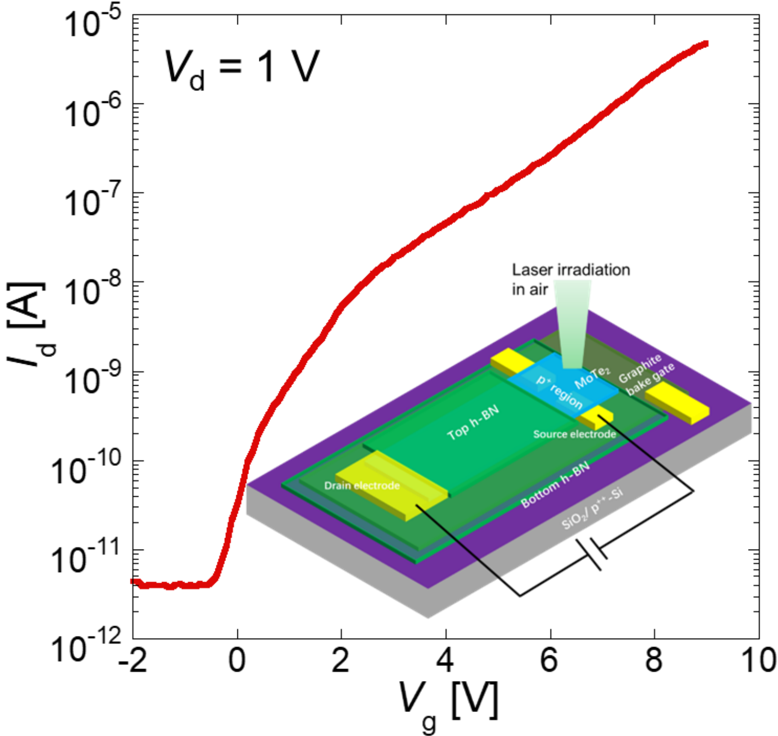

Fig. 5.11 I_d-V_g curve of the in-plane TFET AT 120 K.

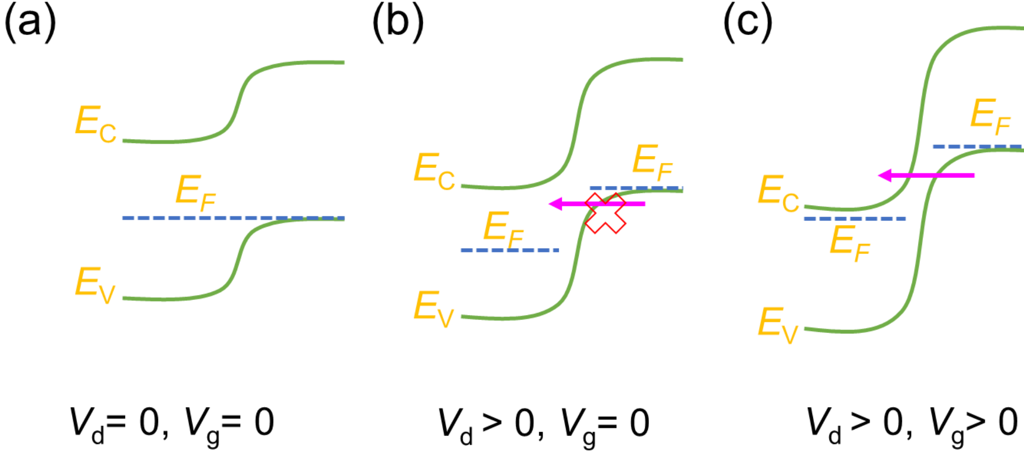

Fig. 5.12 Band evolution diagram of in-plane TFET: (a) original state. (b) off-state. (c) on-state.

5.3. Drain-doped in-plane $MoTe_2$ n-TFET

Although the operation of n-TFET has been successfully achieved by constructing a lateral p/i junction through laser-induced doping techniques, the *SS* value of the device is relatively large, which may be attributed to poor contact properties at the drain region and bubbles exist in *h*-BN/graphite interface that formed in the transfer process. Therefore, to achieve a lower *SS* value, heavy n-type doping is also performed on the drain region using laser irradiation in a vacuum environment, forming a p/i/n lateral homojunction of $MoTe_2$. The fabrication process is as follows:

1. The graphite/*h*-BN heterostructure was prepared in the center position of the prefabricated metal pad using the dry transfer technique. Here, bottom *h*-BN serves as the substrate and gate insulator for $MoTe_2$, while graphite is used as the gate electrode, as shown in **Fig. 5.13 (a)**.
2. Four bottom electrodes were prepared on the surface of bottom *h*-BN, and all the electrodes and graphite were connected to a metal pad, as shown in **Fig. 5.13 (b)**. After the lift-off process, the sample was annealed in an Ar/H_2 environment at 300 ^{o}C for 1 hour to remove organic residue on the bottom *h*-BN and bubbles existing in the *h*-BN/graphite interface.
3. A top *h*-BN/$MoTe_2$ stack was placed on the bottom *h*-BN using the dry transfer technique. Only the middle portion of $MoTe_2$ was encapsulated by *h*-BN to serve as the channel, with two sides contacting the pre-prepared bottom electrodes and ensuring enough extra crystal for laser irradiation, as shown in **Fig. 5.13 (c)**.
4. Laser irradiation in different conditions was subjected to the crystal near the bottom electrode of two sides of $MoTe_2$. This process induces heavy p-doping on one side of the crystal above the electrode and heavy n-doping on the other side, as shown in **Fig. 5.13 (d)**. **Figure 5.13 (e)** illustrates the 3D schematic of the TFET sample with a p/i/n structure.

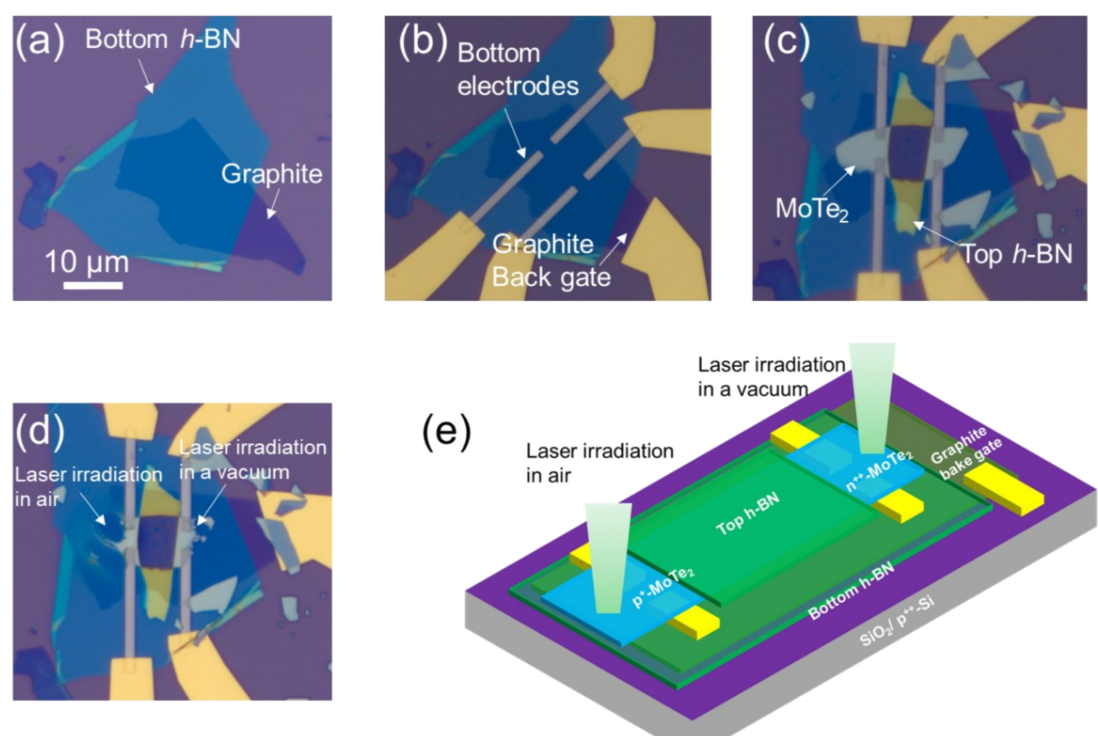

Fig. 5.13 (a) ~ (d) Optical images of the sample at each process. (e) 3D schematic of the sample with a p/i/n structure.

The electrical properties of each heavily doped region realized by laser irradiation were measured at room temperature as shown in **Fig. 5.14**. The right side of $MoTe_2$ in **Fig. 5.13 (c)** showed a n-type semiconducting transfer characteristic before laser irradiation. It was induced by the doping effect resulting from the presence of polycarbonate residue on the $MoTe_2$ surface during the transfer process. After laser irradiation in a vacuum condition for the adjacent crystal, the crystal above the bottom electrodes showed a heavily n-doped transfer characteristic; the current keeps a constant with sweeping gate voltage, as shown in **Fig. 5.14 (a)**. It can be characterized as n^{++}-doped semiconductor behavior as the Fermi level situates above the conduction band and remains unchanged with gate voltage. The large current value indicates that the laser-induced n-doping level is very high. The left side of $MoTe_2$, shown in **Fig. 5.13 (c)**, also showed a strong n-type semiconducting transfer characteristic before laser irradiation and changed to a heavily p-doped one after laser irradiation for adjacent crystal in the atmosphere as shown in **Fig. 5.14 (b)**, which aligns with the results just

stated before. **Figure 5.15** shows the I_d-V_g curves of the n^{++}-region at various temperatures. It demonstrates that the drain current remains almost independent of temperature, indicating that the stability of laser-induced n-type doping is the same as p-type doping shown in **Figure 5.10**. Thus, a $p^+/i/n^{++}$ homojunction was successfully formed by local laser irradiation in different environments.

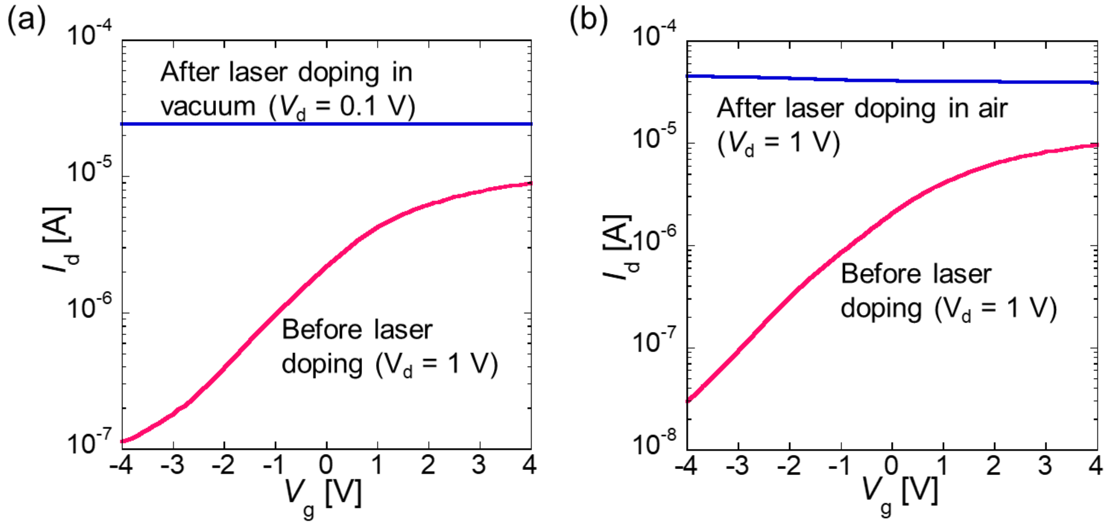

Fig. 5.14 I_d-V_g curves of the right-side region (a) and left-side region (b) of $MoTe_2$ that are shown in Fig. 5.11(c) before and after laser doping at room temperature.

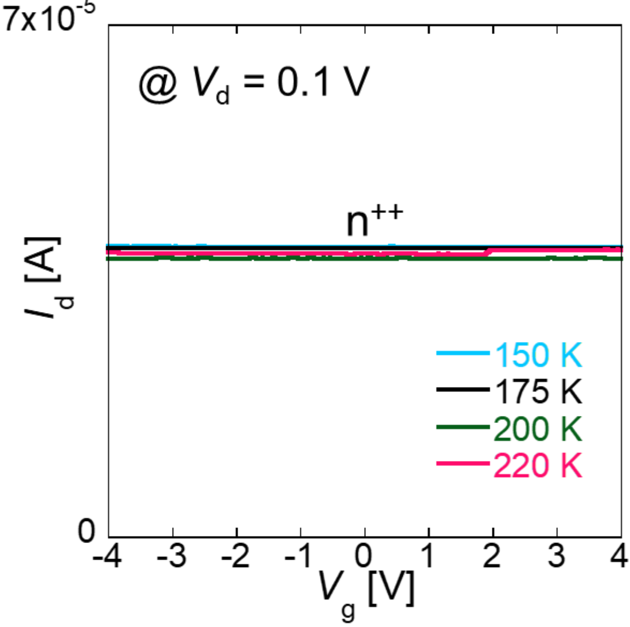

Fig. 5.15 I_d-V_g curves of the heavily n-doped $MoTe_2$ region at different temperatures.

Figure 5.16 shows the I_d-V_g curve of the $p^+/i/n^{++}$ homojunction measured at 150 K. The p^+-region was connected to the source electrode, while the n^{++}-region was connected to the drain one. Under reverse bias voltage of 1 V, the application of positive gate voltage brings the Fermi level in the channel close to the conduction band, resulting in a shift in the energy band alignment of the p^+-source and the channel from type II to type III, as shown in **Fig. 5.17 (a)**. Electrons tunnel from the valence band of the source into the conduction band of the channel, and the elevated positive gate voltage narrows the tunnel width, resulting in a significant increase in tunnel current. A small SS_{min} value of 75 mV/dec and SS_{ave} value of 230 mV/dec was obtained in this n-TFET operation. The on/off ratio is approximately 10^5, which is enough to be applied in logic circuits. However, by applying negative gate voltage at the same drain bias, the current also increased substantially. The current in the p-branch is still dominated by BTBT conduction, which is called an ambipolar state. The Fermi level in the channel gradually approaches the valence band with the application of a negative gate voltage. Simultaneously applying a reverse drain bias and a negative gate voltage induces a shift in the band alignment within the channel-drain region, transitioning it from Type II to Type III alignment. This band alignment change facilitated the electron tunneling process, with electrons tunneling from the valence band of the channel to the conduction band of the drain, as schematically depicted in **Fig. 5.17 (b)**. The ambipolar state also demonstrates a small SS_{min} value, which is attributed to the dominance of tunneling effects between the channel and drain. Furthermore, the sample is capable of operating as a thermal diffusion-dominated gated diode under forward bias conditions. Under the applied electric field, electrons and holes migrate from the n^{++}-region and p^+-region to the respective electrodes. Upon application of a positive gate voltage to the channel, the Fermi level within the channel approaches the conduction band, thereby diminishing the potential barrier for electrons and amplifying the dominance of electron current. Conversely, in the presence of a negative gate voltage, the Fermi level in the channel aligns closely with the valence band, thereby reducing the barrier for holes and augmenting the predominance of hole current, as demonstrated in **Fig. 5.17 (c)** and **Fig. 5.17 (d)**. The n-branch of the gated diode exhibits SS_{min} and SS_{ave} values of 125 mV/dec

and 450 mV/dec, respectively, which are higher than those of the TFET operation. The off-state current of the TFET is significantly smaller than that of the gated diode by two orders of magnitude. This observation provides evidence of BTBT conduction under reverse bias conditions, as the small off-state current is a distinctive characteristic of TFETs. The on-state current of the TFET is also smaller than the gated diode. The limited magnitude of the current facilitated by the tunneling mechanism predominantly arises from its close association with tunneling probability. In addition, the presence of a gradual p/i (n/i) interface within the sample contributes to an elevation in the tunneling barrier, consequently leading to a reduction in current. Ideally, the p/i (n/i) longitudinal interface is situated on either side of the top *h*-BN, but in reality, the doping levels of the $MoTe_2$ crystal undergo a gradual change at varying distances from the irradiated region. Hence, it is imperative to investigate the laser-induced p/i (n/i) interface further in the future, potentially through techniques such as scanning gate microscope (SGM) analyses [2].

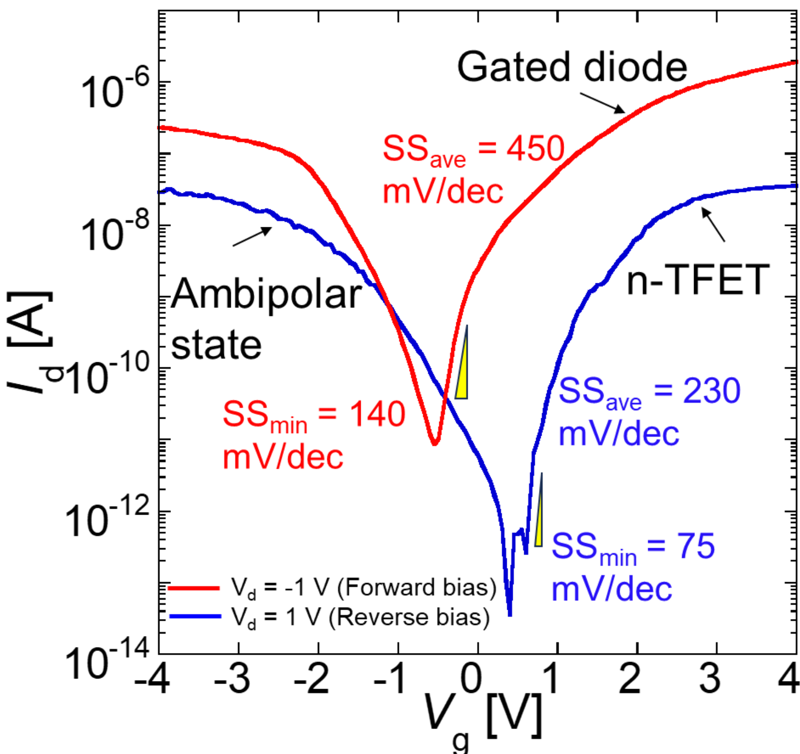

Fig. 5.16 I_d-V_g curves at 150 K of the a $p^+/i/n^{++}$ homojunction sample at reverse bias and forward bias.

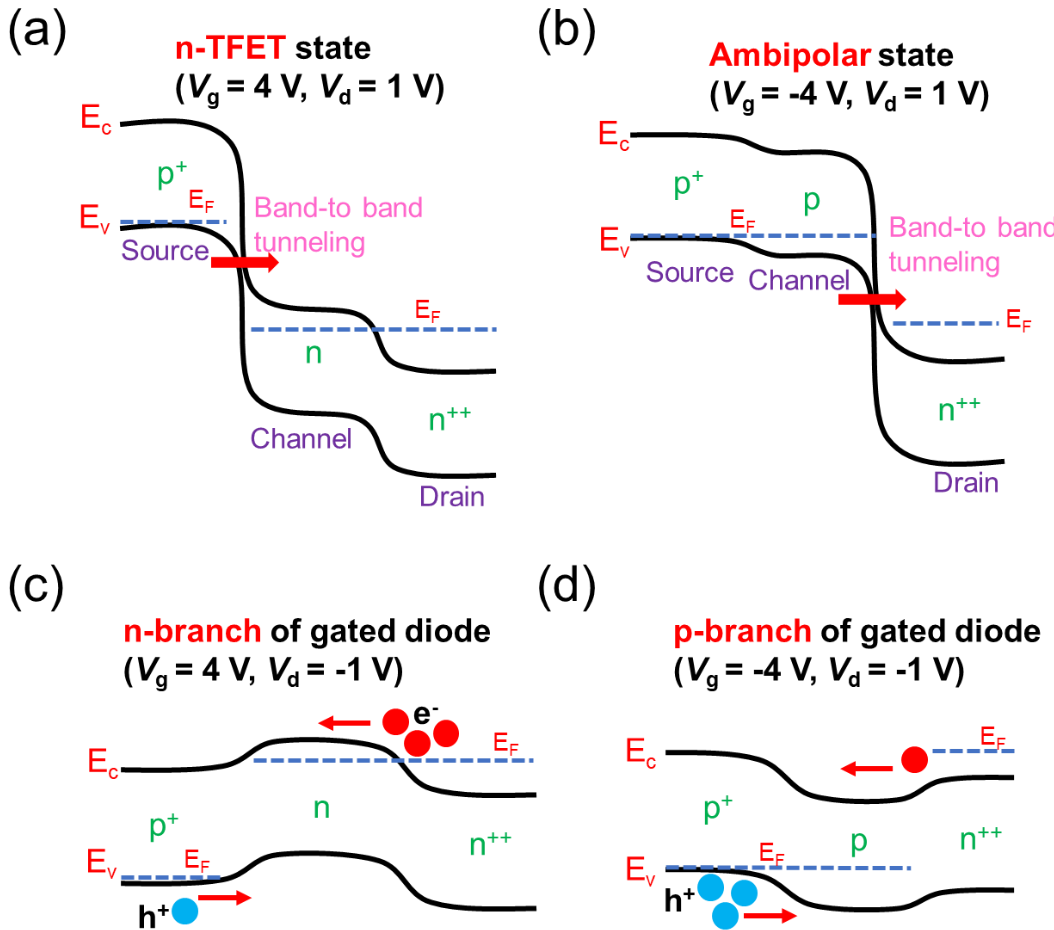

Fig. 5.17 Energy band evolution with the drain bias and gate voltage. (a): n-TFET state, (b): ambipolar state, (c): n-branch of the gated diode, (d): p-branch of the gated diode.

Figure 5.18 shows the I_d-V_g curves at various drain voltages of the n-TFET at 120 K. The *SS* value at the low current region is almost unchanged, while the on-state current significantly increases with increasing drain bias voltages. This is attributed to the elevated reverse bias voltage, causing an increase in the tunneling window and a decrease in the width of the tunneling barrier. This leads to an increased tunneling probability, consequently resulting in an augmentation of tunneling current. **Figure 5.19** depicts the I_d-V_g curves at gate voltages ranging from 0 to 4 V in 1 V increments with a linear scale and logarithmic scale (inset graph) at 120 K. The saturation characteristic of the TFET is clearly observable. The inset figure shows the diode current at forward bias voltages is larger than the tunneling current at reverse bias voltages. The absence of the negative differential resistance (NDR) region in the

forward bias is attributed to the relatively low doping concentration in our sample, which is insufficient to manifest the NDR or NDR trend [3].

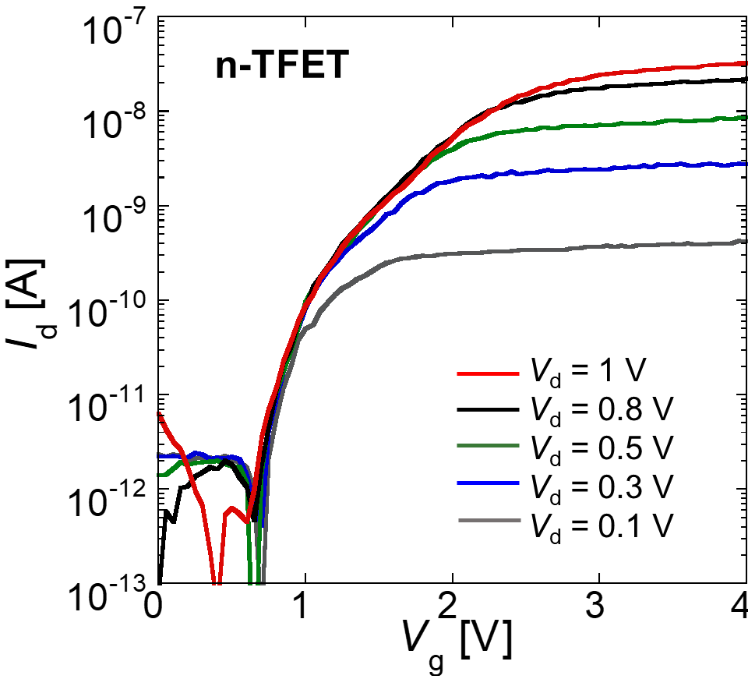

Fig. 5.18 I_d-V_g curves at different drain bias voltages of the n-TFET at 120 K.

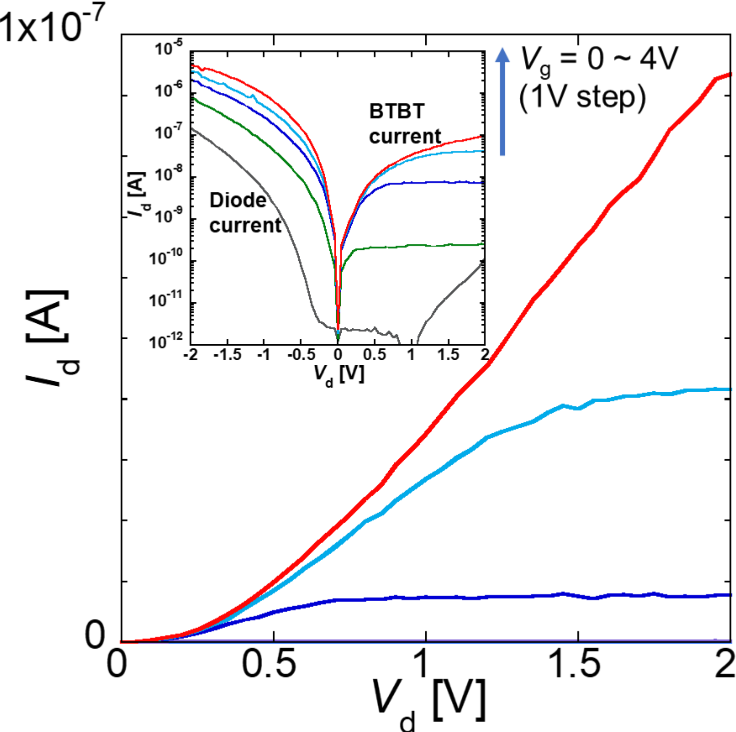

Fig. 5.19 I_d-V_d curves at different gate voltages of the n-TFET at 120 K.

Figure 5.20 (a) shows the I_d-V_g curves at different temperatures. As the temperature increased, the I_{off} and *SS* values (SS_{ave}, SS_{min}) showed a significant increase, as shown in **Fig. 5.20 (b)**. In a p/n junction diode, vacancies or impurities at the junction interface can form charge traps, which severely impact the diode's performance. Similarly, the presence of these traps also affects the performance of TFETs based on p/n junction structures operating under reverse bias. The ideality factor reflects the disparity between the actual and ideal interfaces, with values closer to 1 indicating a closer resemblance to the ideal situation. **Figure 5.21** shows the ideality factors of our p/i/n junction diode at various temperatures (V_g = 0 V). The minimum value of the ideality factors is 3.4 ~ 6.5 as the temperature decreases from 220 K to 120 K. The increase in ideality factors as temperature decreases is due to the reduction in carrier concentration at lower temperatures. Such high ideality factors suggest a highly non-ideal p/i (n/i) interface. In our case, laser-induced Te-vacancies and intrinsic vacancies in the p/i (n/i) interface can act as charge traps. For n-TFET operation at high temperatures, electrons tunnel from the valence band of the source to the conduction band of the channel through these traps via phonon interactions before undergoing BTBT, leading to trap-assisted tunneling (TAT) current [4]. The presence of TAT current has a significant impact on the characteristics of the switching region, including deterioration in the *SS* value and an increase in I_{off}. Moreover, this process exhibits strong temperature dependence and can be suppressed at low temperatures. Therefore, the steep *SS* value and small I_{off} can only be observed at low temperatures in this study.

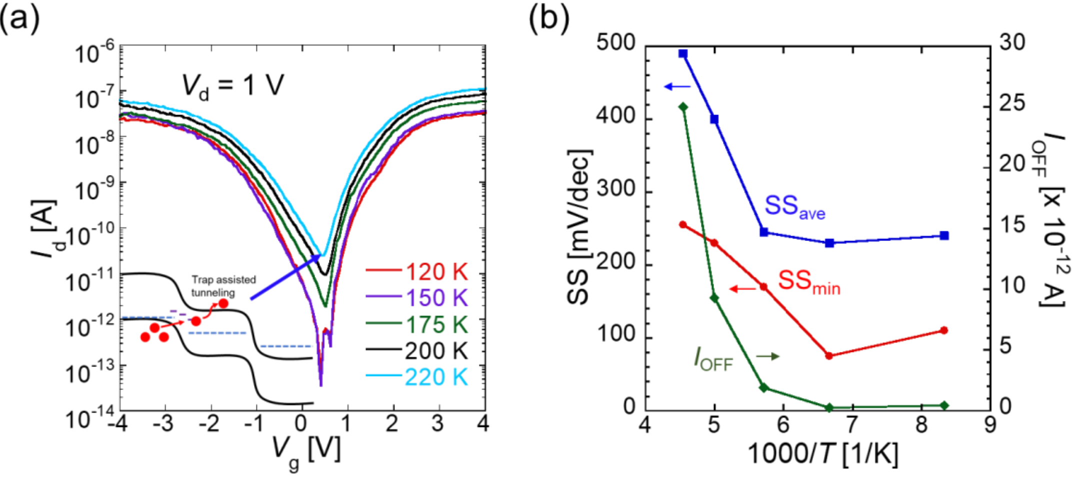

Fig. 5.20 (a) I_d-V_g curves at different temperatures. (b) Temperature dependence of *SS* value and I_{off}.

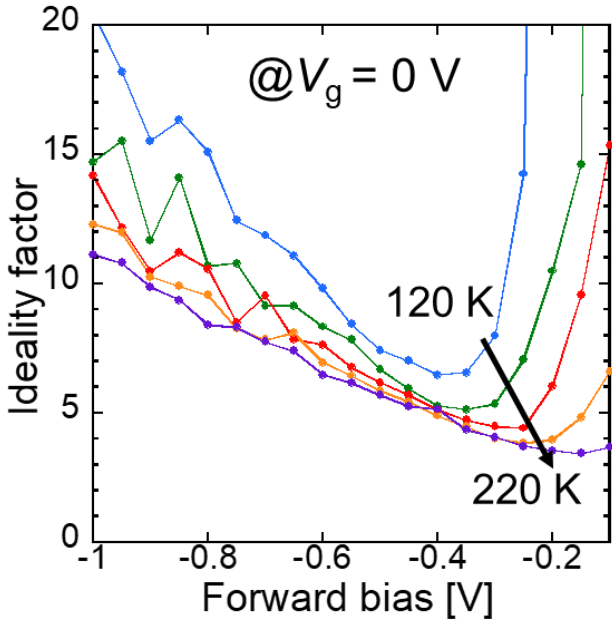

Fig. 5.21 Ideality factors of p/i/n junction diodes at various temperatures.

5.4. In-plane $MoTe_2$ p-TFET

To achieve the application of 2D-TFETs in logic devices, the implementation of p-TFETs complementary to n-TFETs is crucial. Realizing p-TFETs require heavily n-doped source materials, but due to doping technology limitations, there have been few reports on p-TFETs based on 2D materials. However, this study demonstrates that high-intensity laser irradiation on $MoTe_2$ in a vacuum environment can induce a heavily n-doped region, and this doping method is region-selective, offering the potential for p-TFET fabrication. For the p/i/n structure introduced in the previous section, utilizing the heavily n-doped region as the source and the heavily p-doped region as the drain enables p-TFET operation. Therefore, this section introduces results on p-TFET fabrication. Initially, n/i/p structures were directly fabricated on SiO_2/p^{++}-Si substrate, with a fabrication process similar to the previous sample. In this case, SiO_2 and p^{++}-Si can directly serve as the gate insulator layer and globe back gate, respectively. In addition, electrodes were added in the intrinsic part covered by *h*-BN to measure the electrical properties of n/i homojunction structure, as shown in **Fig. 5.22**.

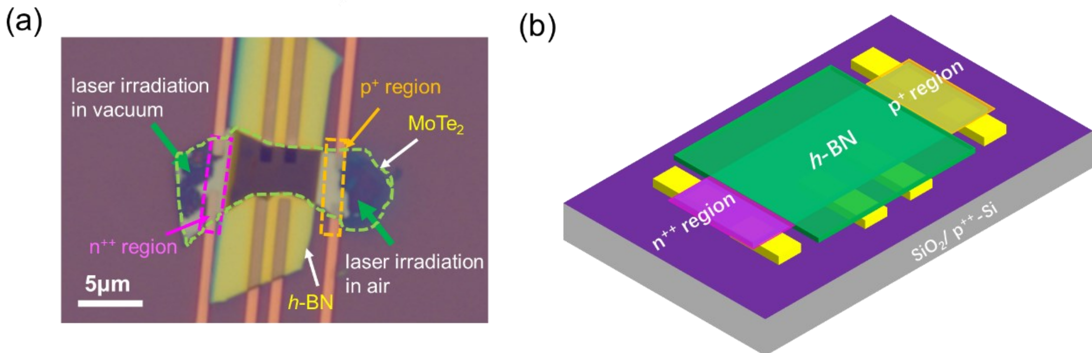

Fig. 5.22 (a) optical image and (b) 3D schematic of the p-TFET sample.

The electrical properties of the doped region were confirmed using the bottom electrodes located beneath the doped region at room temperature, as shown in **Fig. 5.23**. For the heavily n-doped region, the current reached above 4.5 microamps at a drain voltage of 0.1V, indicating a high electron concentration and strong doping level. Although the linear I_d-V_g curve shows a trend of current variation with gate voltage,

within the range of gate voltage from -60 ~ 60 V, the current change is only about three percent. Therefore, it can be inferred that the current is almost independent of the gate voltage, suggesting that the crystal has transitioned into an n-type degenerate semiconductor (n^{++}), consistent with the results presented in Chapter 3. For the heavily p-doped region, the current value at a drain voltage of 0.1V is 0.12 ~ 0.15 microamp, which is more than one order of magnitude lower than the current in the n-doped region. This suggests that the doping level in this region is lower than that of the n-doped region, which is consistent with the case when *h*-BN is used as the substrate, as mentioned before. Within the range of gate voltage up to 120 V, the current variation is about twenty percent. Due to the relatively small doping level and large current change, the Fermi level in this region remains within the bandgap but is very close to the valence band, hence referred to as p^+.

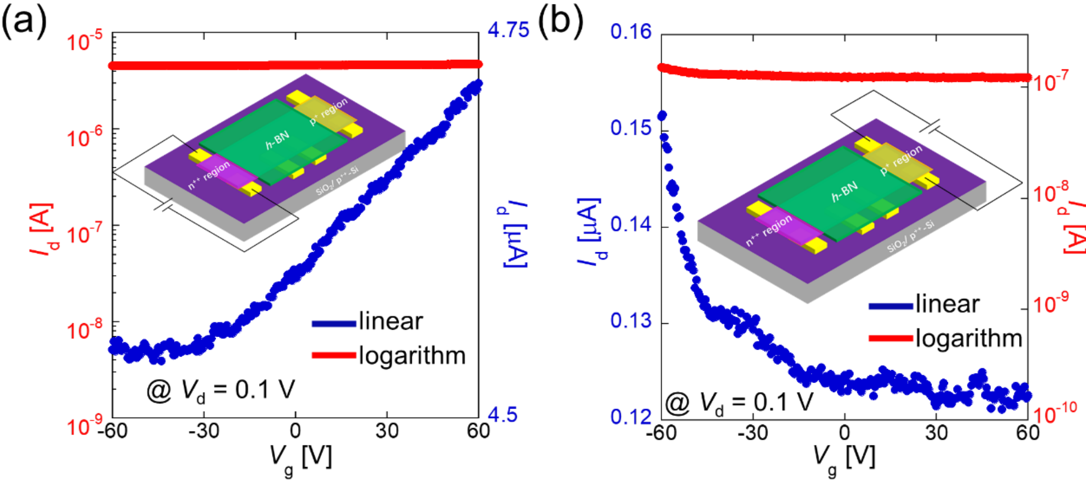

Fig. 5.23 I_d-V_g curves of the (a) heavily n-doped region and heavily n-doped region in linear and logarithmic form at room temperature.

Grounding the n^{++} region as the source and connecting the channel to the drain electrode, the I_d-V_g curve based on n^+/i homojunction was measured under a drain voltage of -2 V at 120 K, as shown in **Fig. 5.24**. This n/i homojunction successfully achieves p-TFET operation by sweeping negative gate voltages. It exhibits an on/off ratio of 10^5 and a relatively low *SS* value of 1.3 V/dec, even a 300-nm-thick SiO_2 as a

gate dielectric layer. From the linear curve, the V_{th} is observed to be -35 V. The band alignment at the on-state of this p-TFET is shown in **Fig. 5.26 (a)**, where electrons tunnel from the channel's valence band to the conduction band in the n^{++} region and then flow into the source, leaving behind holes in the valence band. These holes flow towards the drain under the electric field, forming a hole current in the channel. For the n/i/p homojunction structure, the n^{++} region also serves as the source, while the p^{+} region serves as the drain. The I_d-V_g curve was also measured under a drain voltage of -2 V at 120 K, as shown in **Fig. 5.25**. The performance of TFET based on the n/i/p structure is similar to that of the n/i structure, exhibiting an on/off ratio of 10^5 and an *SS* value of 1 V/dec. However, due to the increased channel length leading to increased channel resistance, the on-state current is slightly lower, and the V_{th} located at -45 V is higher than that of the n/i homojunction p-TFET. After applying a fixed drain voltage, due to the presence of channel resistance, the effective bias voltage applied to the tunneling interface is smaller than the drain voltage. Hence, TFETs with longer channels require a larger gate voltage to open the tunneling window and reduce the tunneling barrier under the same reverse bias. **Figure 5.26 (b)** illustrates the band alignment after the n/i/p homojunction p-TFET is turned on at a high negative gate voltage. The most significant difference from the n/i homojunction p-TFET is that the n/i/p homojunction p-TFET exhibits an increase in current when a sufficiently positive gate voltage is applied. In this situation, the channel turns into n-type, opening the tunneling window between the drain and channel, allowing electron tunneling from the valence band of the p^{+} region to the conduction band of the channel and then flowing into the source, forming a tunneling current, as shown in **Figure 5.26 (c)**. This situation is similar to the current in the p-branch of the p/i/n homojunction n-TFET, referred to as the ambipolar state of the p-TFET.

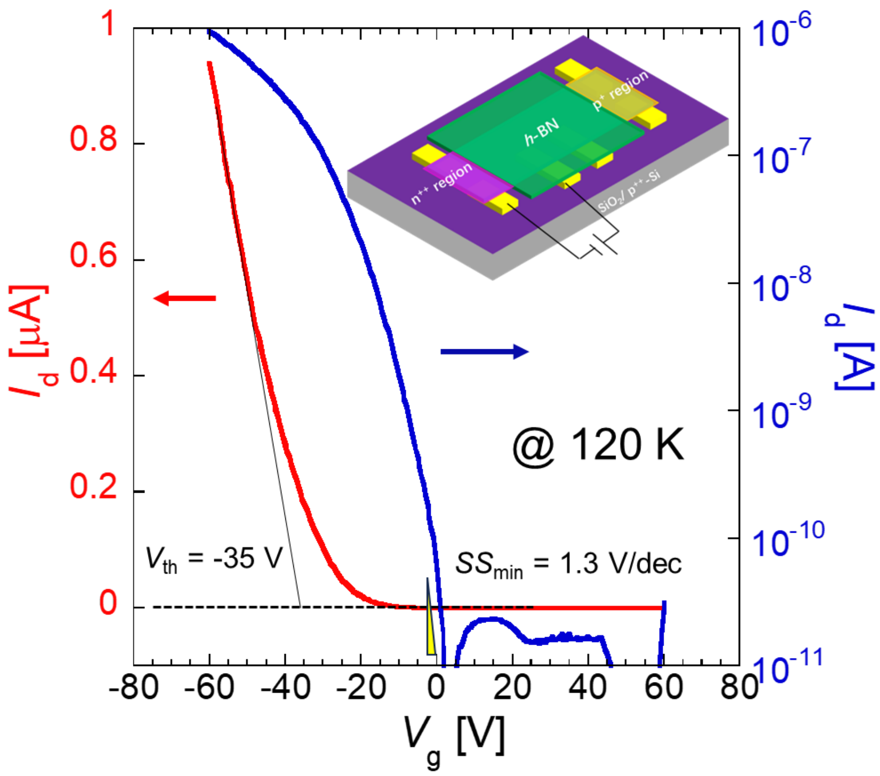

Fig. 5.24 I_d-V_g curve of the n/i homojunction p-TFET at V_d = -2 V.

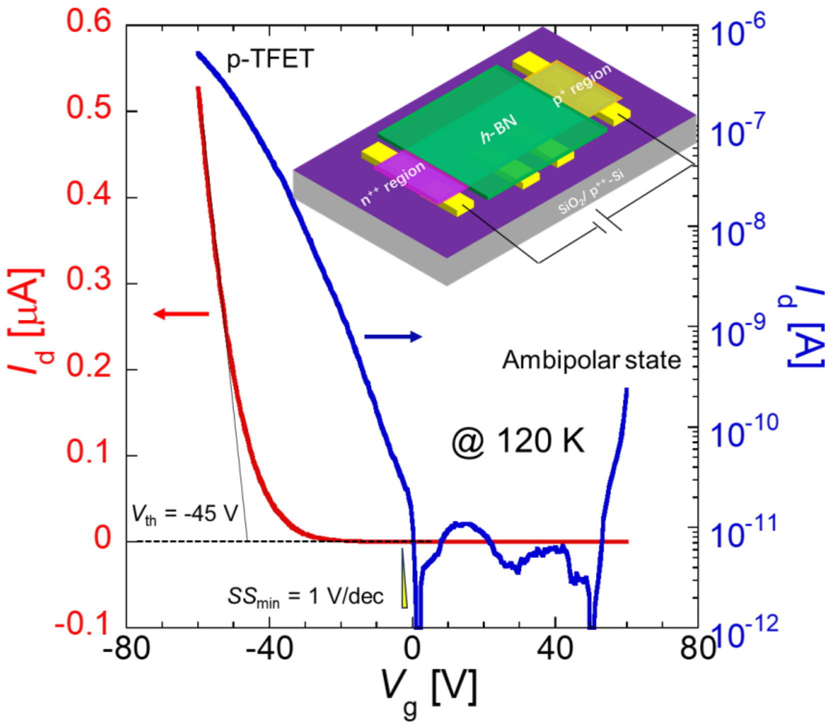

Fig. 5.25 I_d-V_g curves of the n/i/p homojunction p-TFET at V_d = -2 V.

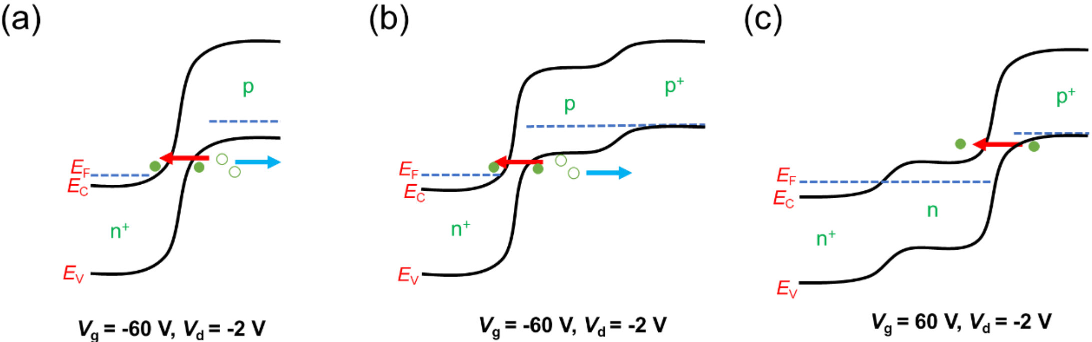

Fig. 5.26 (a) Band alignment of n/i/ homojunction p-TFET at on-state. (b) Band alignment of n/i/p homojunction p-TFET at on-state. (c) Band alignment of n/i/p homojunction p-TFET at ambipolar-state.

Figure 5.27 (a) represents the I_d-V_d curves at different negative gate voltages of the n/i homojunction p-TFET at 120 K. The negative drain voltage region represents the operating region of the TFET with the current conducted by the BTBT mechanism. The positive drain voltage region represents the diode current conducted by the thermal diffusion mechanism. It is evident that the tunneling current exhibits a more pronounced dependence on the gate voltage compared to the diode current, indicating that even with a gate structure of EOT of 300 nm, this lateral tunneling interface can still be effectively controlled by the gate voltage. **Figure 5.27 (b)** represents the linear I_d-V_d curves of BTBT conduction. After applying a certain negative drain voltage, the current initially increases linearly until reaching saturation at a certain voltage. The current in the saturation region is only influenced by the gate voltage, similar to the characteristics of a p-MOSFET.

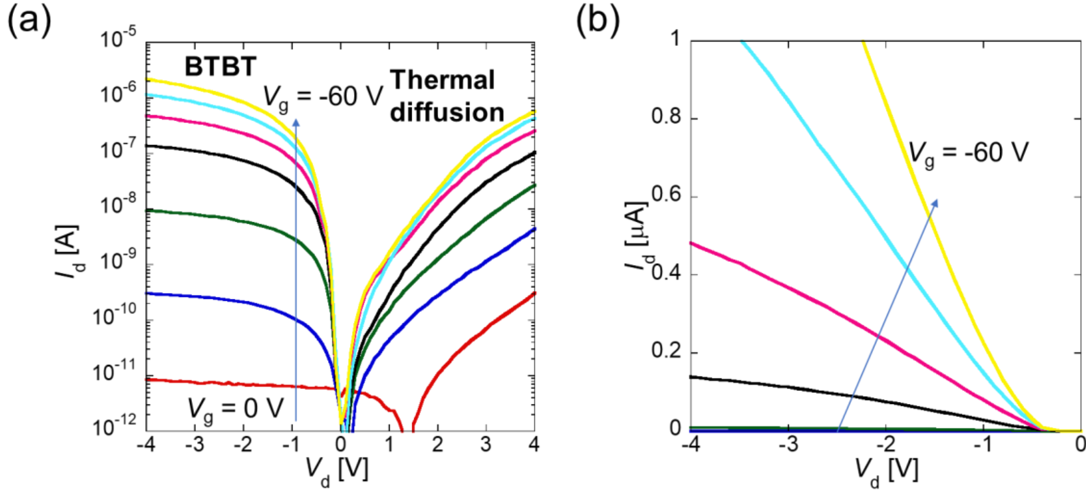

Fig. 5.27 (a) I_d-V_d curves in the logarithmic form of the n/i structure TFET at different gate voltages. (b) I_d-V_d curves of BTBT conduction in linear form.

In order to achieve a lower *SS* value, a n/i homojunction p-TFET was fabricated using *h*-BN and graphite as the gate insulating layer and globe back gate, as shown in **Fig. 5.28**. Not only the channel but also the part connecting the drain electrode was protected by *h*-BN to ensure that it would not be doped by polycarbonate during the transfer process. The exposed $MoTe_2$ crystal was subjected to laser irradiation in a vacuum environment, resulting in the heavily n-doped region above the bottom source electrodes. The density of laser irradiation in this case was smaller compared to previous ones; thus, although the crystalline in the irradiation area was damaged, there was still a crystalline residue with a large size. Raman spectroscopy measurement was conducted on the irradiation area and the doped area separately, as shown in **Fig. 5.29**. The Raman spectrum of the irradiation area shows two distinct peaks located at 151 and 240 cm^{-1}, corresponding to the characteristic peaks of 1T-$MoTe_2$, which is consistent with the results of phase transition in Chapter 3, indicating that phase transition can still occur even when *h*-BN serves as the substrate for 2H-$MoTe_2$. The Raman spectrum of the doped area only displayed characteristic peaks of the 2H structure, indicating that there was no crystalline structural change in this area.

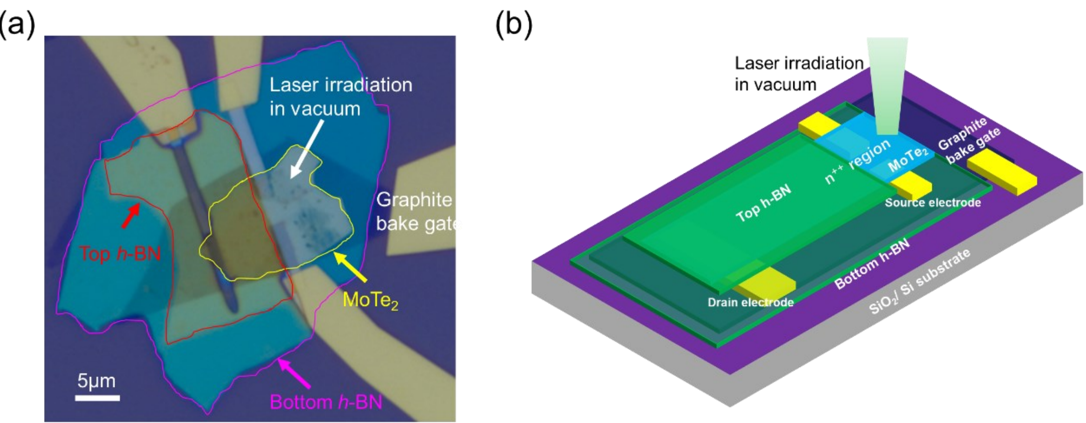

Fig. 5.28 (a) optical image and (b) 3D schematic of the sample.

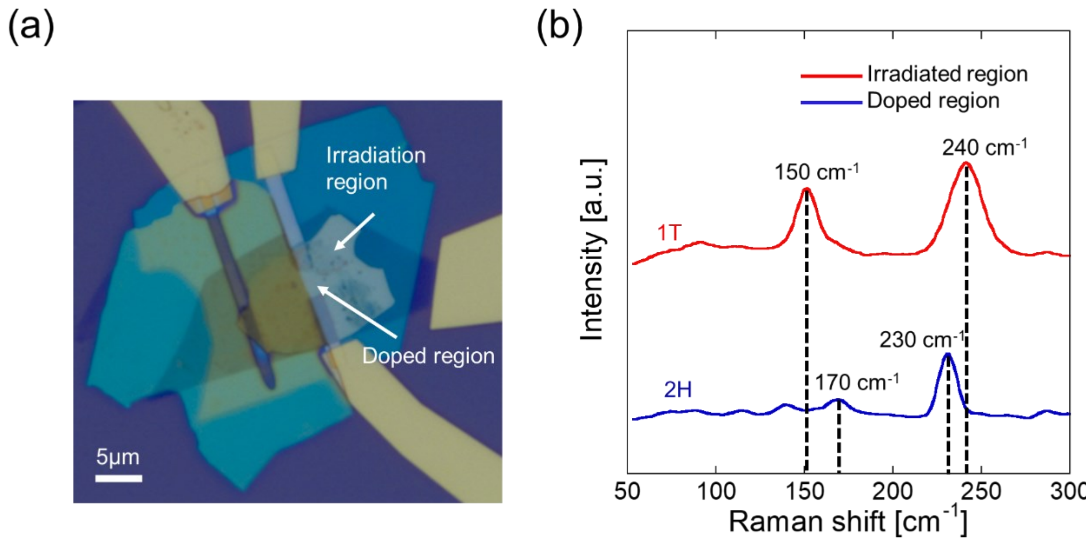

Fig. 5.29 (a) Optical image and (b) Raman spectrum of the irradiated region and doped region.

Subsequently, the heavily n-doped region served as the source, and the electrode connected to the channel served as the drain. The I_d-V_g curve was determined by sweeping the gate voltage with a reverse bias voltage of - 0.5 V at 120 K, as shown in **Fig. 5.30**. The current increased with increasing negative gate voltage, exhibiting a threshold voltage of approximately -4 V and achieving a low *SS* value of 290 mV/dec within the current range of 10^{-11} to 10^{-8}. However, after applying a positive gate voltage, the current also increased. This situation is different from the ambipolar state of the

n/i/p homojunction p-TFET but rather involves the channel transitioning to n-type under the application of positive voltage and then forming an n^+/n junction with the heavily n-doped region, while the depletion region at the n/i junction disappears. At this point, when a negative drain voltage and positive gate voltage are applied, electrons will flow from the drain metal into the channel, forming a thermal current. **Figure 5.31** depicts the I_d-V_d curves of this n/i homojunction p-TFET at different temperatures when V_g = -10 V. The negative voltage region shows the tunneling current, while the positive voltage region exhibits a diode current dominated by thermal diffusion. It can be clearly observed that the current dominated by the BTBT mechanism exhibits less dependence on temperature compared to the diode current, and in the high voltage region, it is even entirely independent of temperature. The temperature dependence of the diode current is attributed to the fact that temperature can change the energy of carriers; higher temperatures result in carriers acquiring more energy, making it easier for carriers to overcome the built-in electric field; thus, the current is increased.

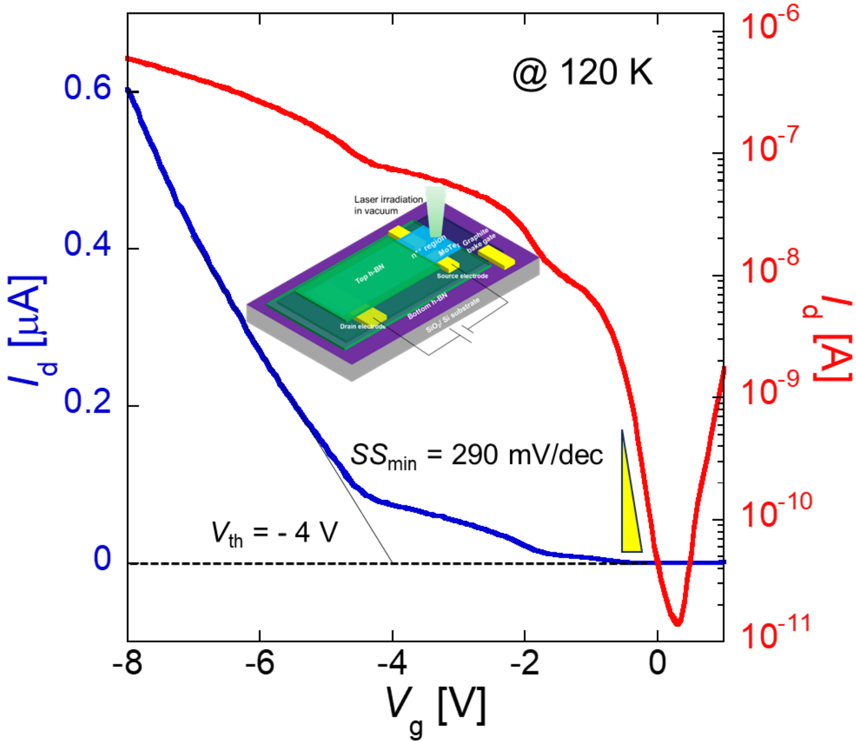

Fig. 5.30 I_d-V_g curve of the n/i homojunction p-TFET with a gate insulator of *h*-BN at V_d = -0.5 V.

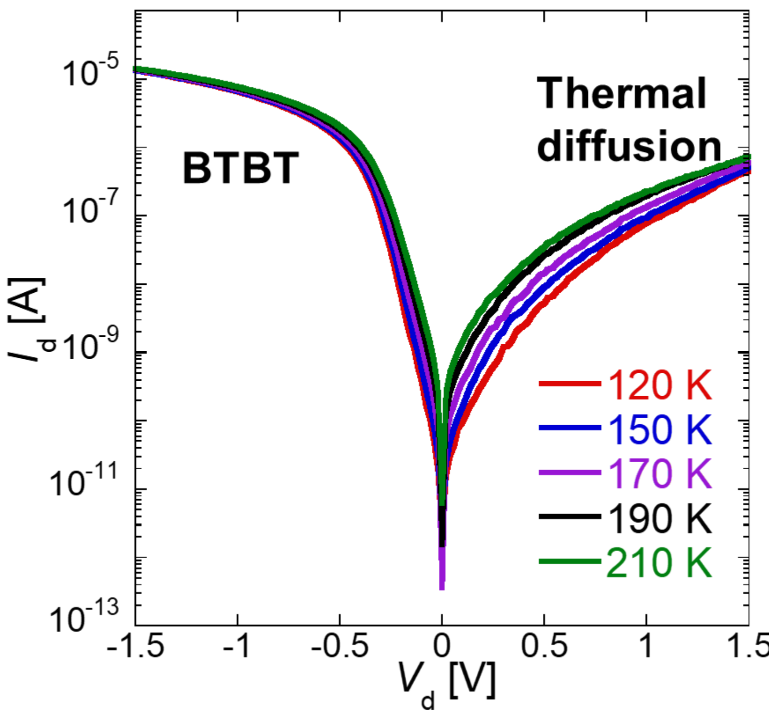

Fig. 5.31 I_d-V_d curves of the n/i homojunction p-TFET with a gate insulator of *h*-BN at different temperatures when V_g = -10 V.

5.5. CTFET inverter realization

Due to the challenges in fabricating p-TFETs, there are currently no reports on inverter fabrication based on 2D-TFETs. However, this study demonstrates that n-TFETs and p-TFETs can be fabricated using polarity-controllable laser-induced doping methods, enabling the combination of both to create a logic inverter. The fabrication process for $MoTe_2$-TFET inverters is outlined as follows:

1. A bottom h-BN/graphite stack was prepared to serve as the gate structure for one TFET, as shown in **Fig. 5.32 (a)**.
2. Source and drain electrodes were fabricated on the surface of the bottom *h*-BN, as shown in **Fig. 5.32 (b)**.
3. A top *h*-BN/$MoTe_2$ stack was placed onto the surface of the bottom *h*-BN using dry transfer technique, ensuring contact between $MoTe_2$ and the electrodes, as shown in **Fig. 5.32 (c)**.
4. A second bottom *h*-BN was placed onto graphite using dry transfer technique as the gate insulating layer for the other TFET, as shown in **Fig. 5.32 (d)**.
5. Source electrodes on the surface of the second bottom *h*-BN are fabricated, as shown in **Fig. 5.32 (e)**.
6. A second *h*-BN /$MoTe_2$ stack was placed onto the surface of the second bottom *h*-BN using dry transfer technique, with $MoTe_2$ encapsulated by the top and bottom *h*-BN. One side of $MoTe_2$ contacts the source electrode, leaving sufficient area for laser irradiation, while the other end is exposed for fabricating the drain electrode, as shown in **Fig. 5.32 (f)** and **(g)**.
7. Laser-induced doping on one side of each $MoTe_2$ in different environments is performed to create p/i and n/i homojunction, as shown in **Fig. 5.32 (h)**.

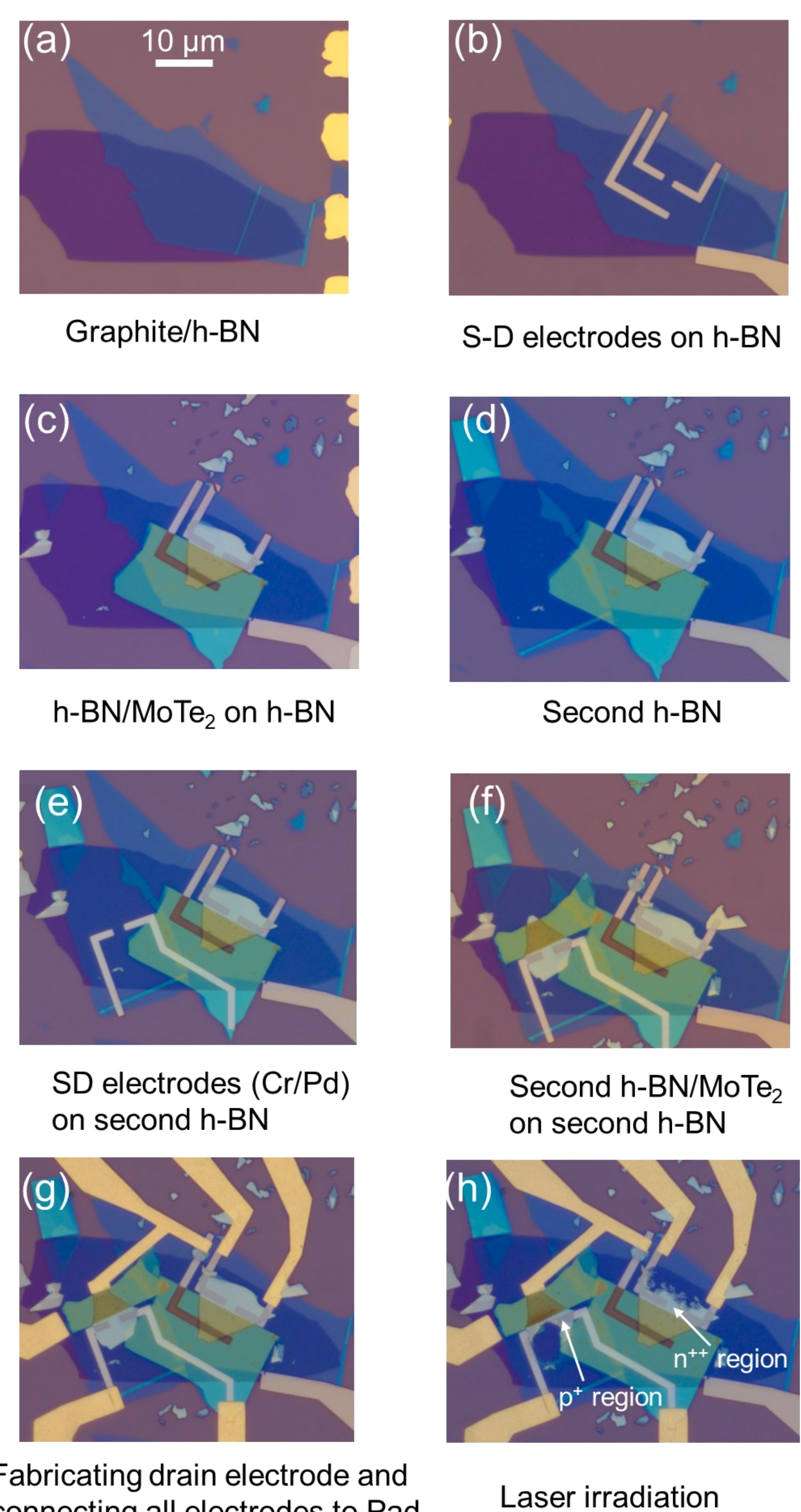

Fig. 5.32 (a) ~ (h) Fabrication process of $MoTe_2$ based CTFET inverter.

The I_d-V_g curves under a reverse bias voltage of 0.1 V were measured at room temperature for p/i and n/i homojunction structures, as shown in **Fig. 5.33**. Both can open the tunneling window and generate tunneling current even at lower reverse biases by applying gate voltage. For the p/i homojunction n-TFET, an on/off ratio exceeding 10^4 was obtained, accompanied by a lower *SS* value of 160 mV/dec, which contributed to the use of a thinner *h*-BN gate insulating layer and an excellent tunneling interface. However, for the n/i homojunction p-TFET, due to the heavy n-type doping mechanism, significant Te-vacancies served as charge traps at the tunneling interface, forming a trap-assist tunneling current, as stated before. The trap-assist tunneling current cannot be neglected at room temperature, leading to a larger off-state current and deteriorated *SS* value. This can be mitigated by lowering the temperature to suppress trap-assisted tunneling current for better performance. **Figure 5.34** illustrates the I_d-V_d curves of both TFETs at room temperature, showing that the n-TFET exhibits higher current at a low drain voltage range under the same gate voltage value. However, in the higher drain voltage region, both exhibit saturation characteristics with similar current levels, indicating that these two TFETs can be combined as an inverter.

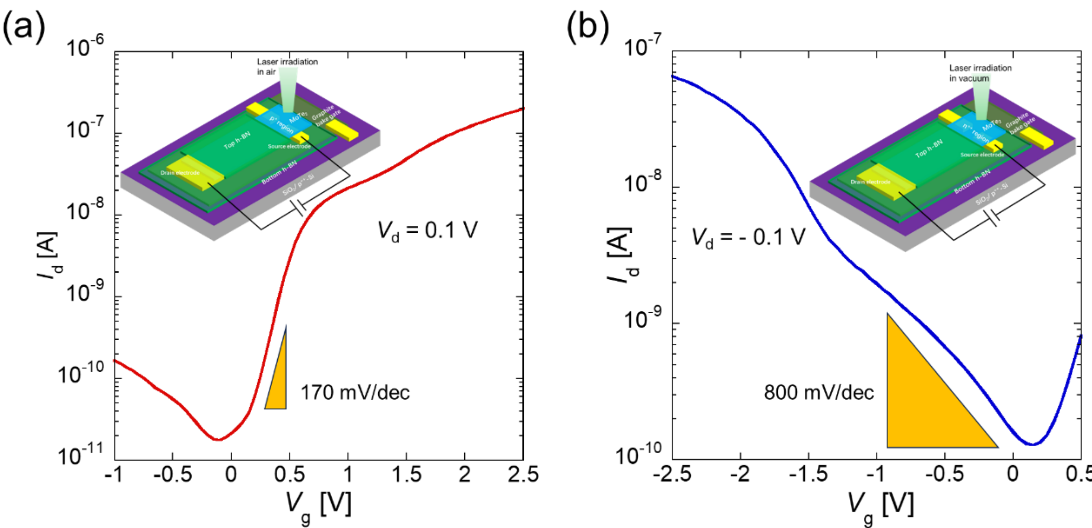

Fig. 5.33 I_d-V_g curves of the p/i homojunction n-TFET and n/i homojunction p-TFET at room temperature.

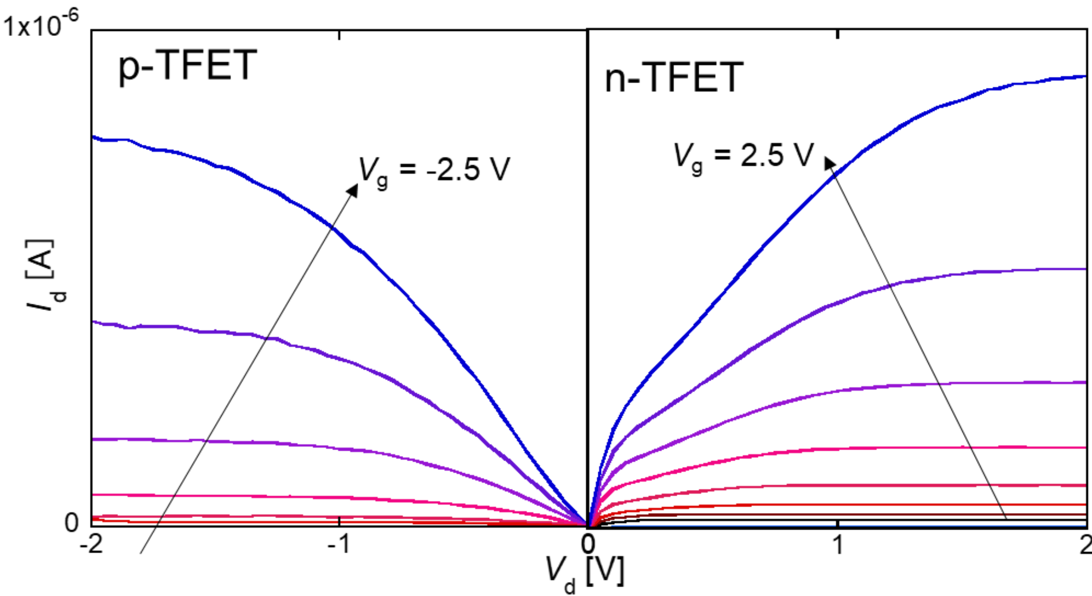

Fig. 5.34 I_d-V_d curves of the p/i homojunction n-TFET and n/i homojunction p-TFET at room temperature.

Then, the source of n-TFET was grounded, and the supply voltage (V_{dd}) was applied to the source of p-TFET. The drains of these two TFETs are connected to a common electrode. Output voltage (V_{out}) was measured by the common drain electrodes. Both n- and p-TFET are controlled by the same graphite back gate that acts as the input voltage (V_{in}) electrode. **Figure 5.35 (a)** shows the VTC of the CTFET inverter as a function of V_{dd} from 0.5 V to 1 V with a step of 0.1 V. Clean signal inversions can be observed in each VTC curve, and the transition voltages are located close to $V_{dd}/2$, especially at higher V_{dd}. **Figure 5.35 (b)** depicts the gain values (dV_{out}/dV_{in}) corresponding to each V_{dd} level. The inverter exhibits maximum gain values of 2.9, 3.4, 3.8, 4.5, 4.4 and 5 at V_{dd}, ranging from 0.5 V to 1 V, respectively.

A high-performance inverter requires various physical parameters of its internal n- and p-type transistor to match, including threshold voltage, mobility, on and off-state current values, on/off ratio, etc., and possess similar small subthreshold swings. In this experiment, although the currents at the on-state are roughly similar for both devices, the significant differences in their transfer characteristics, particularly the higher off-state current and relatively slower switching speed of the p-TFET, result in a smaller gain and poor performance of the inverter. Therefore, the focus of future work lies in

improving the performance of the p-TFET, such as by replacing the gate insulating layer with a higher dielectric constant material.

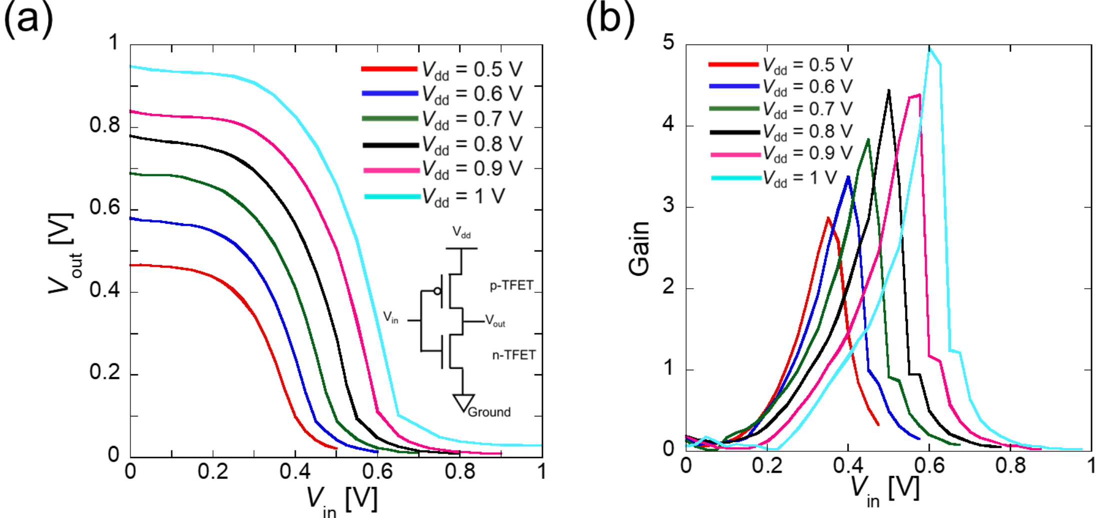

Fig. 5.35 (a) VTC curves (V_{out}-V_{in}) of CTFET inverter as a function of V_{dd}. (b) DC voltage gain of the CTFET inverter.

5.6. Conclusion

This section introduces the application of laser-induced doping effects in the fabrication of 2D-TFETs. The fabrication of 2D-TFETs requires heavily doped 2D source materials, but the lack of controllable heavy doping techniques has limited the development of 2D-TFETs. In this study, laser-induced doping is employed to selectively dope $MoTe_2$, turning it into either p^+-$MoTe_2$ or n^{++}-$MoTe_2$. Consequently, heavily doped $MoTe_2$ can be utilized as source material to fabricate n-TFETs or p-TFETs with different structures. Initially, a p/n heterojunction consisting of heavily p-doped $MoTe_2$ as the source and n-MoS_2 as the channel is constructed by using dry transfer techniques, with graphene serving as the contact electrode for MoS_2 to apply drain voltage. The I_d-V_g curve is measured by sweeping the gate voltage at a reverse bias, and the n-TFET operation demonstrates a high on/off ratio of 10^7 and a low SS_{ave} value of 300 mV/dec. Although this bi-layer TFET structure has the advantage of a large tunneling area, its fabrication requires two different materials, which is not conducive to future large-scale integration. Therefore, achieving TFET fabrication on a single 2D material is particularly significant. By dividing $MoTe_2$ into doped and undoped regions using local laser-induced doping, it becomes possible to fabricate n- and p-TFETs based on single-crystal $MoTe_2$. Initially, a p/i homojunction is fabricated through laser-induced doping in the atmosphere. The channel encapsulated by *h*-BN typically exhibits an intrinsic state, hence termed the “i” region. Upon applying a reverse bias to this p/i homojunction and sweeping the gate voltage, its operation as an n-TFET is confirmed. However, due to poor contact properties at the drain, this n-TFET exhibits a high *SS* value. To achieve a lower *SS* value, heavy n-type doping is applied to the part connected to the drain electrode of this p/i structure, forming a p/i/n homojunction structure. The n-TFET operation is confirmed by measuring the I_d-V_g curve. It shows a low SS_{min} value of 75 mV/dec at a low temperature. However, due to the presence of tunneling interfaces between the channel and drain regions, the current also increases continuously upon applying negative gate voltage, indicating an ambipolar characteristic dominated by tunneling mechanisms. In addition, p-TFET

operation is also successfully achieved based on both the n/i and the n/i/p homojunction structure, with a smaller SS_{ave} obtained when using *h*-BN as the gate insulating layer. Finally, n-TFET and p-TFET are fabricated on the same substrate and combined into an inverter. It successfully achieves signal inversion with a gain value of 5 at V_{dd} = 1 V, representing the first demonstration of 2D-CTFET inverter in the world.

Reference

[1] Y. Du, L. Yang, J. Zhang, et al. IEEE electron device letters **35**, 599 (2014).
[2] K. Sakanashi, H. Ouchi, K. Kamiya, et al. Nanotechnology **31**, 205205 (2020).
[3] L. Esaki, Physical review **109**, 603 (1958).
[4] R. N. Sajjad, W, Chern, J. L. Hoyt, et al. IEEE Transactions on Electron Devices **63**, 4380 (2016).

6. Conclusion and outlook

6.1. Conclusion

As a member of the TMDC material family, $MoTe_2$, due to its ease of being doped and polycrystalline characteristics, holds promise for applications in various electronic device fields. The effects of laser irradiation on the properties of $MoTe_2$ have been reported continuously in previous studies, including doping effects, phase transition effects, and others. Based on prior research, this study systematically explores the influence of high-density laser irradiation on the structure and electrical properties of multilayer $MoTe_2$ crystals in different crystal regions. By utilizing laser-induced phase transition and doping effects, improvements in the contact properties of $MoTe_2$-FET and the fabrication of n- and p-channel $MoTe_2$-TFETs are achieved. In addition, a $MoTe_2$-CMOS inverter with high performance and the first demonstration of a CTFET inverter are also achieved.

Chapter 1 introduces the development of Si-MOSFETs and the current issue of short-channel effects resulting from scaling. In the semiconductor roadmap, novel transistor structures and new channel materials are expected to continue Moore's Law. Among these, TFETs hold promise for application in low-power devices in the future. Therefore, this chapter describes the operating principles, structures, advantages, and current challenges of TFETs. Subsequently, several 2D materials used in this study are introduced, including graphene, *h*-BN, and TMDC. TMDC materials are promising next-generation channel materials because they exhibit a strong tolerance to the short-channel effect and high carrier mobility when utilized as channel materials thinner than 1 nm. Next, the advantages and development of 2D-FETs and 2D-TFETs are introduced. Finally, this chapter presents the structure and electrical properties of the $MoTe_2$, which is the object of this study. Then, the effects of laser irradiation on the structure and electrical properties of $MoTe_2$ of several previous studies are reviewed.

Chapter 2 introduces the experimental techniques used in sample fabrication in this study, including the exfoliation of 2D materials, fabrication of metal electrodes, 2D material transfer techniques, and laser irradiation method. In addition, various electrical

testing methods and Raman spectroscopy characterization used for material identification in this study are introduced.

Chapter 3 systematically introduces the effects of high-density laser irradiation on the crystal structure and electrical properties of $MoTe_2$. For the directly irradiated region, irradiation in the atmosphere causes the crystal to undergo thermal decomposition into Mo and Te atoms. Oxygen in the air oxidizes the Mo atoms during irradiation, forming the final product of MoO_2. Therefore, the irradiated area mainly consists of a mixed layer of MoO_2 and Te. When laser irradiation is conducted in a vacuum without the oxidation process, the high-temperature quenching process formed by laser irradiation transforms the crystal structure into the 1T phase, which can stably exist in the atmosphere. However, for the crystal near the irradiated area, the crystal temperature also increases due to the Gaussian distribution of the laser. Although the increased temperature is not enough to change the material structure, it induces the generation of a large number of Te vacancies. Under irradiation in a vacuum, these Te vacancies form a strong donor level, resulting in a heavy n-type doping effect. Under irradiation in the atmosphere, oxygen molecules rapidly adsorb to the Te vacancies during irradiation. These oxygen molecules form a strong acceptor level, resulting in a heavy p-type doping effect. This laser-induced doping effect is region-selectively and efficient, and the doped crystal is highly stable.

Chapter 4 introduces the experimental and analysis results of laser irradiation in improving the contact properties of $MoTe_2$-FET. Through laser irradiation, phase transition or heavy doping effects occur in the contact area of the FET, which avoids the Fermi level pinning effect and reduces the contact barrier, thus improving the contact properties. Additionally, contact doping can control the polarity of $MoTe_2$-FET. A $MoTe_2$ CMOS inverter is fabricated on the same substrate by the contact doping method, achieving a high gain of 31 at V_{dd} = 4 V.

Chapter 5 introduces various $MoTe_2$-TFETs fabricated using laser-induced doping technique. The heavily n- or p-type doped crystal regions through laser irradiation can be utilized as the source structure of 2D-TFETs. Forming p/i or n/i homojunction structures through directional doping based on a single $MoTe_2$ crystal, the operation of

n- and p-TFET is achieved, respectively, and they show good performance. Finally, n- and p-TFET are fabricated on the same substrate and combined into an inverter, achieving signal inversion with a gain value of 5 at V_{dd} = 1 V.

6.2. Outlook

Laser irradiation is a rapid and efficient annealing process that can be widely applied to various 2D materials. It can accelerate the device application of 2D materials. In addition to the phase transition and doping effects discussed in this study, laser irradiation also has an etching effect. Different effects can be obtained by controlling the power and irradiation method of laser irradiation, which is of great significance for applying 2D semiconductor materials in large-scale integrated circuits. Contact issues currently need to be solved for 2D materials application. Laser-induced contact doping would be a suitable method for improving contact properties. However, achieving controllable doping without damaging the irradiated crystal is an area that requires future efforts, such as using pulsed laser scanning methods. The main advantage of TFET over MOSFET is its potential to overcome the Boltzmann limit (60 mV/dec) and achieve an extremely low SS value. However, in this study, the SS values of all fabricated TFETs are larger than 60 mV/dec. There are two main reasons for the large SS value. Firstly, the laser-induced doping method employed in the experiment cannot achieve a steep doping profile. As a result, a lowly doped region exists at the tunneling interface, making carrier tunneling difficult, especially in the low-voltage region. Hence, it is imperative to investigate the laser-induced p/n interface further in the future, potentially through techniques such as scanning gate microscope (SGM) analyses. In addition, the uniformity of laser-induced doping needs to be improved, which requires adjustments to the laser irradiation methods. Secondly, the gate insulator has a low dielectric constant. SiO_2 and *h*-BN used in this experiment have a dielectric constant of only 3.9; thus, the large EOT limits the gate's control ability. A high-k 2D insulator such as $BiSe_2O_5$ is expected to solve this problem.

Acknowledgments

From October 2018, when I began my studies in Japan, to today, as I complete this doctoral thesis, the journey has been fraught with challenges. However, I have received tremendous help and support from many people and organizations. Here, I want to express my heartfelt gratitude to all those who have assisted me.

First and foremost, I would like to thank my advisor, Professor Nobuyuki Aoki. When I first entered his lab, the language barrier and my inadequate expertise left me feeling anxious. Professor Aoki patiently guided me, arranging courses for me to audit and providing substantial guidance and assistance throughout my research and academic paper writing. Moreover, he generously assisted me in applying for tuition waivers and scholarships, significantly alleviating my financial burden.

I also want to express my gratitude to Assistant Professor Mengnan Ke. During my doctoral period, he provided invaluable guidance and experimental data analysis in research, helping me achieve numerous academic accomplishments. I appreciate his companionship during our lunch outings.

I am thankful for the laboratory technician, Mr. Kida, whose expertise ensured that every student in our lab could smoothly utilize experimental instruments and apparatus. He imparted a wealth of knowledge about experimental equipment and electrical measurement.

I want to thank the laboratory secretary, Ms. Tsutsui, for her meticulous handling of all transactional work in our lab, including managing my research funding.

I am grateful to every other student in our lab, both current peers and graduates. Mr. Ikeda and Mr. Fukuda, in particular, have frequently engaged in academic discussions and shared many private conversations with me. I was also deeply impressed by a senior student, Dr. Kohei Sakanashi, who used to provide new insights in seminars and suggest many improvements for my research. He became a role model for me to keep moving forward. During my doctoral period, Jaquan Feng and Zelin Zhao joined our lab; I hope they will achieve excellent results in their future studies and research endeavors.

Furthermore, I want to express gratitude to individuals outside our lab, especially Mr. Hehe, who helped me through the most stressful period of my first year in Japan by sharing meals and conversations. This gradually helped me adjust my mindset to face challenges. I also want to thank Ms. Matsueda and Mr. Okuyama, whom I met while working part-time at AEON. Their kindness and enthusiasm made me feel warmth in a foreign land.

I am indebted to Chiba University and the Chiba University Quantum Fellowship Project for exempting my tuition fees and providing scholarship support over these years. This greatly eased my financial pressures and enabled me to focus wholeheartedly on my studies and research.

Lastly, I want to express my deepest gratitude to my parents. Without their support, I would not have been able to study in Japan, especially my mother, who tirelessly worked and sacrificed her health to support my living expenses here. Additionally, one very important person, my wife Haiyang Xu, has provided me with endless support and companionship throughout my pursuit of a doctoral degree. Her cooking is the best in the world.

Publications and conferences

Publications:

1. **Tianshun Xie**, Kazuki Fukuda, Mengnan Ke, Peter Krüger, Keiji Ueno, Gil-Ho Kim and Nobuyuki Aoki. "Enhanced contact properties of $MoTe_2$-FET via laser-induced heavy doping." Japanese Journal of Applied Physics, 62(SC), SC1010 (2022).

2. **Tianshun Xie**, Mengnan Ke, Keiji Ueno, Kenji Watanabe, Takashi Taniguchi and Nobuyuki Aoki. "Realization of $MoTe_2$ CMOS inverter by contact doping and channel encapsulation." Japanese Journal of Applied Physics, 63(2), 02SP49 (2024).

3. **Tianshun Xie**, Mengnan Ke, Keiji Ueno, Kenji Watanabe, Takashi Taniguchi and Nobuyuki Aoki. "Realization of single $MoTe_2$ crystal in-plane TFET by laser-induced doping technique", Applied Physics Letters, 124(61), 211904 (2024).

4. **Tianshun Xie**, Mengnan Ke, Peter Krüger, Keiji Ueno, and Nobuyuki Aoki. "Contact properties on semiconducting $MoTe_2$ crystal using polymorphic contact", ACS Applied Electronic Materials, Under revision.

International conference:

1. **Tianshun Xie**, Shuntaro Ikeda, Kohei Sakanashi, Keiji Ueno, Peter Krüger and Nobuyuki Aoki, "Study on the contact properties between the semi-metallic phase and the semiconducting phase of $MoTe_2$", ICN+T 2021, online, July11, 2021. (Poster)
2. **Tianshun Xie**, Kohei Sakanashi, Kazushi Yokoi, Keiji Ueno, and Nobuyuki Aoki, "Evaluation of BKT phase transition in 2H-NbS_2 flake", 29th International Conference on Low Temperature Physics, p19-SF2B-66, Sapporo, August 19, 2022. (Poster)
3. **Tianshun Xie**, Kazuki Fukuda, Mengnan Ke and Nobuyuki Aoki, "Realization of p-type TFET via laser-induced doping technique", 2022 International Conference on Solid State Devices and Materials, F-9-02, Chiba, September 29, 2022. (Oral)
4. **Tianshun Xie**, Mengnan Ke, Peter Krüger, Keiji Ueno, Gil-Ho Kim, Nobuyuki Aoki, "Application of laser irradiation for multilayer $MoTe_2$: phase transition, contact engineering and TFET fabrication", The Fullerenes, Nanotubes and Graphene Research Society, 2P-32, Nagoya, March 2, 2023. (Poster)
5. **Tianshun Xie**, Mengnan Ke and Nobuyuki Aoki, "High-performance CMOS inverter based on $MoTe_2$-FETs achieved by contact doping and channel encapsulation", 2023 International Conference on Solid State Devices and Materials, A-2-05, Nagoya, September 6, 2023. (Oral)

Japanese domestic conference:

1. 謝 天順, 大内 秀益, 坂梨 昂平, 上野 啓司, 青木 伸之.「1T'-$MoTe_2$と 2H-$MoTe_2$のコンタクトの特性の評価」, 応用物理学会 2020 年春季学習講演会, 上智大学四谷キャンパス, コルナのため中止
2. 謝 天順, 大内 秀益, 坂梨 昂平, 上野 啓司, 青木 伸之.「低バリアの実現に向けた 1T'-$MoTe_2$と 2H-$MoTe_2$のコンタクト特性の評価」, 応用物理学会 2020 年秋季学習講演会, 11a-Z29-13, 2020 年 9 月 11 日. (オンライン口頭発表、査読あり)
3. 謝 天順, 池田 駿太郎, 坂梨 昂平, 上野 啓司, 青木 伸之.「真空中でレーザー照射により得られた 1T-$MoTe_2$ と 2H-$MoTe_2$ のコンタクト特性の評価」, 応用物理学会 2021 年春季学習講演会, 18p-Z31-4, 2021 年 3 月 18 日 (オンライン口頭発表、査読あり)
4. 謝 天順, 坂梨 昂平, 上野 啓司, 青木 伸之.「剥離により得られた 2H-NbS_2薄膜における BKT 相転移の評価」, 応用物理学会 2022 年春季学習講演会, 22p-p06-15, 2022 年 3 月 22 日. (現地ポスター発表、査読あり)
5. 謝 天順, 福田 和紀, 柯 梦南, 青木 伸之.「レーザー誘起ドーピング技術を用いて p 型 $MoTe_2$-TFET の実現」,応用物理学会 2022 年秋季学習講演会, 22a-B202-2, 東北大学, 2022 年 9 月 20 日. (現地口頭発表、査読あり)
6. 謝 天順, 柯 梦南, 上野 啓司, 青木伸之. 「レーザー誘起ドーピング技術を用いた高性能 TFET の作製」, 応用物理学会 2023 年春季学習講演会, 17a-B414-5, 上智大学四谷キャンパス, 2023 年 3 月 17 日. (現地口頭発表、査読あり)
7. 謝 天順, 柯 梦南, 上野 啓司, 青木伸之. 「$MoTe_2$における CTFET インバーターの作製」, 応用物理学会 2023 年秋季学習講演会, 19p-P01-73, 熊本城ホール, 2023 年 9 月 19 日. (現地ポスター発表、査読あり)